PART I: FOLD CONTINUATION AND THE FLOW BETWEEN ROTATING, COAXIAL DISKS

PART II: EQUILIBRIUM CHAOS

PART III: A MESH SELECTION ALGORITHM FOR TWO-POINT BOUNDARY VALUE PROBLEMS

Thesis by
Jeffrey Michael Fier

In Partial Fulfillment of the Requirements

for the Degree of

Doctor of Philosophy

California Institute of Technology

Pasadena, California

1985

(Submitted December 10, 1984)

Acknowledgments

First of all, I would like to thank my advisor, Prof. H. B. Keller, for suggesting the topics of this thesis and for his great patience in guiding my work on them. I would also like to thank my undergraduate advisor, Prof. D. S. Cohen, for his advice and friendship during my many years at Caltech.

Support for this work has come from numerous sources including a fellowship from the Northrop Corporation and teaching assistantships and fellowships from the Institute. Summer and graduate resarch assistantships have been provided by the NSF under grant MCS-78-03036, the Air Force under contract AFOSR-82-8321, and the DOE under contract DE-AM03-76SF00767.

The computations were carried out at Caltech on an IBM 4341 with time donated by IBM and on the Fluid Mechanics VAX 11/750 in the Applied Mathematics department. The manuscript was typeset using the HP TEX system on equipment donated to Caltech by Hewlett-Packard. The plots were generated by the NCAR SCD graphics system and I would like to thank Bill Henshaw, Mike Henderson and James Kamm for getting it to run on the 4341 and suffering with me while we tried to get it to work.

Finally, and most of all, I would like to thank my parents, who have made contributions above and beyond anything which could be reasonably asked of them. This is for them.

Abstract

Part I:

We consider folds in the solution surface of nonlinear equations with two free parameters. A system of equations whose solutions are fold paths is formulated and proved to be non-singular in a neighborhood of a fold, thus making continuation possible. Efficient numerical algorithms employing block Gaussian elimination are developed for applying Euler-Newton pseudo-arclength continuation to the system, and these are shown to require fewer operations than other methods.

To demonstrate the use of these methods we calculate the flow between two infinite, rotating disks. For Reynold's number less than 1000, six separate solution sheets are found and completely described. Plots of 47 solutions for three values of the disk speed ratio and for Reynold's number equal to 625 are shown. These are compared with the solutions found by previous investigators.

Part II:

Two ordinary differential equations with parameters whose solution paths exhibit an infinite sequence of folds clustered about a limiting value are studied. Using phase-plane analysis, expressions for the limiting ratios of the parameter values at which these folds occur are derived and the limiting values are shown to be non-universal.

Part III:

A mesh selection algorithm for use in a code to solve first-order nonlinear two-point boundary value problems with separated end conditions is described. The method is based on equidistributing the global error of the box scheme, a

numerical estimate of which is obtained from Richardson extrapolation. Details of the algorithm and examples of its performance on non-stiff and stiff problems are presented.

Table of Contents

List of Figures

Part I: Fold Continuation and the Flow Between Rotating Coaxial Disks

CHAPTER 1

Theory and Numerical Methods for Fold Continuation

1.1 Introduction

We consider nonlinear systems of the form

$$G(u, \lambda, \tau) = 0 \tag{1.1.1}$$

where $G: \mathbb{B} \times \mathbb{R} \times \mathbb{R} \to \mathbb{B}$ is a C^2-mapping and $\mathbb{B}$ is a Banach space. Here, λ and τ are free parameters and the solution $u(\lambda, \tau)$ of (1.1.1) represents a two-dimensional surface in $\mathbb{B} \times \mathbb{R}^2$. Equations of this form occur frequently when describing the steady states of physical systems. One example, which we shall consider later, is the flow between two infinite, rotating, coaxial disks. In this problem λ represents the Reynold's number and τ the ratio of disk speeds. Other examples occur in various fields such as elasticity and chemical reactor theory [23,8].

In solving equations of the above form, one seeks a complete description of the solution surface for all values of the parameters in some region of interest in the (λ, τ)-plane. In particular, one would like to know how many solutions equation (1.1.1) has in different regions of the plane and how these solutions could be obtained from one another by continuation in λ or τ. In addition, one would like to know where critical behavior such as change of stability occurs. For many problems this essentially reduces to locating the folds in the solution surface, since folds generally indicate both transitions in the number of solutions and changes in important characteristics of the solutions. Moreover, folds often represent the

only major global structures in the solution surface, since other phenomena such as bifurcations are usually not stable to perturbations in the problem parameters and consequently remain isolated singular points. Thus, one can usually obtain a complete picture of the solution surface just from the folds. But even for problems in which other structures do exist, the description of the solution would not be complete without determining the locations of the folds. In this work we describe a numerical procedure for efficiently calculating folds.

In order to define a fold more precisely, we now review some basic results from bifurcation theory (see Keller [17]). Holding r fixed in (1.1.1), we obtain the one-parameter family

$$G(u, \lambda) = 0. \tag{1.1.2}$$

If $[u_0, \lambda_0]$ is a solution of (1.1.2) and the Fréchet derivative $G_u(u_0, \lambda_0) \equiv G_u^0$ is non-singular, then $[u_0, \lambda_0]$ is called a *regular solution (point)* and the Implicit Function Theorem guarantees a unique solution branch $[u(\lambda), \lambda]$ of (1.1.2) in a neighborhood of $[u_0, \lambda_0]$. When G_u^0 is singular, the Implicit Function Theorem fails and it is advantageous to introduce a new parameter, s, the arclength. Differentiating (1.1.2) with respect to s, including the arclength condition and evaluating at $[u_0, \lambda_0]$, we obtain the system

$$G_u^0 \dot{u}_0 + G_\lambda^0 \dot{\lambda}_0 = 0 \tag{1.1.3a}$$

$$\|\dot{u}_0\|^2 + |\dot{\lambda}_0|^2 = 1 \tag{1.1.3b}$$

where $G_\lambda^0 \equiv G_\lambda(u_0, \lambda_0)$ and $\dot{} \equiv d/ds$.

In studying (1.1.3) there are two cases to consider. When $G_\lambda^0 \in \mathcal{R}(G_u^0)$, bifurcation may occur and it is likely that two distinct solution paths pass through $[u_0, \lambda_0]$. We shall not be concerned with this case here. What we are interested in is the case when $G_\lambda^0 \notin \mathcal{R}(G_u^0)$. In this case we call the solution point $[u_0, \lambda_0]$

a *fold* because the solution path usually folds over so that there are two solutions for λ on one side of the singular point and no solutions for λ on the other side. Unfortunately, this terminology is not standard. Some authors have instead used the term "limit point" [17,14], while others have of late preferred to call these "turning points" [36,12]. But since our main interest is in problems with more than one free parameter, for which singularities of this form can truly be described as folds, it seems natural to retain this terminology even when we are only considering single parameter problems.

For our work here we consider singularities of the form

$$\mathcal{N}(G_u^0) = \text{span}\{\phi_0\}, \qquad \|\phi_0\| = 1 \tag{1.1.4a}$$

$$\mathcal{N}(G_u^{0*}) = \text{span}\{\psi_0^*\}, \qquad \|\psi_0^*\| = 1 \tag{1.1.4b}$$

$$\mathcal{R}(G_u^0) = \{\, x \in \mathbb{B} \mid \psi_0^* x = 0 \,\} \tag{1.1.4c}$$

where $G_u^{0*}: \mathbb{B}^* \to \mathbb{B}^*$ is the adjoint of the operator G_u^0. This is the most common form a singularity of G_u^0 assumes and so this assumption does not impose much of a restriction on our work. We call a fold with this type of singularity a *simple fold*.

To describe the solution path in a neighborhood of a simple fold, we need to look at the second derivatve of (1.1.2):

$$G_u^0 \ddot{u}_0 + G_\lambda^0 \ddot{\lambda}_0 = -\big(G_{uu}^0 \dot{u}_0 \dot{u}_0 + 2G_{u\lambda}^0 \dot{u}_0 \dot{\lambda}_0 + G_{\lambda\lambda}^0 \dot{\lambda}_0^2\big). \tag{1.1.5}$$

Since $G_\lambda^0 \notin \mathcal{R}(G_u^0)$, it follows that $\psi_0^* G_\lambda^0 \neq 0$, which combined with (1.1.3) gives

$$\dot{\lambda}_0 = 0, \qquad \dot{u}_0 = \phi_0. \tag{1.1.6}$$

Using this in (1.1.5) we have

$$G_u^0 \ddot{u}_0 + G_\lambda^0 \ddot{\lambda}_0 = -G_{uu}^0 \phi_0 \phi_0,$$

and upon applying ψ_0^* to both sides we obtain

$$\ddot{\lambda}_0 = -\frac{\psi_0^* G_{uu}^0 \phi_0 \phi_0}{\psi_0^* G_\lambda^0}.$$

If $\psi_0^* G_{uu}^0 \phi_0 \phi_0 \neq 0$, then $\ddot{\lambda} \neq 0$ and we call $[u_0, \lambda_0]$ a *quadratic simple fold.* If $\ddot{\lambda}_0 = 0$, then higher derivatives must be considered and the solution path can be cubic, quartic, etc. In general, if $d^k\lambda/ds^k = 0$ for $k = 1, 2, \ldots, \mathrm{N}-1$, and $d^{\mathrm{N}}\lambda/ds^{\mathrm{N}} \neq 0$, we term the singularity a *simple fold of order* N. Higher order folds, however, are generally unstable to perturbations and thus will not lead to the types of global structures in the solution surface of $G(u, \lambda, \tau) = 0$ which we seek. Therefore, in this work we will only consider quadratic simple folds and, for ease of reference, we will normally drop the term quadratic. In addition, since we are only considering simple folds, we will also drop the term simple. Thus, in the remainder of this work, *the term fold will be understood to mean a simple quadratic fold.*

In the next section we return to problems with two free parameters and introduce an extended system whose solutions are the folds of (1.1.1). We then show that continuation methods may be applied to this extended system in order to easily trace out the folds in the solution surface. In the following section we describe the numerical methods for implementing Euler-Newton continuation along a fold, including methods to efficiently solve matrix systems involving the Jacobian of the extended system.

At this time we would like to point out that since this work began, Rheinboldt [39] and Jepson and Spence [12] have published papers dealing with continuation along folds. Their work has been based on a slightly different extended system than that used here, one which was introduced by Keener and Keller [14] for studying perturbed bifurcations. In the final section of Chapter 1, we will compare our method with their methods. In Chapter 2 we will apply fold continu-

ation to the problem of calculating the flow between two infinite, rotating, coaxial disks.

1.2 The Extended System

We return to problems of the form (1.1.1) and consider the equations necessary to describe folds in its solution surface. As we saw in Section 1.1, if we hold τ fixed and look at the solution branches as a function of λ, a fold is a singular point where $G_\lambda \notin \mathcal{R}(G_u)$. With τ fixed, we call this a *fold with respect to* λ. In most cases, a fold with respect to λ is also a fold with respect to τ and vice versa. But it is possible that at a fold with respect to, say, τ, the tangent vector to the solution surface could lie entirely in a plane perpendicular to the τ-axis. In this case, we would expect that, instead of a fold, this singular point would be an isolated solution or bifurcation point with respect to λ, and we would no longer have that $G_\lambda \notin \mathcal{R}(G_u)$. Thus, by restricting ourselves to a formulation in terms λ, we can run into difficulties even though the singular point is legitimately a fold (with respect to τ).

In order to insure that these difficulties do not arise, we define λ' and τ' to be a linear transformation of the (λ, τ)-plane such that the tangent vector at a given fold with respect to λ' does not lie completely in a plane perpendicular to the τ'-axis (see fig. 1.1). This will remain true in a neighborhood of the given fold. Thus, a formulation in terms of λ' will remain valid in that neighborhood and so can be used as the basis for a continuation procedure. In the analysis that follows we shall assume a formulation in terms of the transformed parameters λ' and τ'. Thus, when we say fold, we mean a fold with respect to λ'. But in order to keep the notation as simple as possible, we shall drop the primes from here on out.

If $[u_0, \lambda_0, \tau_0]$ is a fold, then we may immediately write down that $[u_0, \lambda_0, \tau_0]$

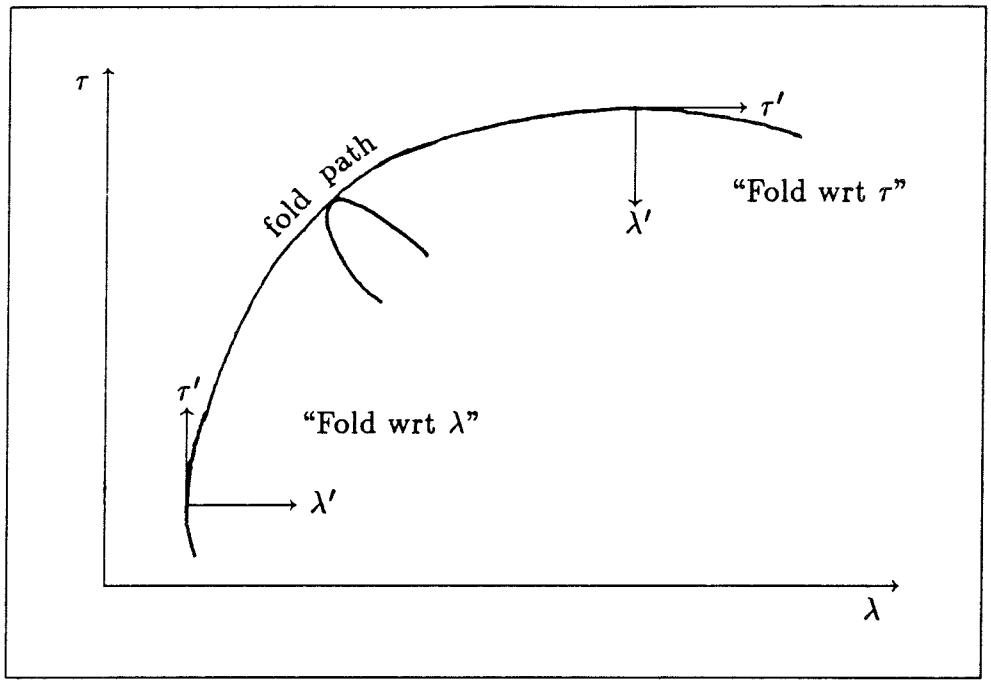

Figure 1.1. The (λ', τ')-coordinate system is rotated so that at any given point on the fold path, the tangent vector to the path is parallel, or nearly parallel, to the τ'-axis.

satisfies the set of equations

$$G(u_0, \lambda_0, \tau_0) = 0 \tag{1.2.1a}$$

$$G_u^0 \phi_0 = 0 \tag{1.2.1b}$$

$$G_u^{0*} \psi_0^* = 0 \tag{1.2.1c}$$

$$\psi_0^* G_\lambda^0 = 1. \tag{1.2.1d}$$

Here, (1.2.1a) indicates that $[u_0, \lambda_0, \tau_0]$ is a solution of our system, (1.2.1b) and (1.2.1c) show that it is also a singular point, and (1.2.1d) tells us that this singular point is a fold instead of a bifurcation point, and also normalizes ψ_0^*.

In order to arrive at a system which is not overdetermined, we need to remove the redundancy generated by the presence of both (1.2.1b) and (1.2.1c). Since ψ_0^* is also present in (1.2.1d), and ϕ_0 only occurs in (1.2.1b), the most natural way to do this is to remove (1.2.1b) from (1.2.1). Doing so gives us our extended

system:

$$G(u_0, \lambda_0, \tau_0) = 0 \tag{1.2.2a}$$

$$G_u^{0*}\psi_0^* = 0 \tag{1.2.2b}$$

$$\psi_0^* G_\lambda^0 = 1. \tag{1.2.2c}$$

As an alternative, we could have formed an extended system by discarding (1.2.1c) instead of (1.2.1b). But then we would have needed to replace (1.2.2c) with another condition to normalize ϕ_0. This was done by Moore and Spence [36] who obtained

$$G(u, \lambda) = 0 \tag{1.2.3a}$$

$$G_u(u, \lambda)\phi = 0 \tag{1.2.3b}$$

$$l(\phi) - 1 = 0, \tag{1.2.3c}$$

where l is a bounded linear functional on $\mathbb{B}$. This was the system used by Rheinboldt [39] and Jepson and Spence [12].

We now wish to show that (1.2.2) is suitable for continuation. To do this we will show that the Fréchet derivative of (1.2.2) is nonsingular at a simple fold. Then we will append an arclength condition to (1.2.2) which will permit continuation independent of λ or τ along the fold path. Finally, we will justify the continuation with the Implicit Function Theorem.

Lemma 1.2.4 *Given that (1.1.4) holds, the Fréchet derivative of (1.2.2) is nonsingular if* $[u_0, \lambda_0, \tau_0]$ *is a simple fold.*

Proof. We need to show that for all $(r, s^*, t) \in \mathbb{B} \times \mathbb{B}^* \times \mathbb{R}$ there exists a unique $(\xi, \eta^*, \varsigma) \in \mathbb{B} \times \mathbb{B}^* \times \mathbb{R}$ such that

$$G_u^0 \xi + G_\lambda^0 \varsigma = r \tag{1.2.5a}$$

$$(G_{uu}^0 \xi)^* \psi_0^* + G_u^{0*}\eta^* + G_{u\lambda}^{0*}\psi_0^*\varsigma = s^* \tag{1.2.5b}$$

$$\psi_0^*(G_{\lambda u}^0 \xi) + \eta^* G_\lambda^0 + (\psi_0^* G_{\lambda\lambda}^0)\varsigma = t. \tag{1.2.5c}$$

Operating on (1.2.5a) with ψ_0^* we obtain

$$\psi_0^*(G_u^0\xi) + (\psi_0^* G_\lambda^0)\varsigma = \psi_0^* r.$$

Using (1.2.2b) and (1.2.2c) we find

$$\varsigma = \psi_0^* r. \tag{1.2.6}$$

With this value of ς, $r - G_\lambda^0\varsigma \in \mathcal{R}(G_u^0)$, so there exists a unique $\tilde{\xi}_0$ such that

$$G_u^0\tilde{\xi}_0 = r - G_\lambda^0\varsigma, \qquad \psi_0^*\tilde{\xi}_0 = 0.$$

Therefore, ξ takes the form

$$\xi = \tilde{\xi}_0 + \alpha\phi_0 \tag{1.2.7}$$

Now if we let (1.2.5b) operate on ϕ_0, we obtain

$$(G_{uu}^0\xi)^*\psi_0^*\phi_0 + G_u^{0*}\eta^*\phi_0 + G_{u\lambda}^{0*}\psi_0^*\phi_0\varsigma = s^*\phi_0$$

which, after using (1.2.1b) and the definition of an adjoint, becomes

$$\psi_0^* G_{uu}^0\xi\phi_0 + \psi_0^* G_{u\lambda}^0\phi_0\varsigma = s^*\phi_0. \tag{1.2.8}$$

Substituting (1.2.7) into (1.2.8), and recalling that $[u_0, \lambda_0, \tau_0]$ is a simple fold if and only if $\psi_0^* G_{uu}^0\phi_0\phi_0 \neq 0$, we find

$$\alpha = \frac{s^*\phi_0 - \psi_0^* G_{u\lambda}^0\phi_0\varsigma - \psi_0^* G_{uu}^0\tilde{\xi}_0\phi_0}{\psi_0^* G_{uu}^0\phi_0\phi_0}. \tag{1.2.9}$$

With α known we may now solve (1.2.5b) for η^*. We obtain

$$\eta^* = \tilde{\eta}_0^* + \beta\psi_0^*$$

where $\tilde{\eta}_0^*$ is the unique solution to

$$G_u^{0*}\tilde{\eta}_0^* = s^* - G_{u\lambda}^{0*}\psi_0^*\varsigma - (G_{uu}^0\xi)^*\psi_0^*, \qquad \phi_0^{**}\tilde{\eta}_0^* = 0, \tag{1.2.10}$$

and where $\phi_0^{**} \in \mathbb{B}^{**}$ is chosen such that

$$\phi_0^{**} G_u^{0\,*}(\cdot) = 0, \qquad \|\phi_0^{**}\| = 1.$$

Substituting this form for η^* into (1.2.5c) and using (1.2.2c), we find that

$$\beta = t - \varsigma \psi_0^* G_{\lambda\lambda}^0 - \psi_0^* G_{\lambda u}^0 \xi - \tilde{\eta}_0^* G_\lambda^0. \tag{1.2.11}$$

This shows that the Fréchet derivative of (1.2.2) is onto. To show that it is also one-to-one merely requires noting that $(r, s^*, t) = (0,0,0)$ implies that $(\xi, \eta^*, \varsigma) \equiv (0,0,0)$.

Having shown the Fréchet derivative is one-to-one and onto, the result then follows from the open mapping theorem. ■

Since the Fréchet derivative of (1.2.2) is nonsingular, we are free to solve this system using, say, Newton's method. To do this we would need to fix τ at τ_0, choose some initial values $u^{(0)}$, $\psi^{*(0)}$ and $\lambda^{(0)}$ for the unknowns u_0, ψ_0^* and λ_0, and iterate. But since our goal is to use continuation on this system, it is convenient to introduce a parameter other than τ to continue in, since, just as in the case of continuation in single parameter problems, the solution path may bend around at some value of τ.

A natural choice for this parameter is the arclength, or more conveniently pseudo-arclength, along the fold path, which would require appending to (1.2.2) the additional constraint

$$\begin{aligned} \dot{u}^*(s_0)\big[u(s) - u(s_0)\big] + \dot{\psi}^{**}(s_0)\big[\psi^*(s) - \psi^*(s_0)\big] + \dot{\lambda}(s_0)\big[\lambda(s) - \lambda(s_0)\big] \\ + \dot{\tau}(s_0)\big[\tau(s) - \tau(s_0)\big] - (s - s_0) = 0. \end{aligned} \tag{1.2.12}$$

Here, the Hahn-Banach theorem has been used to choose $\dot{u}^*(s_0) \in \mathbb{B}^*$ so that $\dot{u}^*(s_0)\dot{u}(s_0) = \|\dot{u}(s_0)\|^2$ and $\dot{\psi}^{**}(s_0) \in \mathbb{B}^{**}$ so that $\dot{\psi}^{**}(s_0)\dot{\psi}^*(s_0) = \|\dot{\psi}^*(s_0)\|^2$.

With this constraint s represents the pseudo-arclength in the space $\mathbb{B}\times\mathbb{B}^*\times\mathbb{R}\times\mathbb{R}$. However, we can also let s represent the pseudo-arclength in the space $\mathbb{B}\times\mathbb{R}\times\mathbb{R}$ by dropping the ψ^* dependence from the above equation. This is desirable for two reasons. First, this is the space we think of when we picture the solution surface of (1.1.1); s represents a tangible quantity: the pseudo-arclength along a fold in a sheet of solutions. Second, by choosing this form for the constraint, we will be able to numerically solve systems involving the Jacobian of this constraint and the extended system in a much more efficient way than if the form (1.2.12) were used.

So, for our extended system we now consider the set of equations

$$G(u,\lambda,\tau)=0 \tag{1.2.13a}$$

$$G_u^*\psi^*=0 \tag{1.2.13b}$$

$$\psi^*G_\lambda-1=0 \tag{1.2.13c}$$

$$\begin{aligned}\dot{u}^*(s_0)\big[u(s)-u(s_0)\big]+\dot{\lambda}(s_0)\big[\lambda(s)-\lambda(s_0)\big]\\ +\dot{\tau}(s_0)\big[\tau(s)-\tau(s_0)\big]-(s-s_0)=0.\end{aligned} \tag{1.2.13d}$$

To make referring to this system a little easier, let $X\equiv(u,\psi^*,\lambda,\tau)\in\mathbb{B}\times\mathbb{B}^*\times\mathbb{R}\times\mathbb{R}$ and let $F(X)=0$ denote (1.2.13). We now show that the Fréchet derivative F_X^0 is nonsingular in the following lemma.

Lemma 1.2.14 *Given that (1.1.4) holds, F_X evaluated at $X_0\equiv(u_0,\psi_0^*,\lambda_0,\tau_0)$ is nonsingular if $[u_0,\lambda_0,\tau_0]$ is a simple fold and $\dot{\tau}(s_0)\neq 0$.*

Proof. The Fréchet derivative is given by

$$F_X = \left(\begin{array}{ccc|c} G_u & O & G_\lambda & G_\tau \\ (G_{uu}\cdot)^*\psi^* & G_u^* & G_{u\lambda}^*\psi^* & G_{u\tau}^*\psi^* \\ \psi^*(G_{\lambda u}\cdot) & \cdot G_\lambda & \psi^*G_{\lambda\lambda} & \psi^*G_{\lambda\tau} \\ \hline \dot{u}^*(s_0) & 0 & \dot{\lambda}(s_0) & \dot{\tau}(s_0) \end{array}\right) \equiv \left(\begin{array}{c|c} A & b \\ \hline c^* & d \end{array}\right).$$

In Lemma 1.2.4 we showed that the operator A is nonsingular when evaluated at $s = s_0$. To proceed here we use Keller's Lemma 2.8 [17] which states that $F_X(s_0)$ is nonsingular if and only if $d - c^* A^{-1} b \neq 0$ at s_0. Differentiating (1.2.13a–c) with respect to s and using the above notation, we have

$$A \begin{pmatrix} \dot{u}(s) \\ \dot{\psi}^*(s) \\ \dot{\lambda}(s) \end{pmatrix} = -\dot{\tau}(s) b.$$

$A(s_0)$ is nonsingular, so using the Implicit Function Theorem we may solve this in a neighborhood of s_0 since we have assumed $\dot{\tau}(s_0) \neq 0$. We obtain

$$A^{-1} b = -\frac{1}{\dot{\tau}(s)} \begin{pmatrix} \dot{u}(s) \\ \dot{\psi}^*(s) \\ \dot{\lambda}(s) \end{pmatrix}.$$

Therefore, we have that

$$\begin{aligned} d - c^* A^{-1} b &= \dot{\tau}(s_0) + \begin{pmatrix} \dot{u}^*(s_0) & 0 & \dot{\lambda}(s_0) \end{pmatrix} \frac{1}{\dot{\tau}(s)} \begin{pmatrix} \dot{u}(s) \\ \dot{\psi}^*(s) \\ \dot{\lambda}(s) \end{pmatrix} \\ &= \frac{1}{\dot{\tau}(s)} \{ \dot{\tau}(s_0)\dot{\tau}(s) + \dot{u}^*(s_0)\dot{u}(s) + \dot{\lambda}(s_0)\dot{\lambda}(s_0) \}. \quad (1.2.15) \end{aligned}$$

Letting $s \to s_0$ in (1.2.13d) we obtain

$$\dot{u}^*(s_0)\dot{u}(s_0) + \dot{\lambda}^2(s_0) + \dot{\tau}^2(s_0) = 1.$$

Thus, for s sufficiently close to s_0 the expression in braces in (1.2.15) cannot be zero, which implies that $d - c^* A^{-1} b \neq 0$ at $s = s_0$. ■

The assumption $\dot{\tau}(s_0) \neq 0$ in Lemma 1.2.14 was necessary due to the fact that a fold path may achieve an extremum in τ as we continue in s; that is,

the tangent vector to the solution path lies entirely in a plane normal to the τ-axis. As mentioned above, when this happens, we no longer have a fold in the restricted problem $G(u, \lambda) = 0$ since locally the solution branch degenerates to an isolated point (an *isola*), a transverse bifurcation (*hyperbolic point*) or to a pitchfork bifurcation (a *cusp*). We dealt with this above by choosing λ and τ to be a transformation of the original problem parameters such that $\dot{\tau}(s_0) \neq 0$. This solves the problem locally, but in employing continuation we are bound to run into subsequent problems if we do not modify this transformation during the course of the continuation. We now discuss what is done in practice.

In the case of an isola or hyperbolic point, the fold path merely bends around, so that we have $\dot{\tau}(s_0) = 0$ and $\dot{\lambda}(s_0) \neq 0$. Thus, this point is a fold with respect to τ, and we may deal with the situation simply by rotating our coordinate system 90°. Thus, to get around this extremum, all we have to do is interchange the roles of λ and τ in (1.2.2).

There is, however, an even better way to deal with this situation. We choose λ and τ to be a transformation of the original problem parameters such that λ is the coordinate perpendicular to the fold path, and τ is the coordinate tangent to fold path at s_0. With the transformation so chosen, we have that $\dot{\lambda}(s_0) = 0$ and $\dot{\tau}(s_0) \neq 0$. Now, as we step along in the continuation procedure, we keep changing the transformation so that λ is always perpendicular to the fold path. In this way we will always be able to keep the hypothesis of Lemma 1.2.14 satisfied.

The only problem with using this approach in an actual continuation procedure is that, in addition to the unknowns u, ψ^*, λ and τ, we must also solve for the angle between our current parameter coordinate system and the coordinate system of the original problem parameters, which unduly complicates matters. So, instead of using a purist's approach, we settle for choosing the angle between the coordinate systems at each step to be that angle which makes the transformed

coordinate λ orthogonal to the solution path at the point we are continuing from. Now, when we converge to the next solution, λ probably will not be normal to the fold path. But as long as the fold path has curved by less than 90° during the step, we will not have violated the condition in Lemma 1.2.14. And requiring that continuation steps be small enough so that the solution path bends around less than 90° is not even a restriction since in using pseudo-arclength continuation, we always require the dot product of consecutive tangent vectors to be positive to ensure that the continuation is proceeding in the proper direction, and this is exactly the less than 90° condition (see Keller [18]).

At a cusp the situation is a bit trickier since this is a simple fold of order three with respect to the coordinate normal to the solution path (and a pitchfork bifurcation with respect to the coordinate tangent to the solution path). Here, both $\dot{r}(s_0)$ and $\dot{\lambda}(s_0)$ equal 0. So rotating the coordinate system is not going to alleviate the problem. But in practice we have found we can simply step over cusps (the same as one can step over bifurcation points using pseudo-arclength continuation in single parameter problems), and so they have produced no real problems.

We conclude this section by using Lemma 1.2.14 and the Implicit Function Theorem to obtain the following theorem, which demonstrates the existence of a fold path in the neighborhood of a solution to (1.2.13):

Theorem 1.2.16 *Given that (1.1.4) holds and that* $[u_0, \lambda_0, \tau_0]$ *is a simple fold of (1.1.2), then there exists a* $\rho_0 > 0$ *and smooth functions* $u(s) \in \mathbb{B}$, $\psi^*(s) \in \mathbb{B}^*$, $\lambda(s) \in \mathbb{R}$ *and* $\tau(s) \in R$ *such that* $u(s_0) = u_0$, $\psi^*(s_0) = \psi_0^*$, $\lambda(s_0) = \lambda_0$ *and* $\tau(s_0) = \tau_0$ *and* $\big(u(s), \psi^*(s), \lambda(s), \tau(s)\big)$ *satisfies (1.2.13) for all s such that* $|s - s_0| < \rho_0$.

1.3 Numerical Methods

Having established the existence of fold paths, we now turn our attention to numerical methods we can use to trace them out. Equation (1.1.1) allows problems of a quite general nature to be treated. In order that we may solve these numerically, we assume a suitable discretization of (1.1.1) exists so that we may approximate the solution in a finite dimensional space. Thus, (1.1.1) takes the form

$$G_h(u_h, \lambda, \tau) = 0 \tag{1.3.1}$$

where $G_h: \mathbb{R}^N \times \mathbb{R} \times \mathbb{R} \to \mathbb{R}^N$. For simplicity we now drop the subscript h for the remainder of this section.

Written in its finite-dimensional form, the system of equations we wish to solve is

$$G(u, \lambda, \tau) = 0 \tag{1.3.2a}$$

$$G_u^T \psi = 0 \tag{1.3.2b}$$

$$G_\lambda^T \psi - 1 = 0 \tag{1.3.2c}$$

$$\begin{aligned} &\dot{u}^T(s_0)\big[u(s) - u(s_0)\big] + \dot{\lambda}(s_0)\big[\lambda(s) - \lambda(s_0)\big] \\ &\quad + \dot{\tau}(s_0)\big[\tau(s) - \tau(s_0)\big] - (s - s_0) = 0 \end{aligned} \tag{1.3.2d}$$

The numerical method we will use is the Euler-Newton pseudo-arclength continuation due to Keller [17,18]. There are three basic steps in applying this technique to trace out folds. The first is to locate a starting point for the continuation. This involves using pseudo-arclength continuation on one-parameter problems like (1.1.2), noting where a fold occurs and then accurately determining the solution at the fold. This yields the starting solution $[u(s_0), \psi(s_0), \lambda(s_0), \tau(s_0)]$. Then comes the continuation step in which we will obtain a solution some distance away on the solution path. It has two parts: the Euler step and the Newton iteration. To

perform the Euler step we calculate the tangent vector to the solution path. If we let $\dot{T}(s_0)$ denote the tangent vector and $X(s_0)$ the solution of (1.3.2) at the starting point, then $X(s_0) + \dot{T}(s_0)\Delta s$ provides an approximation to the solution a distance Δs away on the solution path. This approximation is then used as the starting point for the Newton iteration, which will accurately determine the next solution on the path. These last two steps are then repeated to trace out the solution path as far as one desires.

We now describe the numerical methods employed in each of these steps. A fold is typically encountered in the course of carrying out pseudo-arclength continuation on problems of the form (1.1.2). As a fold is passed, a change in the sign of both $\det(G_u)$ and $\dot{\lambda}(s)$ occurs. The pair of solutions for which the sign change was observed mark the endpoints of an interval on the solution path in which a fold lies.

With the location of the fold narrowed down, we have a couple of methods available to us for accurately locating the fold. Since the fold is a solution of the inflated systems (1.2.2) and (1.2.3), we could use one of the endpoint solutions as an initial guess and employ Newton's method to solve either system for the fold. Moore and Spence [36] have carried out this procedure for (1.2.3), and Jepson and Spence [12] have presented another algorithm for solving equations involving the Jacobian of systems of that form. Alternatively, we could use a root solver on the scalar function $\dot{\lambda}(s)$ and locate its root in the interval between the two endpoint solutions, since $\dot{\lambda}(s) = 0$ at a fold (cf. equation (1.1.6)). This procedure was outlined by Keller [18].

For our work we have chosen to employ the second method. It is relatively easy to implement, and its usage avoids having to build into our code the extra machinery necessary to carry out the factorization of the Jacobians of (1.2.2) or (1.2.3), which is different than the technique used to factor the Jacobian of (1.3.2).

To describe the procedure we now introduce the notation of Keller [18]. Let the branch of solutions of the system (1.1.2), (1.1.3b) containing the endpoint solutions be denoted by $\Gamma(s)$, where s is the true arclength. We define one of the endpoint solutions to be $[u(s_0), \lambda(s_0)]$, where $[u, \lambda]$ is a solution on $\Gamma(s)$ parametrized by the arclength. Since the numerical solutions are calculated using pseudo-arclength, we introduce a solution point $[v, \xi]$ on $\Gamma(s)$ parametrized by the pseudo-arclength σ. This solution satisfies the equations

$$G(v, \xi) = 0 \tag{1.3.3a}$$

$$\dot{u}_0^T[v - u_0] + \dot{\lambda}_0[\xi - \lambda_0] - (\sigma - s_0) = 0 \tag{1.3.3b}$$

where $u_0 \equiv u(s_0)$, $\lambda_0 \equiv \lambda(s_0)$, etc., $\dot{} \equiv d/ds$, and we define $\sigma_0 \equiv s_0$. The other endpoint solution is given by $[v(\sigma_1), \xi(\sigma_1)] \equiv [u(s_1), \lambda(s_1)]$, and the value of $\sigma_1 - \sigma_0$ is known from the continuation procedure used to obtain the endpoint solutions. Also known are the tangent vectors $[\dot{u}(s_0), \dot{\lambda}(s_0)]$ and $[\dot{u}(s_1), \dot{\lambda}(s_1)]$ at the two endpoints, and the fact that $\dot{\lambda}(s_0)\dot{\lambda}(s_1) < 0$. Therefore, there is a point $s^* \in (s_0, s_1)$ such that $\dot{\lambda}(s^*) = 0$, and this point is the fold.

In [18] it is shown that $\dot{\lambda}(s)$ and $\xi'(\sigma)$ have the same sign, where $' \equiv d/d\sigma$. So to locate the fold, it is only necessary to find the point σ^* for which $\xi'(\sigma^*) = 0$. But to do this we must first be able to calculate $\xi'(\sigma)$. Since $(d\sigma/ds)_{s=s_0} = 1$, we have that $[v'(\sigma_0), \xi'(\sigma_0)] = [\dot{u}(s_0), \dot{\lambda}(s_0)]$. But for any other value of σ, we need to solve

$$G_u(\sigma)v'(\sigma) + G_\lambda(\sigma)\xi'(\sigma) = 0 \tag{1.3.4a}$$

$$\dot{u}_0^T v'(\sigma) + \dot{\lambda}_0 \xi'(\sigma) = 1, \tag{1.3.4b}$$

which were obtained by differentiating (1.3.3) with respect to σ. If we define $\phi(\sigma)$ by

$$G_u(\sigma)\phi(\sigma) = -G_\lambda(\sigma) \tag{1.3.5}$$

for G_u nonsingular, and by

$$G_u(\sigma)\phi(\sigma) = 0$$

for G_u singular, then we have that

$$v'(\sigma) = \xi'(\sigma)\phi(\sigma) \tag{1.3.6a}$$

$$\xi'(\sigma) = [\dot{u}_0^T\phi(\sigma) + \dot{\lambda}_0]^{-1}. \tag{1.3.6b}$$

To solve for σ^*, we use a combination of the secant method and *regula falsi*. With σ_0 and σ_1 known to surround the fold, we start off by employing the secant method:

$$\sigma_{j+1} = \sigma_j - \xi'_j \frac{\sigma_j - \sigma_{j-1}}{\xi'_j - \xi'_{j-1}}. \tag{1.3.7}$$

where $\xi'_j \equiv \xi'(\sigma_j)$, etc. To ensure the quickest convergence we wish to enforce that all new iterates fall between the two previous iterates which form the smallest interval containing the fold. Let this interval be denoted by (σ_k, σ_j), where j marks the current iterate and σ_k is the most recent iterate for which $\xi'_j\xi'_k < 0$. If (1.3.7) yields a value outside this interval, we replace that σ_{j+1} with the *regula falsi* iterate

$$\sigma_{j+1} = \frac{\xi'_j\sigma_k - \xi'_k\sigma_j}{\xi'_j - \xi'_k}, \tag{1.3.8}$$

which will lie in (σ_k, σ_j). With the value of σ_{j+1} so chosen, we wish to calculate $\xi'(\sigma_{j+1})$. For this we will need to know $v(\sigma_{j+1})$ and $\xi(\sigma_{j+1})$. We obtain these by solving (1.3.3) by the usual Newton iteration (see Keller [17] or [18]). For initial guesses we use linear interpolations of $v(\sigma)$ and $\xi'(\sigma)$. The expression for $\xi'(\sigma)$ is

$$\xi'(\sigma) \approx \xi'(\sigma_k) - (\sigma - \sigma_k)\frac{\xi'(\sigma_j) - \xi'(\sigma_k)}{\sigma_j - \sigma_k}.$$

Integrating with respect to σ and evaluating at $\sigma = \sigma_k$ to determine the constant of integration, we obtain a quadratic interpolant for $\xi(\sigma)$. Thus, for initial guesses

we use

$$v^{(0)}(\sigma_{j+1}) = \theta v(\sigma_j) + (1-\theta)v(\sigma_k) \tag{1.3.9a}$$

$$\begin{aligned}\xi^{(0)}(\sigma_{j+1}) &= \xi(\sigma_k) + (\sigma_{j+1} - \sigma_k)\xi(\sigma_k) \\ &\quad + \tfrac{1}{2}\theta(\sigma_{j+1} + 3\sigma_k)[\,\xi'(\sigma_j) - \xi'(\sigma_k)\,]\end{aligned} \tag{1.3.9b}$$

where

$$\theta = \frac{\sigma_{j+1} - \sigma_k}{\sigma_j - \sigma_k}. \tag{1.3.10}$$

Once we have solved for $v(\sigma_{j+1})$ and $\xi(\sigma_{j+1})$, we may solve (1.3.6) to obtain $\xi'(\sigma_{j+1})$. Note that this is particularly cheap to do since, in the last Newton iteration, we solved the equation

$$G_u(v^{(\nu)}, \xi^{(\nu)})y = -G_\lambda(v^{(\nu)}, \xi^{(\nu)}),$$

where $v^{(\nu)} \to v(\sigma_{j+1})$ and $\xi^{(\nu)} \to \xi(\sigma_{j+1})$. Thus, y is essentially equal to $\phi(\sigma_{j+1})$, and so we need not solve (1.3.5). If $|\xi'(\sigma_{j+1})|$ is sufficiently small, the fold is located and we stop. If not, we update the value of k and iterate again.

With the fold accurately located, we are ready to begin continuation on the extended system. The first step is to calculate the tangent vector. Differentiating (1.3.2a–c) with respect to s we obtain

$$G_u^0 \dot{u}_0 + G_\lambda^0 \dot{\lambda}_0 + G_\tau^0 \dot{\tau}_0 = 0 \tag{1.3.11a}$$

$${G_{uu}^0}^T \psi_0 \dot{u}_0 + {G_u^0}^T \dot{\psi}_0 + {G_{u\lambda}^0}^T \psi_0 \dot{\lambda}_0 + {G_{u\tau}^0}^T \psi_0 \dot{\tau}_0 = 0 \tag{1.3.11b}$$

$${G_{\lambda u}^0}^T \psi_0 \dot{u}_0 + {G_\lambda^0}^T \dot{\psi}_0 + {G_{\lambda\lambda}^0}^T \psi_0 \dot{\lambda}_0 + {G_{\lambda\tau}^0}^T \psi_0 \dot{\tau}_0 = 0. \tag{1.3.11c}$$

These combined with the arclength condition

$$\|\dot{u}_0\|^2 + \dot{\lambda}_0^2 + \dot{\tau}_0^2 = 1 \tag{1.3.12}$$

provide the equations necessary to solve for the tangent vector $[\dot{u}_0, \dot{\psi}_0, \dot{\lambda}_0, \dot{\tau}_0]$. Recalling the notation of Lemma 1.2.14, (1.3.11) may be written as

$$A_0 \mathcal{T}_0 + b_0 \dot{\tau}_0 = 0,$$

where $\mathcal{T}_0 \equiv (\dot{u}_0 \quad \dot{\psi}_0 \quad \dot{\lambda}_0)^T$. Since A_0 is nonsingular by Lemma 1.2.4, we may define $\mathcal{V}$ by

$$A_0 \mathcal{V} = -b_0, \tag{1.3.13}$$

and then $\mathcal{T}_0 = \dot{\tau}_0 \mathcal{V}$. Now, (1.3.12) may be written as

$$\| \mathcal{T}_0^{(1)} \|^2 + \mathcal{T}_0^{(3)\,2} + \dot{\tau}_0^2 = 1,$$

where $\mathcal{T}_0 \equiv (\mathcal{T}_0^{(1)} \quad \mathcal{T}_0^{(2)} \quad \mathcal{T}_0^{(3)})^T$. Thus, we have that

$$\dot{\tau}_0^2 \left[\| \mathcal{V}^{(1)} \|^2 + \mathcal{V}^{(3)\,2} + 1 \right] = 1,$$

from which we may solve for $\dot{\tau}_0$:

$$\dot{\tau}_0 = \pm \sqrt{\frac{1}{1 + \| \mathcal{V}^{(1)} \|^2 + \mathcal{V}^{(3)\,2}}}, \tag{1.3.14}$$

where the $\pm$ indicates that the tangent vector may point in the direction of either increasing or decreasing τ along the fold. The remainder of the tangent vector is given by

$$\begin{pmatrix} \dot{u}_0 \\ \dot{\psi}_0 \\ \dot{\lambda}_0 \end{pmatrix} = \dot{\tau}_0 \begin{pmatrix} \mathcal{V}^{(1)} \\ \mathcal{V}^{(2)} \\ \mathcal{V}^{(3)} \end{pmatrix}. \tag{1.3.15}$$

The majority of the work in calculating the tangent vector, then, is in solving (1.3.13). But this can be done efficiently by employing the method used to prove Lemma 1.2.4. Retracing those steps we obtain

$$\mathcal{V}^{(3)} = -\psi_0^T G_\tau^0 \tag{1.3.16a}$$

$$\mathcal{V}^{(1)} = \tilde{\xi}_0 + \alpha \phi_0 \tag{1.3.16b}$$

$$\mathcal{V}^{(2)} = \tilde{\eta}_0 + \beta \psi_0 \tag{1.3.16c}$$

where

$$G_u^0 \tilde{\xi}_0 = -G_\tau^0 - G_\lambda^0 \mathcal{V}^{(3)}, \qquad \psi_0^T \tilde{\xi}_0 = 0, \tag{1.3.17}$$

$$\alpha = -\frac{\psi_0^T G_{u\tau}^0 \phi_0 + \psi^T G_{u\lambda}^0 \phi_0 \mathcal{V}^{(3)} + \psi^T G_{uu}^0 \tilde{\xi}_0 \phi_0}{\psi^T G_{uu}^0 \phi_0 \phi_0}, \tag{1.3.18}$$

$$G_u^{0\,T} \tilde{\eta}_0 = -\big(G_{u\tau}^{0\,T} \psi_0 + G_{u\lambda}^{0\,T} \psi_0 \mathcal{V}^{(3)} + (G_{uu}^0 \mathcal{V}^{(1)})^T \psi_0\big), \qquad \phi_0^T \tilde{\eta}_0 = 0, \tag{1.3.19}$$

and

$$\beta = -\big(\psi_0^T G_{\lambda\tau}^0 + \psi_0^T G_{\lambda\lambda}^0 \mathcal{V}^{(3)} + \psi_0^T G_{\lambda u}^0 \mathcal{V}^{(1)} + \tilde{\eta}_0^T G_\lambda^0\big). \tag{1.3.20}$$

Performing these steps is very inexpensive. For instance, the LU-decomposition of G_u^0 (and also of $G_u^{0\,T}$ if the proper LU-solver is used) is already available to us. If this is the first Euler step, then we may use the factorization from the last Newton iteration that was performed to locate the starting fold point accurately. If this is a subsequent Euler step, then in using Newton's method to solve (1.3.2) at $s = s_0$, G_u^0 was factored during each iteration, and we may use the factorization from the last iteration. In any case, the most costly part of the procedure has already been carried out.

This leaves as the most expensive steps of the calculation the solution of (1.3.17) and (1.3.19), and the calculation of ψ_0 (for the first Euler step only) and ϕ_0. But using the techniques due to Keller [19], each of these calculations only requires half a backsolve. Note also that the particular form of the constraints which are the second equations of (1.3.17) and (1.3.19) is unimportant. We only need to make $\tilde{\xi}_0$ and $\tilde{\eta}_0$ unique, and the methods of [19] do this for us. So for a problem where analytic derivatives are available, a typical Euler step will only require three half-backsolves and a hand full of inner products.

When derivatives must be calculated numerically, the situation can change depending on how costly the derivatives are to evaluate. If these calculations

are fairly cheap, then one will probably use Newton's method to solve the system. In this case the derivatives will be available from the last Newton iteration and so will not have to be recalculated to find the tangent vector. If, on the other hand, the derivative calculations are costly enough that the chord method, say, is used instead of Newton's method, then new derivatives must be calculated in order to solve for the tangent vector. In this case the tangent calculation can be as expensive as a chord iteration, and the various costs will have to be weighed against each other in order to determine the most efficient solution strategy.

This brings us to the solution phase of the continuation procedure. Here we are going to have to solve systems involving the Jacobian of (1.3.2). We solve once if we decide to use the chord method, and we solve at every iteration if Newton's method is used. The Jacobian we wish to invert is

$$\begin{pmatrix} G_u & O & G_\lambda & G_\tau \\ (G_u^T\psi)_u & G_u^T & G_{u\lambda}^T\psi & G_{u\tau}^T\psi \\ G_{\lambda u}^T\psi & G_\lambda^T & G_{\lambda\lambda}^T\psi & G_{\lambda\tau}^T\psi \\ \dot{u}_0^T & 0 & \dot{\lambda}_0 & \dot{\tau}_0 \end{pmatrix} \tag{1.3.21}$$

One way to solve a system of this form is to partition it into 2×2 blocks as it stands. One may then apply the bordering algorithm (block Gaussian elimination) to solve it. And even when the system is evaluated at a fold, where, as is easily shown, the upper left hand 2×2 block becomes singular with a null space of dimension two, the algorithm is still applicable, as has been shown by Keller [20]. However, solving systems involving that upper left hand block does present a significant problem. With both G_u and G_u^T singular, this system cannot be partitioned again, and its solution would thus require treating it as a single matrix with dimensions twice that of G_u. For most problems, where G_u is both

large and banded, the cost of this would be prohibitive.

So instead, we use a trick based on an idea due to Rheinboldt [39]. We move row four to the position following row one and interchange columns two and three. This leads to a natural partitioning of the Jacobian as

$$\left(\begin{array}{cc|cc} G_u & G_\lambda & O & G_\tau \\ \dot{u}_0^T & \dot{\lambda}_0 & 0 & \dot{\tau}_0 \\ \hline G_{uu}^T \cdot \psi & G_{u\lambda}^T \psi & G_u^T & G_{u\tau}^T \psi \\ G_{\lambda u}^T \psi & G_{\lambda\lambda}^T \psi & G_\lambda^T & G_{\lambda\tau}^T \psi \end{array}\right) \equiv \left(\begin{array}{c|c} A & B \\ \hline C & D \end{array}\right). \tag{1.3.22}$$

Thus, a typical system involving (1.3.22) is

$$A\xi + B\eta = r \tag{1.3.23a}$$

$$C\xi + D\eta = \rho. \tag{1.3.23b}$$

The procedure we propose for solving systems of this form is this: Define Y and z by $AY = B$ and $Az = r$. Then using (1.3.23a) we have that $\xi = z - Y\eta$. Substituting this into (1.3.23b) yields

$$(D - CY)\eta = \rho - Cz. \tag{1.3.24}$$

Thus, solving (1.3.23) only requires solving systems involving A and $(D - CY)$.

Now, A is of the same form as the systems to which Keller applied his bordering algorithm (see [17] or [18]). So, solving for z only requires one LU-decomposition of G_u and two backsolves. Letting $r \equiv \left(r^{(1)^T} \quad r^{(2)}\right)^T$ and $z \equiv \left(z^{(1)^T} \quad z^{(2)}\right)^T$ and defining ω and ς by $G_u\omega = G_\lambda$ and $G_u\varsigma = r^{(1)}$, we obtain

$$z^{(2)} = \frac{r^{(2)} - \dot{u}_0^T\varsigma}{\dot{\lambda}_0 - \dot{u}_0^T\omega}, \qquad z^{(1)} = \varsigma - z^{(2)}\omega. \tag{1.3.25}$$

Since G_u becomes (nearly) singular as the Newton iterations converge, if one is not careful, trouble can arise from using the bordering algorithm to solve

systems involving A. Chan [4] has pointed out that, as the smallest pivot of G_u approaches zero, the bordering algorithm becomes inaccurate. But if one requires that the absolute value of this pivot never falls below $O(\epsilon_M^{1/2})$, where ϵ_M is the machine epsilon, the results obtained from the bordering algorithm, as is evident from Chan's figures, will remain accurate to $O(\epsilon_M^{1/2})$ even near the singular point (see Keller's analysis in [19]). We call this "enforcing" round-off, and have used it in our calculations as the accuracy in double precision arithmetic has proved sufficient.

Due to the choice of (1.3.3b) instead of (1.2.12) as the pseudo-arclength condition, all but the last column of B, and hence Y, are identically zero. Therefore, solving for the matrix Y requires the same amount of work as solving for a vector. And since the LU-decomposition of G_u is already available and ω has been calculated, this only takes one more backsolve. Letting the last column of Y be denoted by $\left(y^{(1)^T} \quad y^{(2)} \right)^T$ and defining $\tilde{\zeta}$ by $G_u \tilde{\zeta} = G_\tau$, we have that

$$y^{(2)} = \frac{\dot{\tau}_0 - \dot{u}_0^T \tilde{\zeta}}{\dot{\lambda}_0 - \dot{u}_0^T \omega}, \qquad y^{(1)} = \tilde{\zeta} - y^{(2)} \omega. \tag{1.3.26}$$

To evaluate $(D - CY)$ we must first calculate the product CY. This has the same form as Y. In fact,

$$CY = \begin{pmatrix} O & (G_{uu}^T y^{(1)} \psi + G_{u\lambda}^T \psi y^{(2)}) \\ 0 & (G_{\lambda u}^T \psi y^{(1)} + G_{\lambda\lambda}^T \psi y^{(2)}) \end{pmatrix} \equiv \begin{pmatrix} O & e^{(1)} \\ 0 & e^{(2)} \end{pmatrix},$$

so that

$$D - CY = \begin{pmatrix} G_u^T & (G_{u\tau}^T \psi - e^{(1)}) \\ G_\lambda^T & (G_{\lambda\tau}^T \psi - e^{(2)}) \end{pmatrix}.$$

Therefore, applying the bordering algorithm to $(D - CY)$ will not require another LU-decomposition. Only two backsolves are needed. If we let $\eta \equiv \left(\eta^{(1)^T} \quad \eta^{(2)} \right)^T$,

$\rho \equiv \left(\rho^{(1)\,T} \quad \rho^{(2)} \right)^T$ and $Cz \equiv \left(f^{(1)\,T} \quad f^{(2)} \right)^T$, and define ω' and ς' by $G_u^T \omega' = G_{u\tau}^T \psi - e^{(1)}$ and $G_u^T \varsigma' = \rho^{(1)} - f^{(1)}$, then

$$\eta^{(2)} = \frac{\rho^{(2)} - f^{(2)} - G_\lambda^T \varsigma'}{G_{\lambda\tau}^T \psi - e^{(2)} - G_\lambda^T \omega'}, \qquad \eta^{(1)} = \varsigma' - \eta^{(2)} \omega', \tag{1.3.27}$$

and finally

$$\xi = z - Y\eta = \begin{pmatrix} z^{(1)} - y^{(1)} \eta^{(2)} \\ z^{(2)} - y^{(2)} \eta^{(2)} \end{pmatrix}. \tag{1.3.28}$$

Thus, systems involving (1.3.22) can be solved with only one LU-decomposition, five backsolves and several inner products.

Of course, the preceding requires that the steps involved in solving the system with this partitioning can be carried out. In particular, one needs to solve systems with the matrices A and $D - CY$. Using Keller's Lemma 2.8 and the fact that the entire Jacobian is nonsingular, one can show that if A is nonsingular, then $D - CY$ is, too. Thus, when A is nonsingular, the partitioning is valid and this algorithm yields the correct solution to systems involving the Jacobian. But what happens when A is singular? As we shall see, the surprising answer to this is that with only a minor modification the algorithm still works!

Let's consider what can happen to make A singular. First, we look at the case when G_u is nonsingular. Once again making use of Lemma 2.8, we find that A is singular only if $\dot{\lambda}_0 - \dot{u}_0^T G_u^{-1} G_\lambda = 0$. In performing the calculations with finite precision arithmetic, one would expect that, due to round-off errors, we would actually have that $\dot{\lambda}_0 - \dot{u}_0^T G_u^{-1} G_\lambda = \epsilon$, where ϵ is a small quantity. (If this were not true, for example, in a problem where $\dot{u}_0^T \equiv 0$ and $\dot{\lambda}_0 \equiv 0$, we could make it true by enforcing round-off.) Applying the algorithm with this nonzero ϵ, we find exactly the same type of cancellation of the ϵ^{-1} terms as occurs when the bordering algorithm is applied to systems involving a singular matrix (see Keller [19] or [20]

for a detailed account of what happens in the case of the bordering algorithm). The result is that we get the correct solution accurate to $O(\epsilon, \epsilon_M/\epsilon)$. To maximize the accuracy, then, we should choose $\epsilon = \epsilon_M^{1/2}$, which balances the errors due to the imperfect cancellation of the ϵ^{-1} terms with finite precision arithmetic and the introduction of a nonzero ϵ. That we cannot retain full accuracy is a reflection of the fact that we are working with an ill-conditioned matrix system. But by looking at the problem in a different way, we can make the system better conditioned and obtain more accurate results.

By enforcing round-off we are essentially changing the value of $\dot{\lambda}_0$ (or $\dot{u}_0$) by a small amount. This has the effect of modifying our definition of pseudo-arclength so that s now measures distance along a vector close to the tangent vector. As long as the curvature of the fold path is not too great, this new s will work just as well as the normal pseudo-arclength; and even when the curvature is big, reducing the continuation step sizes a little bit will take care of any problems that could arise. This remains true even for values of ϵ larger than that given above, as long as the nearby tangent vector we are specifying does not differ from the true tangent vector by too much. So we may choose ϵ larger than $\epsilon_M^{1/2}$ in order to better condition the matrix A. The solution we obtain will differ by $O(\epsilon)$ from what we would have obtained had we solved with the original definition of pseudo-arclength, but this merely indicates that we are solving at a slightly different location on the fold path. Of course, the new definition of pseudo-arclength will have to remain in effect throughout subsequent Newton iterations until we have converged to the solution. But we may return to the normal definition in the next continuation step if A is no longer singular.

The other case in which A can become singular is actually the more important case to consider. This is when G_u is singular, or nearly singular, and is more important because as we converge to a solution of (1.3.2), G_u will become singular.

One more application of Lemma 2.8 shows that the condition necessary for A to be singular in this case is that $\dot{u}_0^T \in \mathcal{R}(G_u^T)$, i.e., $\dot{u}_0^T \Phi = 0$, where Φ is the (unit) null vector of G_u. Here we have made use of the fact that $G_\lambda \notin \mathcal{R}(G_u)$. Letting Ψ^T denote a left null vector of G_u, we see that this is true if we are sufficiently close to a solution since $G_\lambda^T \psi = 1$ and $\Psi \to \psi$ (to within a nonzero multiplicative constant) as we approach a solution.

We deal with this case just as we did the last one. We replace $\dot{u}_0^T$ with $\dot{u}_0^T + \epsilon\Phi$, thus modifying the pseudo-arclength definition. Retaining this definition of pseudo-arclength in subsequent iterations, we will obtain a more accurate solution to (1.3.2) due to the better conditioned A matrix.

In practice, we have always employed Newton's method to solve the nonlinear system instead of the chord method. Therefore, we have chosen to ignore the first type of singularity since normal round-off errors should suffice in dealing with it. And even if we lose some accuracy in doing so, this is of little consequence since this case could only occur in an early iteration; the final iterations will have G_u nearly singular. Of course, if the chord method is used, this case should be tested for explicitly. We test for the second case by computing $\dot{u}_0^T \Phi$ during each application of the algorithm. If this quantity is sufficiently small, we then modify $\dot{u}_0^T$ as above and continue. But in the course of all our work with this algorithm on real problems (e.g., the flow between rotating, coaxial disks), we have yet to encounter a singular A matrix.

1.4 Comparison To Other Methods

To conclude this chapter we shall compare the present method to other methods for tracing out folds. The simplest approach is just to make use of standard continuation methods for single parameter problems. Holding one parameter fixed, solution branches are traced out as a function of the other parameter. The loca-

tions of folds are noted as they are passed. The parameter held fixed is then varied and the process repeated. Finally, the fold paths are constructed from the locations noted on the cross sections of the solution surface. This was the method used by Szeto [43] to map out the solution sheets and folds of the flow between two infinite, rotating, coaxial disks. It is an easy method to use since it requires no new machinery to be added to existing continuation codes. But in order to resolve features along the folds such as cusps, many cross sectional slices need to be computed, and so the method can be costly. In addition, if one simply wishes to compute a particular fold, it is not easy to set up an efficient procedure to do this automatically.

To overcome these problems it is natural to consider extended systems which have as their solutions the fold paths. This, of course, is the basis for the present method, as well as those of Rheinboldt [39] and Jepson and Spence [12]. But in spite of starting out with the same basic idea, the implementations of the three methods are quite different. The present method, which was discussed in detail in the previous section, uses the system (1.2.13). The methods of Rheinboldt and Jepson and Spence both start off with the extended system (1.2.3). To this Jepson and Spence append the pseudo-arclength condition (1.2.12), while Rheinboldt appends a condition specifying in which of the parameters or solution components the continuation is proceeding.

To solve his system Rheinboldt employs a particular choice for the scaling condition (1.2.3c) which allows the Jacobian of his extended system to be written as a rank one modification of a matrix which is easy to invert. But with this choice of scaling, the Jacobian system to be solved is singular under some conditions. In addition, use of this scaling requires modifications in his standard continuation process which force smaller continuation steps to be made. Nevertheless, Rheinboldt has used his method effectively on problems of small to moderate size.

However, he has concluded that his implementation is not suitable for problems where N, the number of equations in G, is large.

Jepson and Spence present a method for solving systems involving matrices of the same form as the Jacobian of (1.2.3). Their algorithm assumes that G_u is singular, or nearly singular, whenever this Jacobian-like system is solved. To implement the fold following, however, pseudo-arclength continuation is used, which has the effect of adding an extra row and column to the system. Fortunately, this larger system may be solved with only moderate additional expense by using, for example, the bordering algorithm.

	Present Algorithm	Jepson & Spence	Rheinboldt
LU-Decompositions	1	1	1
Triangular System Solutions	10	15	16
Matrix-Vector Multiplications	2	4	2

Table 1.1. A comparison of the major operations necessary to carry out a Newton iteration for the three fold following methods.

In Table 1.1 we compare the operation counts of the three methods. We have included the most significant operations in the three algorithms, namely, the LU-decomposition of G_u, the backsolves necessary to solve equations involving G_u (a backsolve consists of two triangular system solutions), and matrix-vector multiplications of order N.

In compiling this table, certain assumptions have been made. We have assumed that for the present method an LU-solver which can solve systems involving both the original matrix and its transpose is available. (Note that the LINPACK routines provide this capability [7].) Neither Rheinboldt nor Jepson and Spence present complete algorithms for solving their extended systems. Rheinboldt states

that solution of his system can be accomplished by solving four N+1 $\times$ N+1 systems. We have assumed the use of the bordering algorithm to solve these four systems since it is very efficient in the typical case where G_u is banded. We have also combined the algorithm presented by Jepson and Spence with the bordering algorithm so that pseudo-arclength continuation may be employed.

As can be seen from the table, the present method costs several triangular system solutions less than either of the other methods. When cummulated over a few Newton iterations at many continuation points, this can add up to quite a big savings. It certainly is a great deal more efficient than the cross section technique when one takes into consideration the extra points which must be calculated in each cross section and the iterative procedure needed to then locate the folds accurately. In addition, properly resolving the fold path is readily built into the continuation process, something which can only be achieved by human intervention in the cross section method.

In actual use we have found the present method to be quite efficient and effective. The results of its use in the calculation of the flow between two infinite, rotating, coaxial disks is presented in Chapter 2.

CHAPTER 2

The Flow Between Rotating, Coaxial Disks

As an example of the use of fold continuation, we calculate the solution surface for the problem of fluid flow between two infinite, rotating, coaxial disks.

2.1 Introduction

In 1921, von Kármán [46] introduced a similarity transformation which reduced the Navier-Stokes equations describing the steady flow of an incompressible, viscous fluid over an infinite, rotating plane to a system of ordinary differential equations. In 1951, Batchelor [1] used this transformation to study the flow between two infinite, rotating, coaxial disks and conjectured what the behavior of the flow would be for various values of γ, the ratio of the speeds of the two disks, as the Reynold's number, R, becomes large. The distinguishing characteristic of his solutions for $\gamma \leq 0$ was that the main body of the fluid is rotating, and transitions between regions of different rotational rates take place in narrow layers. Responding to this work, Stewartson [41] offered a different opinion as to the behavior of the flow for $\gamma \leq 0$. He claimed that the main body of the fluid has essentially no angular velocity, and he provided experimental evidence to support his claim. As a result of this controversy, as well as the fact that the similarity solution provides a rare exact solution of the Navier-Stokes equations, the flow between rotating disks has become a subject of great interest.

In 1962, Lance and Rogers [28] solved the system of nonlinear ordinary dif-

ferential equations numerically and provided solutions for various values of γ and R. Pearson [38] integrated the time-dependent equations and found steady solutions for counter-rotating disks and the case of one disk at rest. This case was also the subject of a more extensive numerical study by Mellor, Chapple and Stokes [34]. Integrating the steady-state equations, they found several different solution branches, differentiating between them by the number of cells in each solution, where a cell is defined as a region bounded by planes parallel to the disks on which the axial velocity of the fluid vanishes. Mellor, *et al.* found one-, two- and three-cell solutions. Nguyen, Ribault and Florent [37] also performed calculations for the case of one disk rotating and one at rest, applying various amounts of suction or blowing at the stationary disk. From their results they concluded that there is a unique solution for small values of R. The solution branches of Mellor, *et al.* were reproduced by Roberts and Shipman, who also found other solutions including a five-cell branch for values of R near 5000. Holodniok, Kubíček and Hlaváček [10] used Newton's method to perform a systematic search for solutions at $R = 625$. They found five solution branches and also concluded that a unique solution exists for small R. In 1978, Wilson and Schryer [45] used the time dependent equations to find steady-state solutions for large R, $\gamma = 0$, and various values of suction at the rotating disk. Also in 1978, Szeto [43] performed the most complete numerical study yet of the problem. Using the technique of pseudo-arclength continuation, he mapped out features of the solution surface for all values of γ ($-1 \leq \gamma \leq 1$) and Reynold's number up to 1000. In particular, he reported up to 19 different solutions in some regions of the (R,γ)-plane. Finally, Holodniok, *et al.* [11], in a continuation of their previous work, reproduced many of Szeto's solutions for $R = 625$ and $\gamma = 1, 0$ and -1.

In addition to the numerical studies, there have been theoretical and analytic investigations. McLeod and Parter [33] proved the existence of a solu-

tion for $\gamma = -1$ and provided estimates of the behavior of the solution as $R \rightarrow \infty$. Tam [44] and Matkowsky and Siegmann [32] found asymptotic solutions for large R. Matkowsky and Siegmann noted that the properties of their solution were in precise agreement with the estimates of McLeod and Parter. Kreiss and Parter [25,26,27] have written a series of papers in which they describe the shapes of the solutions to the governing equations in the limit of large Reynold's number. They have dealt with solutions which decay, are bounded, and which grow as the Reynold's number increases. These growing solutions are of particular note and we will have more to say about them later when we compare them to our numerical results.

Despite all this work, the controversy between the conjectures of Batchelor and Stewartson has not been completely resolved. Numerical solutions of both Batchelor and Stewartson type have been reported for $\gamma = 0$. For $\gamma = -1$ a solution of Stewartson type has been found both numerically [37,43,11] and analytically [32], but none of Batchelor type has been found.

Owing to the great number of solution branches and the complexity of the solution surface, this problem provides an ideal test for the fold continuation method described in Chapter 1. Here, using fold continuation to aide in its calculation and description, we have carried out a complete investigation of the solution surface for $R \leq 1000$. In addition to providing independent confirmation of most of the results of Szeto, we have been able to resolve the features of the solution surface much more accurately than heretofore possible, located folds and solutions not previously reported, and have completely described the structure of the solution surface.

In the next section we will formulate the problem and describe the numerical procedure used to integrate the differential equations. Then we will present the methods used to map out the solution surface and describe its structure. Finally,

we will indicate the locations of the solutions found by the previous investigators of this problem.

2.2 Problem Formulation

We consider the flow between two infinite, rotating, coaxial disks. Let d be the disk spacing so that in the cylindrical coordinates (r, θ, z) the lower disk lies in the plane $z = 0$ and the upper disk in the plane $z = d$. The angular velocity of the lower disk will be denoted by Ω_0 and that of the upper disk by Ω_1. The disk speed ratio is $\gamma \equiv \Omega_1/\Omega_0$. We non-dimensionalize the Navier-Stokes equations by dividing r and z by d, the velocities by $\Omega_0 d$, and the pressure by $\rho(\Omega_0 d)^2$, where ρ is the density. We define the Reynold's number as $\mathrm{R} \equiv \Omega_0 d^2/\nu$, where ν is the kinematic viscosity.

Now we seek a solution to the equations in the form of similarity variables. Following Szeto [43] we assume

$$u_z = f(z), \qquad u_r = -rf'(z)/2, \qquad u_\theta = rg(z). \tag{2.2.1}$$

When these are substituted into the Navier-Stokes equations we obtain

$$\begin{aligned} f'''' &= \mathrm{R}\,[ff''' + 4gg'] \\ g'' &= \mathrm{R}\,[fg' - gf'], \end{aligned} \tag{2.2.2}$$

where all quantities are now non-dimensional, so that the upper disk lies on $z = 1$.

The boundary conditions are $u_r = u_z = 0$, $u_\theta = 1$ at $z = 0$ and $u_r = u_z = 0$, $u_\theta = \gamma$ at $z = 1$. In terms of the similarity variables, these become

$$\begin{aligned} f(0) = f'(0) &= 0, \quad g(0) = 1, \\ f(1) = f'(1) &= 0, \quad g(1) = \gamma. \end{aligned} \tag{2.2.3}$$

As defined above, all solutions to this problem lie in the region $-1 \leq \gamma \leq 1$, since any solution with a value of γ such that $|\gamma| > 1$ is equivalent to a solution with $|\gamma| < 1$; this just corresponds to an interchange of the disks. To make this correspondence precise we quote a result due to Szeto [43]:

Lemma 2.2.4 *Denote a solution of (2.2.2-2.2.3) with* $\gamma \neq 0$ *by*

$$\mathcal{S} \equiv [f(z), g(z), \mathrm{R}, \gamma, \quad \text{on} \quad 0 \leq z \leq 1] .$$

Then

$$\hat{\mathcal{S}} \equiv \left[\hat{f}(\varsigma), \hat{g}(\varsigma), \hat{\mathrm{R}}, \hat{\gamma}, \quad \text{on} \quad 0 \leq \varsigma \leq 1\right],$$

where $\varsigma = 1 - z$, $\hat{\mathrm{R}} = |\gamma|\mathrm{R}$, $\hat{\gamma} = 1/\gamma$, $\hat{f}(\varsigma) = -f(z)/|\gamma|$ *and* $\hat{g}(\varsigma) = -g(z)/\gamma$ *is also a solution.*

Lemma 2.2.4 will play a very important part in obtaining a complete picture of the solution surface. As we shall see later, the solution surface consists of several disconnected sheets which cannot be obtained from one another by continuation in R or γ. Nevertheless, these sheets can be linked together, and the links are provided by Lemma 2.2.4.

The key to this is obtained by studying the special cases $\gamma = \pm 1$. For $\gamma = 1$, $\mathcal{S}$ and $\hat{\mathcal{S}}$ represent two distinct solutions unless $f(z)$ is antisymmetric and $g(z)$ is symmetric about $z = 1/2$. For $\gamma = -1$ the solutions are distinct unless both $f(z)$ and $g(z)$ are antisymmetric. If the appropriate symmetry conditions hold for a given solution, we shall simply say that the solution is *symmetric*. If they do not hold, then we shall say the solution is *antisymmetric*, and in this case all we need do is apply Lemma 2.2.4 and we will obtain a new solution.

To make Lemma 2.2.4 more useful when viewing plots of the fluid velocities, we now restate the result for the special cases $\gamma = \pm 1$. Namely, for $\gamma = 1$ $\mathcal{S}$ and $\hat{\mathcal{S}}$ represent two distinct solutions unless the axial velocity is antisymmetric and both

the radial and angular velocities are symmetric about $z = 1/2$. For $\gamma = -1$ the solutions are distinct unless both the axial and angular velocities are antisymmetric and the radial velocity is symmetric.

In order to use continuation methods to trace out the solution surface, we need a starting solution. Szeto [43] has pointed out the trivial solutions

$$f(z) \equiv 0, \quad g(z) = 1 + (\gamma - 1)z, \qquad \text{for R} = 0, \ \gamma \text{ arbitrary} \tag{2.2.5a}$$

$$f(z) \equiv 0, \quad g(z) = 1, \qquad \text{for } \gamma = 1, \text{ R arbitrary.} \tag{2.2.5b}$$

Note that (2.2.5b) just represents rigid body rotation.

To solve (2.2.2) we introduce the variable $h \equiv f''$. This allows us to rewrite (2.2.2) as a second order system of ordinary differential equations. Keller and Pereyra [22] have shown that it is more efficient to solve a system of this form as a second order system rather than converting it to a larger first order system. Therefore, the system we will be solving is

$$\begin{aligned} h'' &= \text{R}\,[fh' + 4gg'] \\ f'' &= h \\ g'' &= \text{R}\,[fg' - gf'], \end{aligned} \tag{2.2.6}$$

with the boundary conditions (2.2.3) left unchanged.

Keller and Pereyra [22] have also indicated that, in order to keep the difference scheme as compact as possible for an even order system, one needs to use a mesh which overlaps the solution interval. Thus, we set up the mesh by dividing the interval $[-\Delta z/2, 1 + \Delta z/2]$ into J equal subintervals, where $\Delta z = 1/(J - 1)$. We write the difference equations about the endpoints of the subintervals. Standard three-point formulae are used to approximate first and second derivatives of interior mesh points. The boundary conditions at $z = 0$ and $z = 1$ are approximated

by using the mesh points $j = 0$, $j = 1$ and $j = J - 1$, $j = J$, respectively, averaging for function values and differencing for derivatives. Thus, the discretization of (2.2.6, 2.2.3) is

$$\left.\begin{aligned} \frac{1}{2}(f_1 + f_0) &= 0 \\ \frac{1}{\Delta z}(f_1 - f_0) &= 0 \\ \frac{1}{2}(g_1 + g_0) &= 1 \end{aligned}\right\} \tag{2.2.7}$$

$$\left.\begin{aligned} \frac{h_{j+1} - 2h_j + h_{j-1}}{\Delta z^2} - \mathrm{R}\left[f_j \frac{h_{j+1} - h_{j-1}}{2\Delta z} + 4g_j \frac{g_{j+1} - g_{j-1}}{2\Delta z}\right] &= 0 \\ \frac{f_{j+1} - 2f_j + f_{j-1}}{\Delta z^2} - h_j &= 0 \\ \frac{g_{j+1} - 2g_j + g_{j-1}}{\Delta z^2} - \mathrm{R}\left[f_j \frac{g_{j+1} - g_{j-1}}{2\Delta z} - g_j \frac{f_{j+1} - f_{j-1}}{2\Delta z}\right] &= 0 \end{aligned}\right\} \tag{2.2.8}$$

$$\left.\begin{aligned} \frac{1}{2}(f_J + f_{J-1}) &= 0 \\ \frac{1}{\Delta z}(f_J - f_{J-1}) &= 0 \\ \frac{1}{2}(g_J + g_{J-1}) &= \gamma \end{aligned}\right\} \tag{2.2.9}$$

This, then, is the equation $G(u, \lambda, \tau) = 0$ to which we apply fold continuation and pseudo-arclength continuation. Here, $u = (h_0, f_0, g_0, \ldots, h_J, f_J, g_J)^T$, $\lambda = \mathrm{R}$ and $\tau = \gamma$. In the results that follow, a value of $J = 400$ has been used most of the time. For a few of the solutions, $J = 200$ proved sufficient, while for those on top of fold L, $J = 800$ was necessary.

2.3 The Solution Surface

Now we describe the solution surface and the techniques used to map it out. Figure 2.1 is a plot of the (R,γ)-plane showing the folds found in the solution

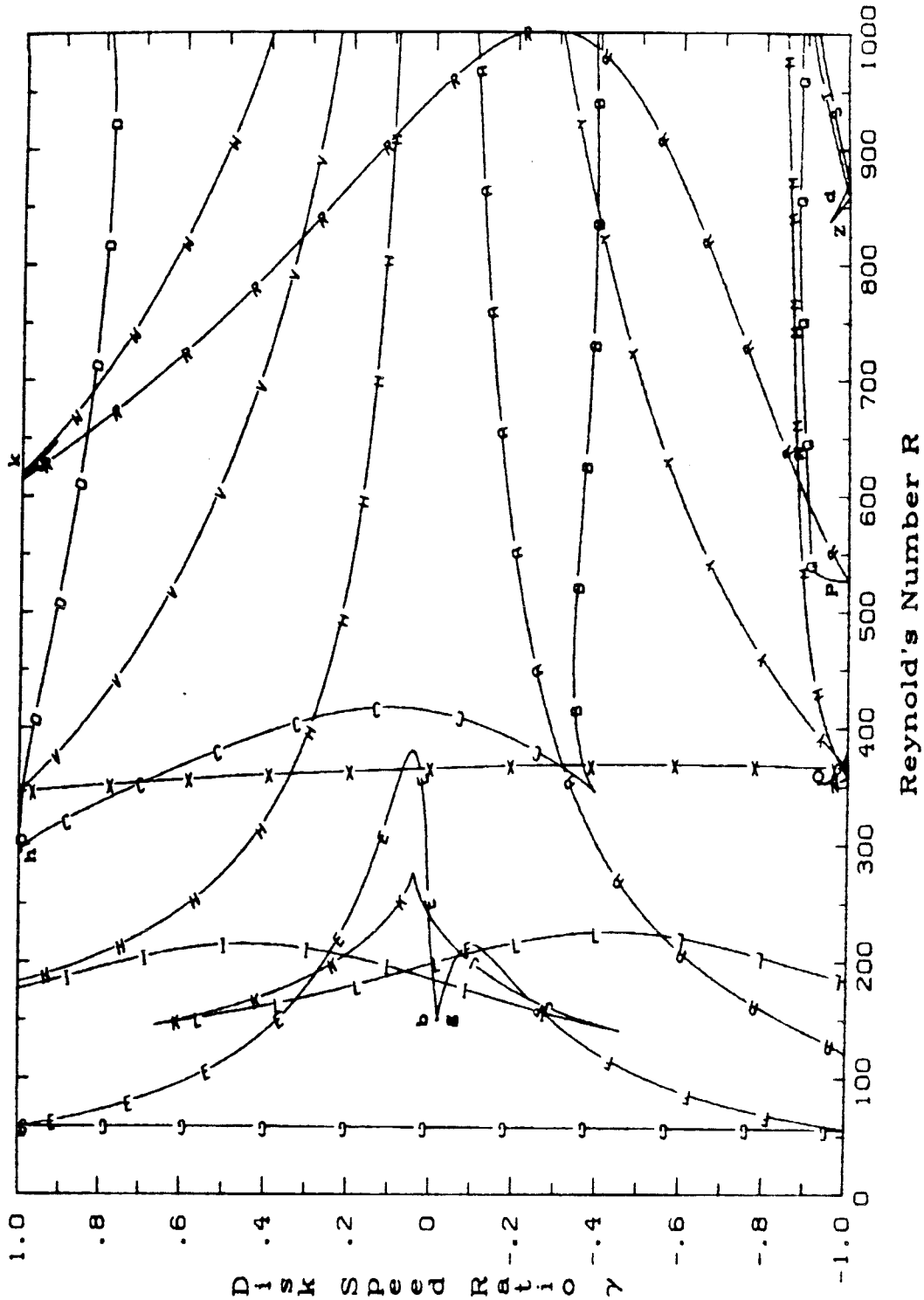

Figure 2.1. A plot of the folds in the solution surface of the equations describing the flow between rotating, coaxial disks.

surface of (2.2.6). Each fold has been labeled by an upper or lower case letter. The picture is quite involved as it depicts the structure of six different sheets of solutions.

At this point we clarify what is meant by a sheet of solutions. For the moment we revert to general terminolgy. Let $(\lambda, \tau) \in \Omega$, a subset of $\mathbb{R} \times \mathbb{R}$. Then, a *solution sheet* is defined to be a connected set in $\mathbb{B} \times \mathbb{R}^2$, each element of which is a solution of $G(u, \lambda, \tau) = 0$. Thus, any solution is a member of one, and only one, solution sheet. Moreover, two solutions are on the same sheet if and only if either can be found from the other by continuation.

The numerical technique to trace out the solution sheet to which a given solution belongs, then, is straightforward. First, since we can only perform the calculation over a finite region of space, we define boundaries for the sheet, i.e., we specify the domain Ω. If the parameters λ and τ are restricted to some subset of the (λ,τ)-plane, then the boundaries of this domain will provide natural boundaries for the solution sheet. If this domain is unbounded, we imposed artificial limits on λ and τ to make it bounded.

Once these boundaries are defined, we begin calculating the solution sheet. Starting at the given solution, we pick a direction to continue in (λ constant, τ constant, or some combination of the two constant). Then we trace out the solution curve on either side of the starting solution using pseudo-arclength continuation to take us to the edges of the domain. This gives us a starting line of solutions from which we may construct the sheet. (Actual domain boundaries, as well as the natural boundaries marked by folds, are particularly convenient choices for a starting line.) Now we construct the sheet by using solutions spaced out along the starting line as starting points for new lines of solutions, each traced out in a direction normal to the starting line.

If no singular points are encountered as we trace out these transverse lines of

solutions, we conclude that the sheet is "flat," i.e., single-valued. (As we will see shortly, none of the solution sheets found for the flow between rotating, coaxial disks is flat.) But, if the solution sheet has any structure at all, we should certainly expect to encounter singularities. If we are lucky, the singularities will be obvious, i.e., we pass through a fold or bifurcation point as we trace out the transverse path. Sometimes, however, singularities are not so obvious.

Fortunately, there are ways to locate them, anyway. For instance, we may have noticed a point of inflection in the solution path as one of the transverse paths was traced out. This could be just an inflection point; but on the other hand, it could be an indication that two folds nearby have coalesced, forming a cusp (see fig. 2.2). We can check this out in two ways. First, we can add more transverse paths next to the one with the inflection point. If two folds coalesce nearby, we will pass through them or a pitchfork bifurcation point on a neighboring path. We have used this method to locate folds B and C (see fig. 2.1).

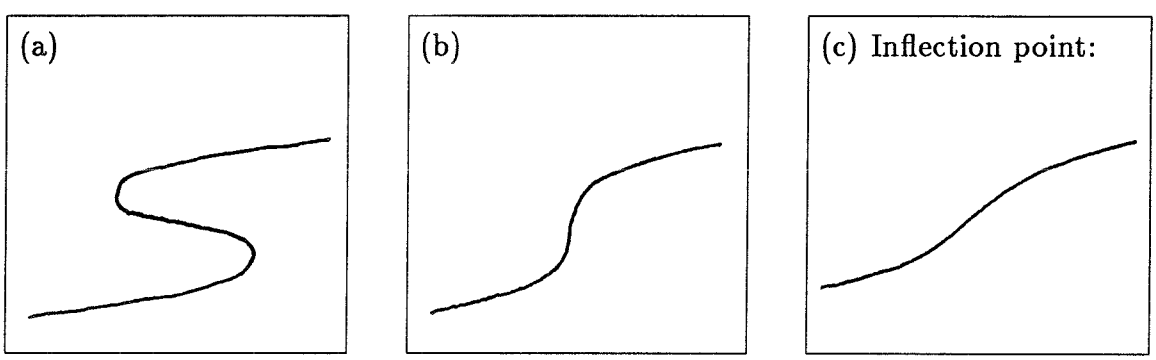

Figure 2.2. As one of the parameters, say γ, varies, two folds coalesce and the result is an inflection point in the solution path.

Alternatively, we can try continuing solutions from the two neighboring transverse paths across the path with the point of inflection. If a cusp lies in either region between the transverse paths, continuation from one path across to the other will generate a solution different from that originally calculated for the path. This

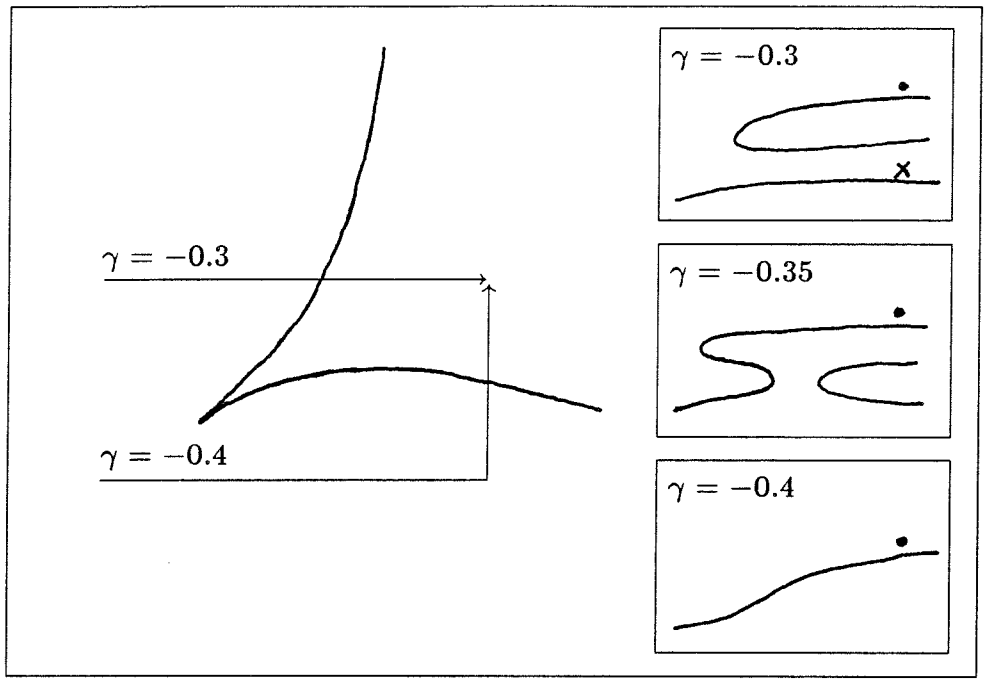

Figure 2.3. Two different solutions are obtained at the same point in the (R, γ)-plane by continuing to that point on different paths. This indicates that a cusp is present between the two paths. The cross-sections of the solution surface sketched at the right show how the solution from the top path ($\times$) is distinct from the solution obtained by taking the bottom path ($\bullet$).

method was used by Szeto [43] to locate the cusps between folds B and C. Szeto had calculated transverse paths for $\gamma = -0.4$ and $\gamma = -0.3$ without encountering any folds. But by continuing from R = 500, $\gamma = -0.4$ to R = 500, $\gamma = -0.3$, he obtained a different solution than he found for this point on the transverse path. Fold C was then found by continuing in decreasing R (see fig. 2.3).

Once a fold is found, we use the techniques of Chapter 1 to trace it out. If there are no cusps along the fold path, then the fold just marks the edge of two subsheets: one "above" the fold and the other "below." We map these out just as if they were disconnected sheets, using the sheet boundaries as the other edges for these subsheets.

If there is a cusp, the picture is a little more involved. We divide the sheet into subsheets by imposing a straight artificial boundary along the line bisecting the

cusp (that is, bisecting its projection onto the (λ,τ)-plane). On this dividing line, the solution path has a pitchfork bifurcation point at the cusp (see fig. 2.4b). Thus, the cusp marks the transition from one solution to three solutions. If we consider a solution path on either side of this dividing line, we see a main solution path (the continuation of the single solution path past the cusp) and another solution path, with a fold, which only exists on the "three solution side" of the cusp. (This phenomenon is called perturbed bifurcation; see Keener and Keller [14].) So, on each side of the dividing line, we will have three subsheets: the subsheet containing the main solution path, and the two above and below the fold (see figs. 2.4a and 2.4c). We treat each of these just as if they were new sheets to map out.

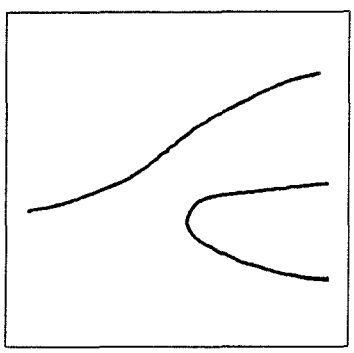

Figure 2.4a. Solution paths on one side of the dividing line of the cusp.

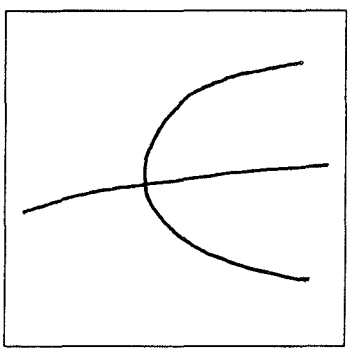

Figure 2.4b. Solution path on the dividing line.

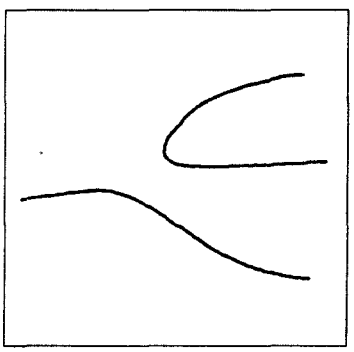

Figure 2.4c. Solution paths on the other side of the dividing line.

If the singularity found on a transverse path is a bifurcation point instead of a fold, then we do not expect it to be stable to perturbations in the problem parameters. Thus, there usually is not a path of singular points to be traced out. So we proceed by using the transverse path as a dividing line between subsheets. If the singular point is a pitchfork bifurcation, then the situation is exactly as above for the cusp; in fact, we have just been lucky enough to have selected a transverse path which bisects a cusp.

If the singular point is a transverse bifurcation point (fig. 2.5b), then the

situation is different on each side of the transverse path. On one side, we have two solution paths, neither of which has a fold (locally, at least). Each of these is a separate subsheet, and the transverse path marks one edge of each subsheet (fig. 2.5a). On the other side, there are also two solution paths, but each has a fold (fig. 2.5c). Thus, there are four subsheets on this side, with the transverse path marking one edge for all of them. One fold marks an edge for one pair of the subsheets, and the other fold an edge for the other pair. As before, we proceed by mapping out each subsheet separately.

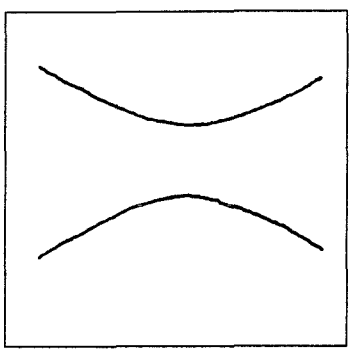

Figure 2.5a. Solution paths on one side of the transverse bifurcation. Each path is the edge of a subsheet.

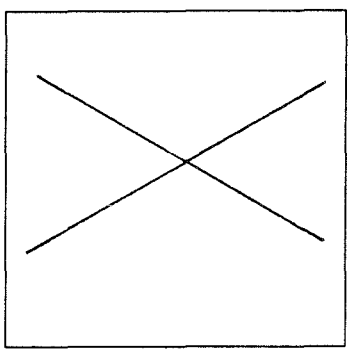

Figure 2.5b. Solution path which contains the transverse bifurcation point.

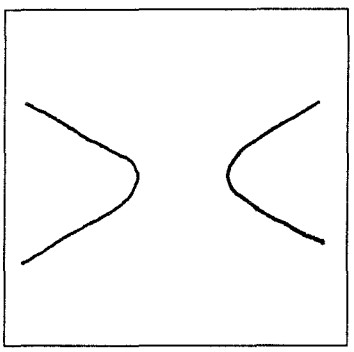

Figure 2.5c. Solution paths on the other side of the transverse bifurcation. Due to the two folds, we see the edges of four subsheets.

This mapping out process is continued until the solution sheet consists only of single-valued subsheets. When this has been accomplished, the sheet has been completely mapped out. We now present the results of this process for each of the sheets found in the solution surface for the flow between rotating, coaxial disks. For sheet one we will describe the process in detail.

2.3.1 Sheet One

The first solution sheet we encounter is that which contains the trivial solutions (2.2.5a) and (2.2.5b). $\gamma = \pm 1$ are natural boundaries for this sheet, as well

as all the others. R = 0 is also a natural boundary for this sheet. To restrict the computations to a finite domain, we chose R = 1000 as the remaining boundary.

Figure 2.6 shows the folds in sheet one. In fig. 2.7 we show sketches of the cross-sections of this sheet. We have not specified an ordinate for these sketches. It is meant to be some norm or projection of the solution, but we have not used any actual mapping since all those that we tried allowed solution branches to cross each other, resulting in much less clear pictures. The abscissa in these sketches is the Reynold's number, R. In order to make the structure of the solution branches clearer, some features have been exaggerated, so the horizontal scale is not linear. Thus, this axis is not labeled either. The value of the Reynold's number at all the folds depicted in the sketches can be obtained from fig. 2.6, however.

Since solutions on the lines R = 0 and $\gamma = 1$ are known, we can use either as the starting line. Following Szeto [43], we have chosen R = 0. We select starting points for the transverse paths at $\gamma = .1i$, $i = -10, \ldots, 10$. For $\gamma = -1$, we encounter a pitchfork bifurcation at R = 119.8 (see fig. 2.7h). This gives rise to the main branch subsheet (which has the same boundaries as sheet one) and the two subsheets forming the top and bottom of fold A (see fig. 2.7g). By continuing a short distance onto the upper branch emanating from the bifurcation point, and then continuing in increasing γ, we locate a point on fold A from which we may start the fold continuation. Fold A runs from the bifurcation point out to R = 1000 with γ monotonically approaching 0. It seems reasonable to conjecture that the fold approaches $\gamma = 0$ asymptotically as $R \to \infty$. We have verified that this is the case as far as R = 3000. Both subsheets making up the top and bottom of fold A are single-valued for $R \leq 1000$.

The next place we encounter some structure in sheet one is between the transversal paths for $\gamma = -.4$ and $\gamma = -.3$ An inflection point is noted in the path for $\gamma = -.4$, and by choosing $\gamma = -.35$ we find the two fold points that "caused"

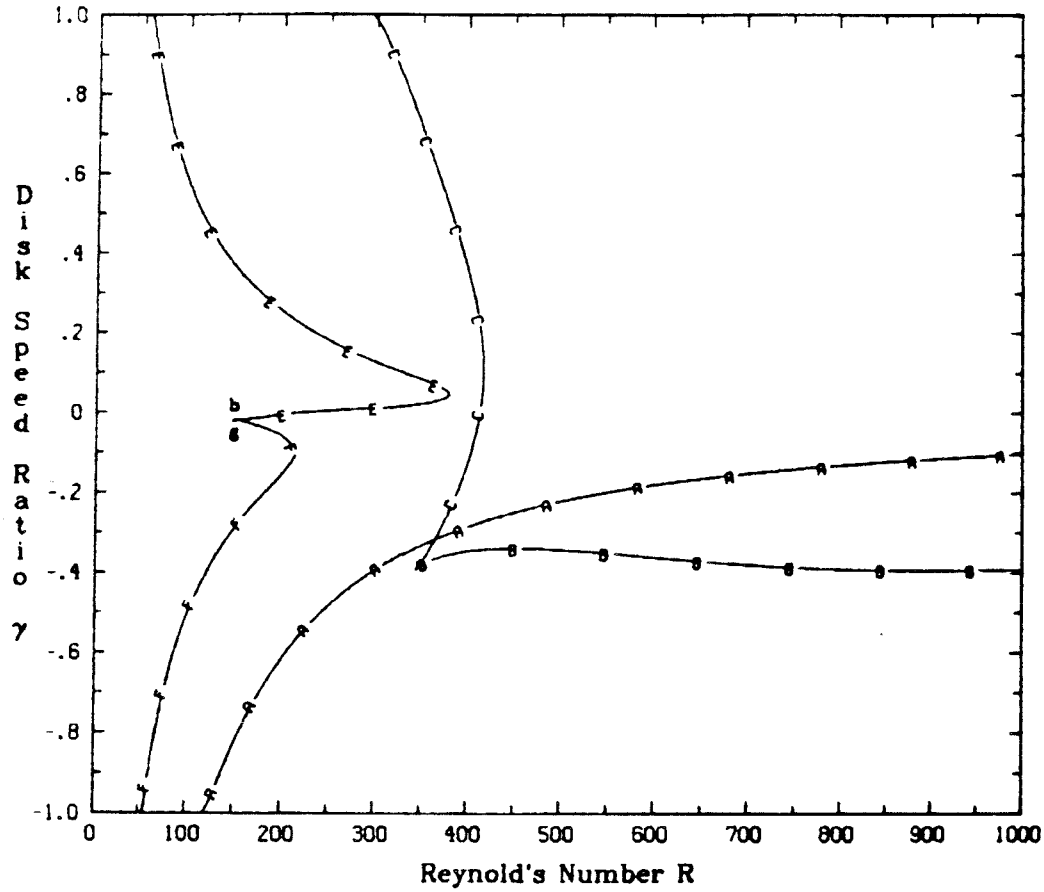

Figure 2.6. A plot of the folds in sheet one.

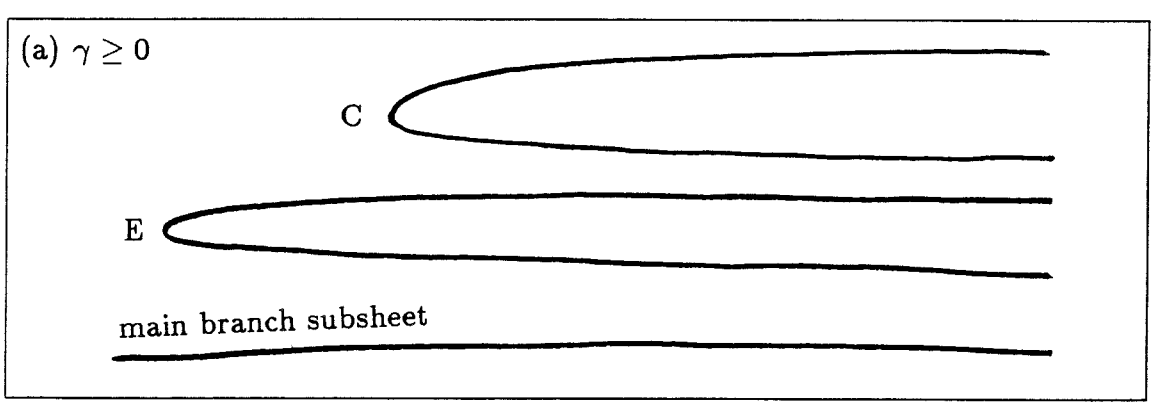

Figure 2.7. A sketch of the cross-sections of sheet one.

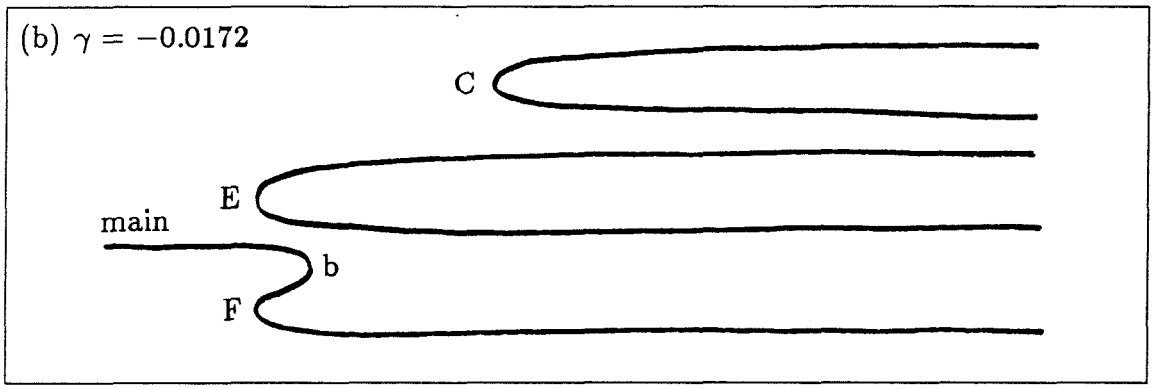

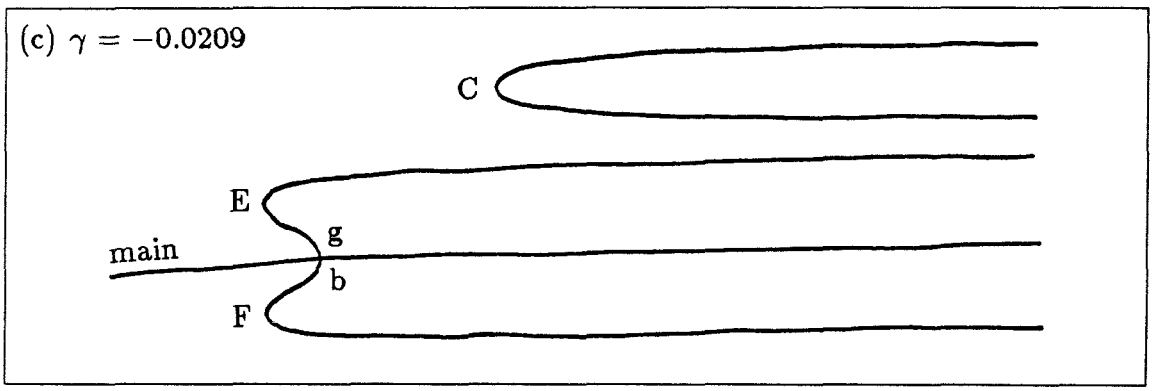

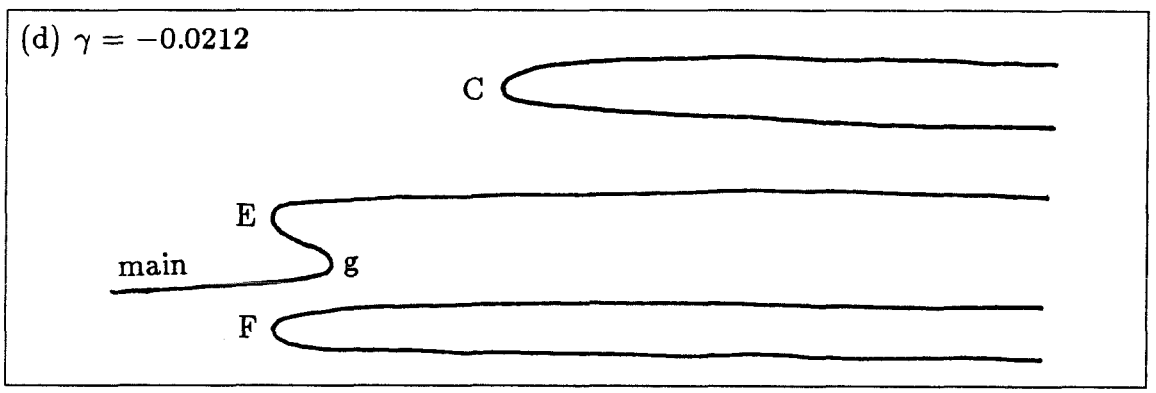

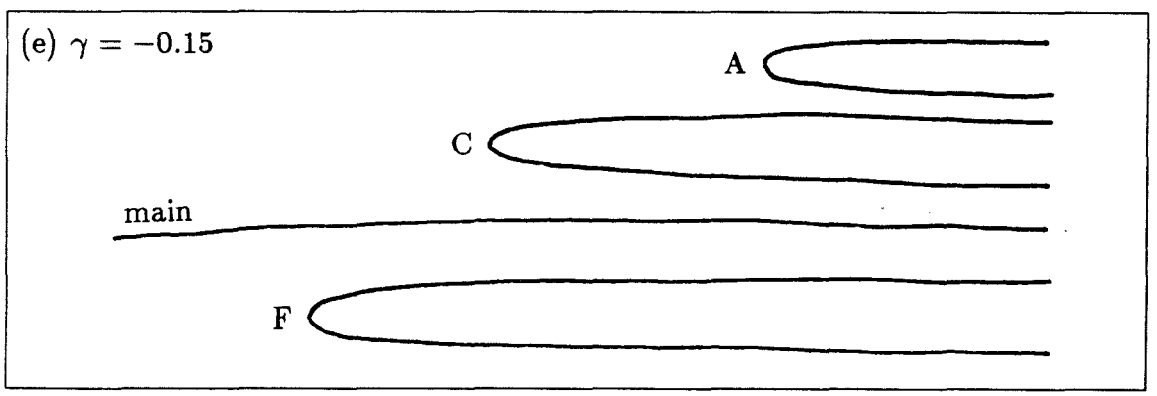

Figure 2.7 (cont.). A sketch of the cross-sections of sheet one.

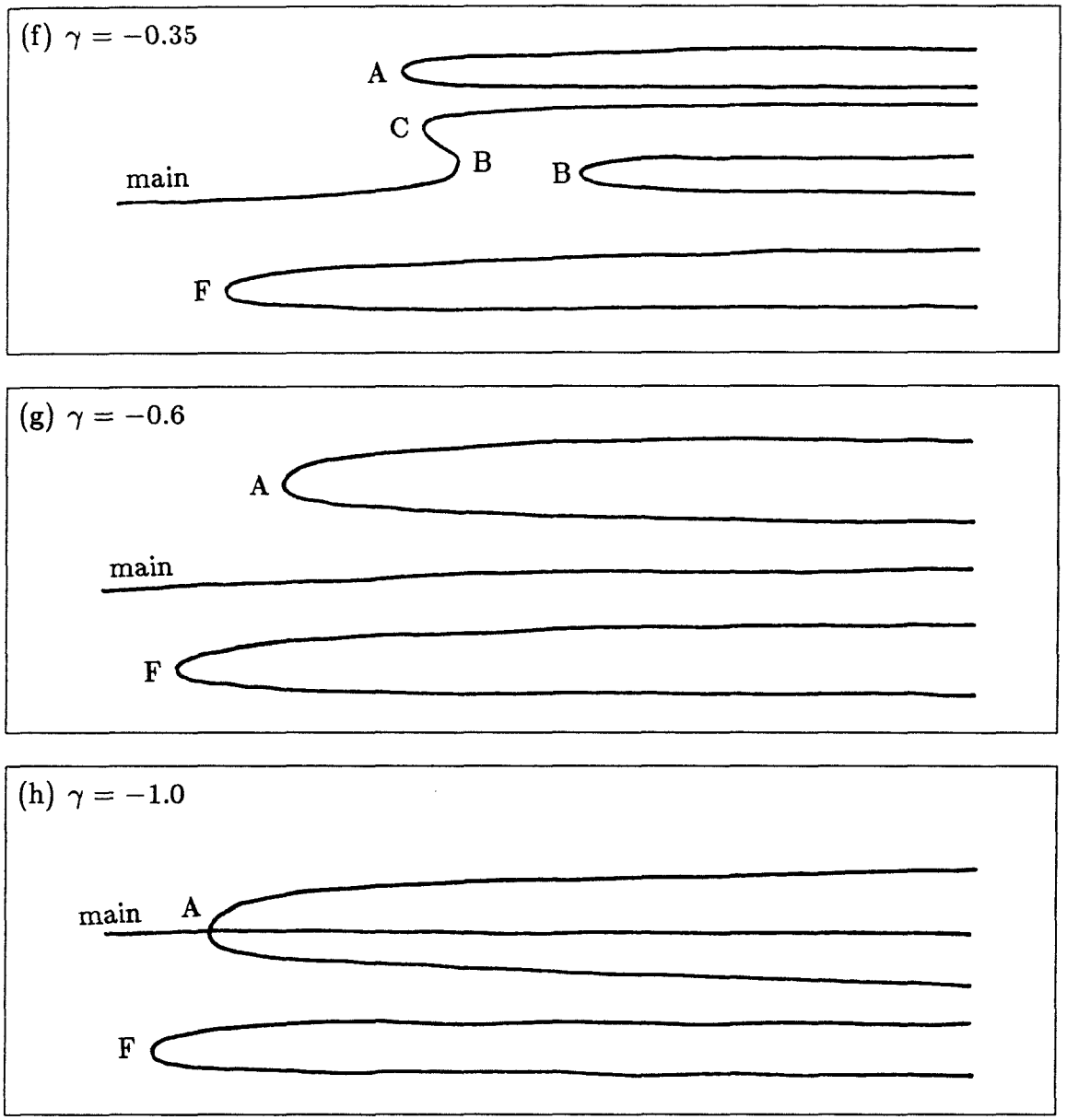

Figure 2.7 (cont.). A sketch of the cross-sections of sheet one.

it (see fig. 2.7f). From these two points we trace out folds B and C, which meet at a cusp. Following the above discussion we partition the main branch (sub) sheet into three subsheets on each side of the dividing line bisecting this cusp. One subsheet on either side of the dividing line is just half of the main branch (sub) sheet. The remaining subsheets make up the tops and bottoms of folds B and C. Each of these four subsheets, as well as the half of the main branch (sub) sheet on

the "fold B side" of the dividing line, is single-valued.

We now have just the "fold C side" half of the main branch (sub) sheet to map out. The only place we have a hint of structure is between $\gamma = -.1$ and $\gamma = 0$. Putting in extra transverse paths does not do much good, but by continuing the solution on the $\gamma = 0$ transverse path at R = 300 to $\gamma = -.1$, and then continuing in decreasing R, we encounter fold F (see figs. 2.7a–e, noting that fold F never passes above R $\approx$ 220). Using fold continuation, we are able to trace out folds F and E and locate folds b and g. We say "locate" here because these two folds are so small and so close to each other and folds E and F that fold continuation becomes nearly impossible in this small region. Pseudo-arclength continuation in both the R- and γ-directions can be used to clear up the picture, however, and we are able to resume fold continuation once we are a little bit away from folds b and g.

Since folds b and g are so small, it is impossible to see in fig. 2.1 what is going on where they meet folds E and F. The structure here is what is called in catastrophe theory a *butterfly* [47]. A much bigger example of this phenomenon occurs for folds I, J, K and L on sheet three (for the butterfly at hand, fold E corresponds to fold I, g to J, b to K and F to L). Since this butterfly in sheet one is so small, the net effect it has away from its immediate vicinity is that of a cusp. A dividing line through the center of the butterfly divides the current subsheet into two halves, and on either side of the dividing line, two more subsheets, representing the upper and lower subsheets of folds E and F, are generated.

In the neighborhood of the butterfly, the picture is more complicated. (As a first resort, consult the pictures, not the words.) We begin dissecting the local geometry by drawing a dividing line which bisects the cusp where folds b and g meet (fig. 2.7c is a sketch of the solution branches in the cross-section taken along this dividing line). On one side of this line (fig. 2.7b) is a tiny subsheet with edges at folds F and b. In the discussion of cusps above, we would have called

this the "bottom of fold b" subsheet. Matters are complicated by the fact that this subsheet almost immediately folds over, which divides the "bottom of fold b" subsheet into two subsheets: one is really just the bottom of fold b; the other is the bottom of fold F, which was mentioned above when we considered the net effect of the butterfly. Back to the three subsheets on this side of the dividing line: The top of fold b is the part of the curve heading toward $R = 0$. This is part of what we have been calling the main branch (sub) sheet. The third subsheet generated on this side of the cusp is the bottom of fold E, which we have already mentioned above. A similar story holds for the other side of the dividing line (fig. 2.7d) with the tiny subsheet now having edges on folds E and g. For a good picture of a butterfly, see [47], p. 338.

All of the subsheets in the last two paragraphs are single-valued, so we have completed mapping out sheet one. In order to find more solutions, we must locate new sheets. To do this we make use of Lemma 2.2.4. In the discussion to follow, we will be speaking about solution branches. Here, by *solution branch* we shall mean a connected set of solutions, for a given cross-section of a solution sheet, the endpoints of which are marked by the boundaries of the sheet or by singular points. Thus, fig. 2.7h shows six solution branches.

Recalling the mapping defined in Lemma 2.2.4, we see that it is one-to-one, onto and smooth. Thus, when applied to the solution branches of sheet one at $\gamma = \pm 1$, the resulting solution branches have the same structure as they did in sheet one. That is, folds map to folds, bifurcation points to bifurcation points, and the solution branches connect to each other just as they do in figs. 2.7a and 2.7h. Therefore, we only need to apply Lemma 2.2.4 at one point on each solution branch, and we can minimize the amount of work we need to do by mapping the solution points that have the most branches in common, i.e., singular points.

As an example, for $\gamma = 1$, depicted in fig. 2.7a, we need to map three points:

the two folds and any point on the main solution branch. In this case the main solution branch is symmetric, so the transformation in Lemma 2.2.4 will only give us back these same solutions. The folds, however, are antisymmetric and from them we obtain new solutions: Fold C maps to fold h on sheet two, and fold E maps to fold G on sheet three. For $\gamma = -1$, which is shown in fig. 2.7h, we need only do two mappings: one at the bifurcation point and one at the fold. In this case, the bifurcation point is symmetric. But the fold is not, and the mapping gives us a new fold. In fact, this turns out to be fold G, which we probably could have surmised since we can continue along fold F, through folds b and g, and end up on fold E, which is mapped to fold G.

With no more solutions to which we need to apply Lemma 2.2.4, we are ready to move onto sheet two.

2.3.2 Sheet Two

Figure 2.8 shows the folds in solution sheet two. The cross-sections of this sheet are sketched in fig. 2.9.

As mentioned above, we obtain a starting solution for sheet two by applying Lemma 2.2.4 to Fold C at $\gamma = 1$. The new solution obtained is on fold h, which is barely visible in fig. 2.8. Using fold continuation, we trace out fold h to the cusp where it meets fold D. Continuing through this cusp we trace out fold D to R = 1000.

The presence of the cusp indicates that there are at least three solutions on this sheet for any values of R and γ lying to the right of fold h and above fold D (i.e., on the three solution side of the cusp). At any given point two of these will just be the top and bottom of one of these folds. The third solution is what we have called the main branch of the cusp. In addition to being the third solution branch on this side of the cusp, it is also the only solution branch on the other

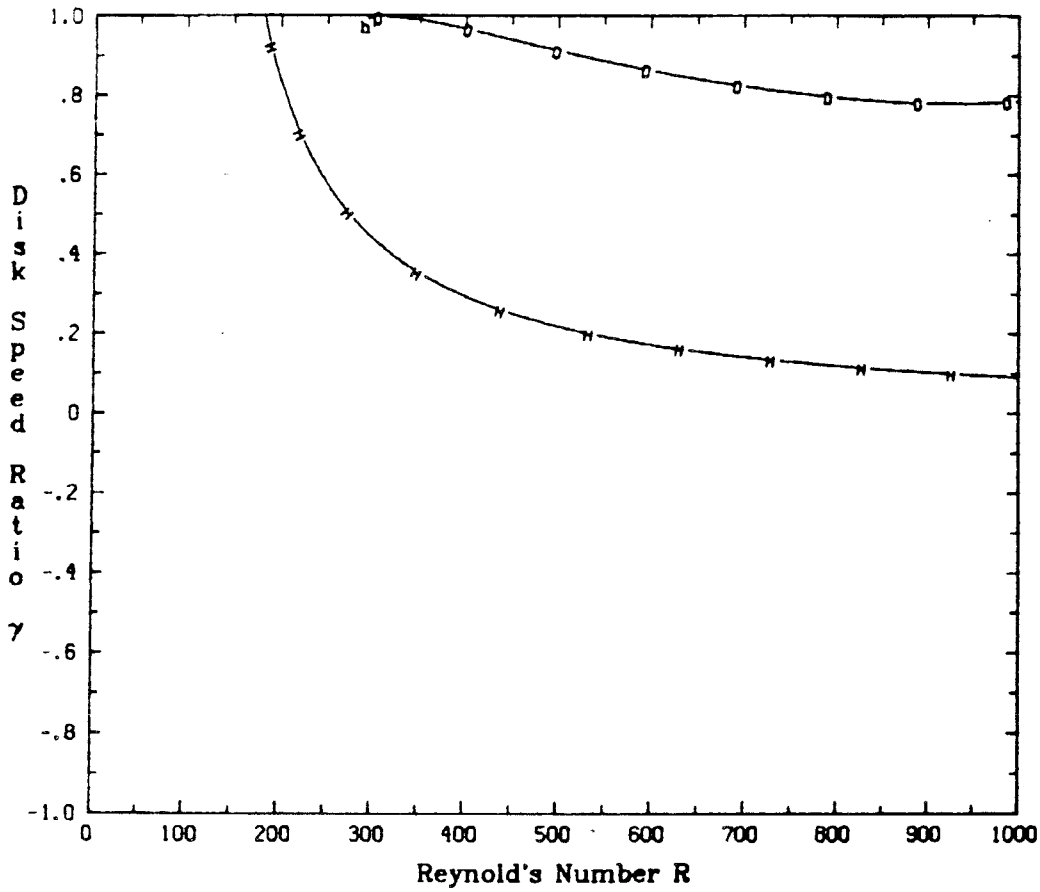

Figure 2.8. A plot of the folds in sheet two.

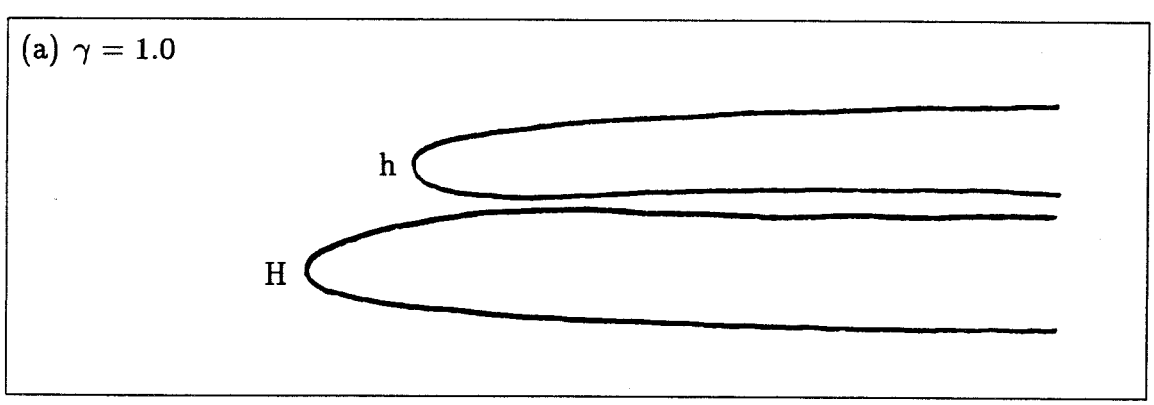

Figure 2.9. A sketch of the cross-sections of sheet two.

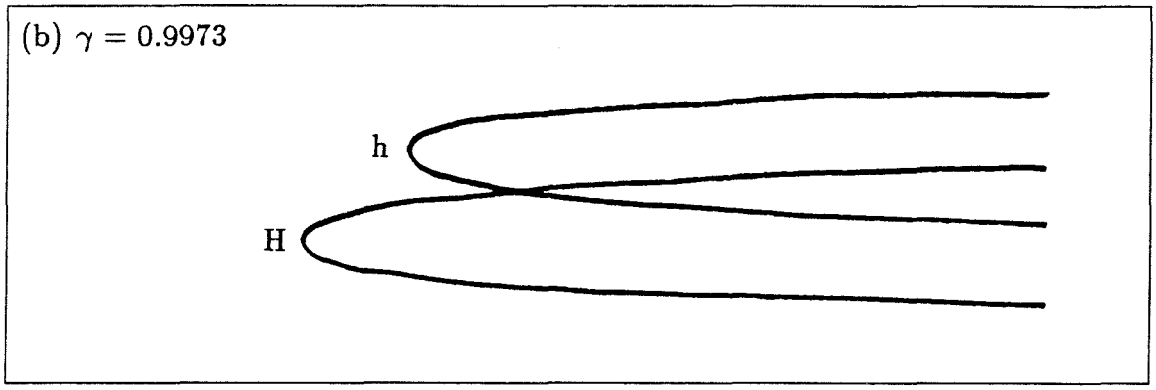

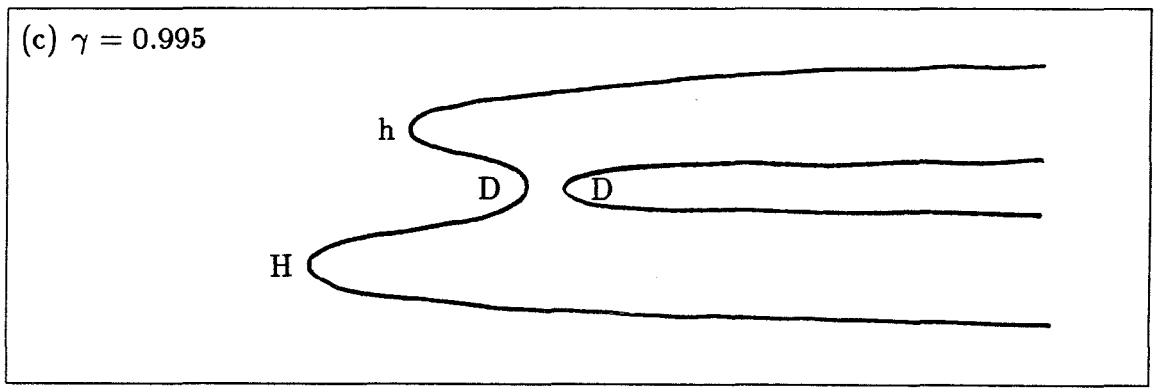

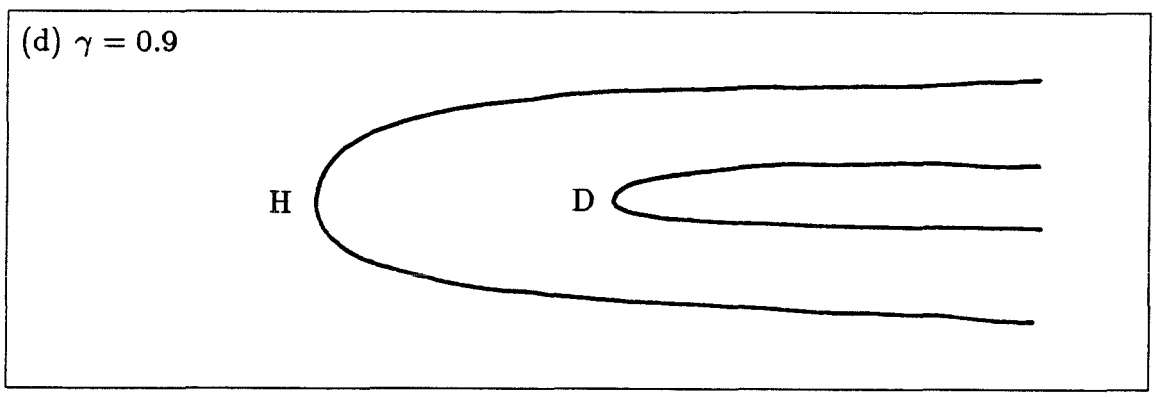

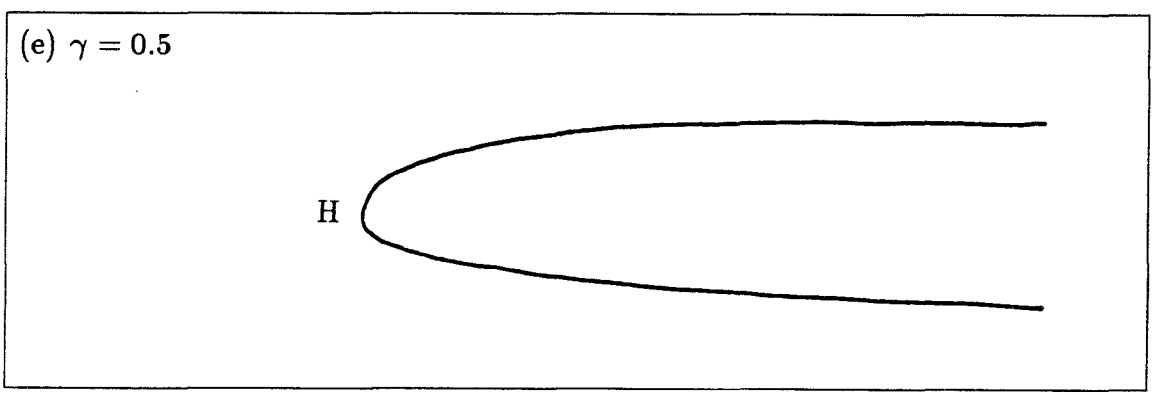

Figure 2.9 (cont.). A sketch of the cross-sections of sheet two.

side. Continuing it on the one solution side, we find fold H. This fold is a natural boundary for sheet two. Its presence indicates that another subsheet of solutions, that on the bottom of fold H, exists. This bottom subsheet turns out to be flat, so sheet two simply consists of the flat lower subsheet and the upper subsheet, which is comprised of the cusp and its requisite subsheets.

Since the structure of this sheet is very simple, the only features of particular note, other than the cusp where folds h and D meet, are the hyperbolic point near $R \approx 300$ and the isola near $R \approx 950$, both on fold D (and both with respect to R). As can be seen in fig. 2.9b, the hyperbolic point is just a transverse bifurcation for γ held fixed. Changing γ by a small positive amount perturbs the hyperbolic point into two branches (the bottom of fold h and the top of fold H) with no (local) folds (fig. 2.9a). Perturbing in the other direction breaks the hyperbolic point into four branches (fig. 2.9c). The isola just indicates that the fold is bending back towards $\gamma = 1$. Thus, it is unclear whether this fold eventually asymptotes to $\gamma = 0$ as fold H appears to do.

2.3.3 Sheet Three

Sheet three is the most complex of the solution sheets. Its folds are plotted in figure 2.10. The cross-sections of this sheet are sketched in fig. 2.11.

A starting solution for this sheet is obtained by using Lemma 2.2.4 either on fold E at $\gamma = 1$ or on fold F at $\gamma = -1$. Using fold continuation, both choices result in the tracing out of fold G. This fold, given by, say, $R = R_G(\gamma)$, is a natural boundary for the two subsheets above and below it. In fact, it is a natural boundary for the entire sheet, as no other solutions exits for values of R to the left of this fold. This is also true of all other sheets and subsheets except sheet one, which leads one to conjecture that the problem has a unique solution for $R < R_G(\gamma) \approx 57$. Note that this fold is not a straight line as it appears to be

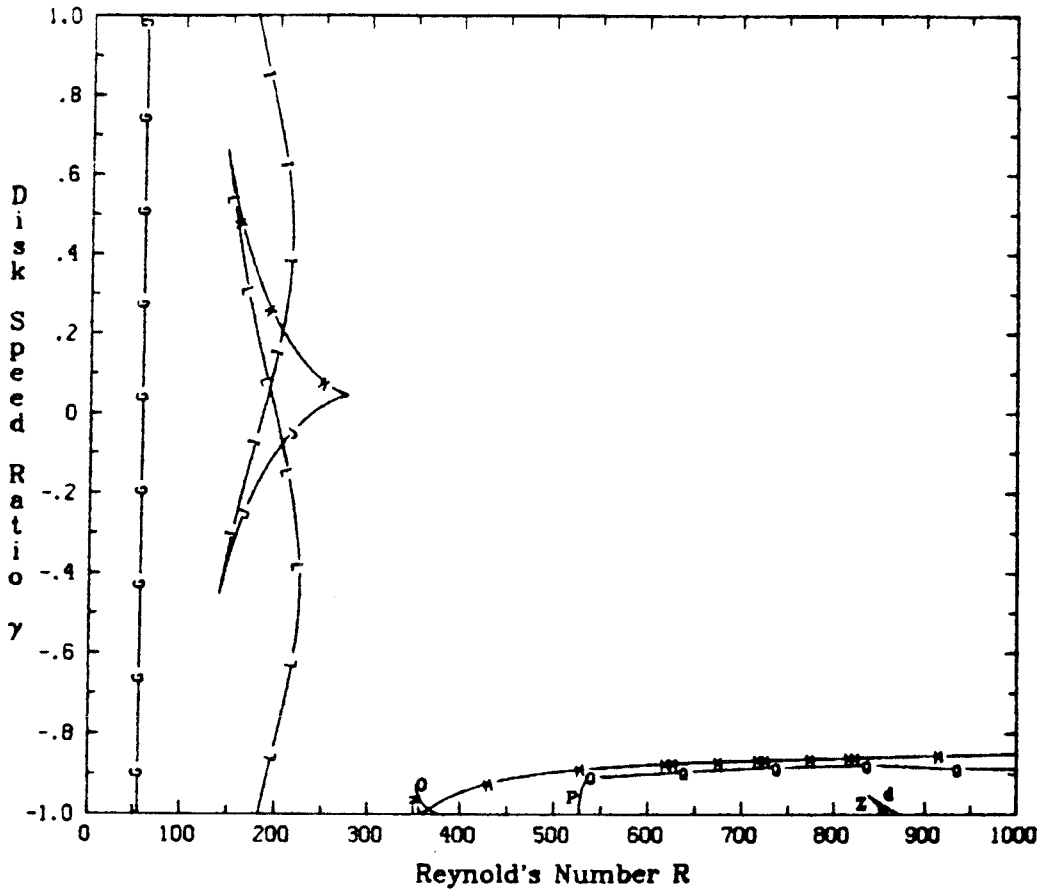

Figure 2.10. A plot of the folds in sheet three.

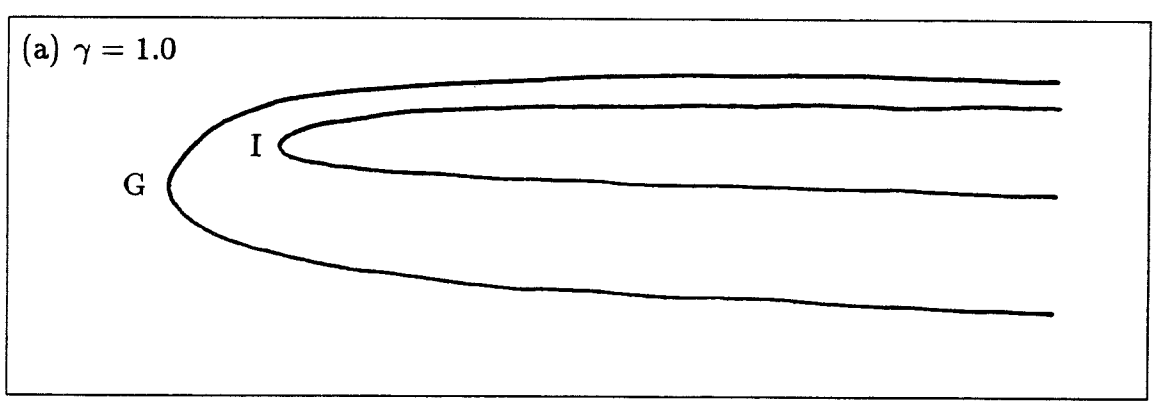

Figure 2.11. A sketch of the cross-sections of sheet three.

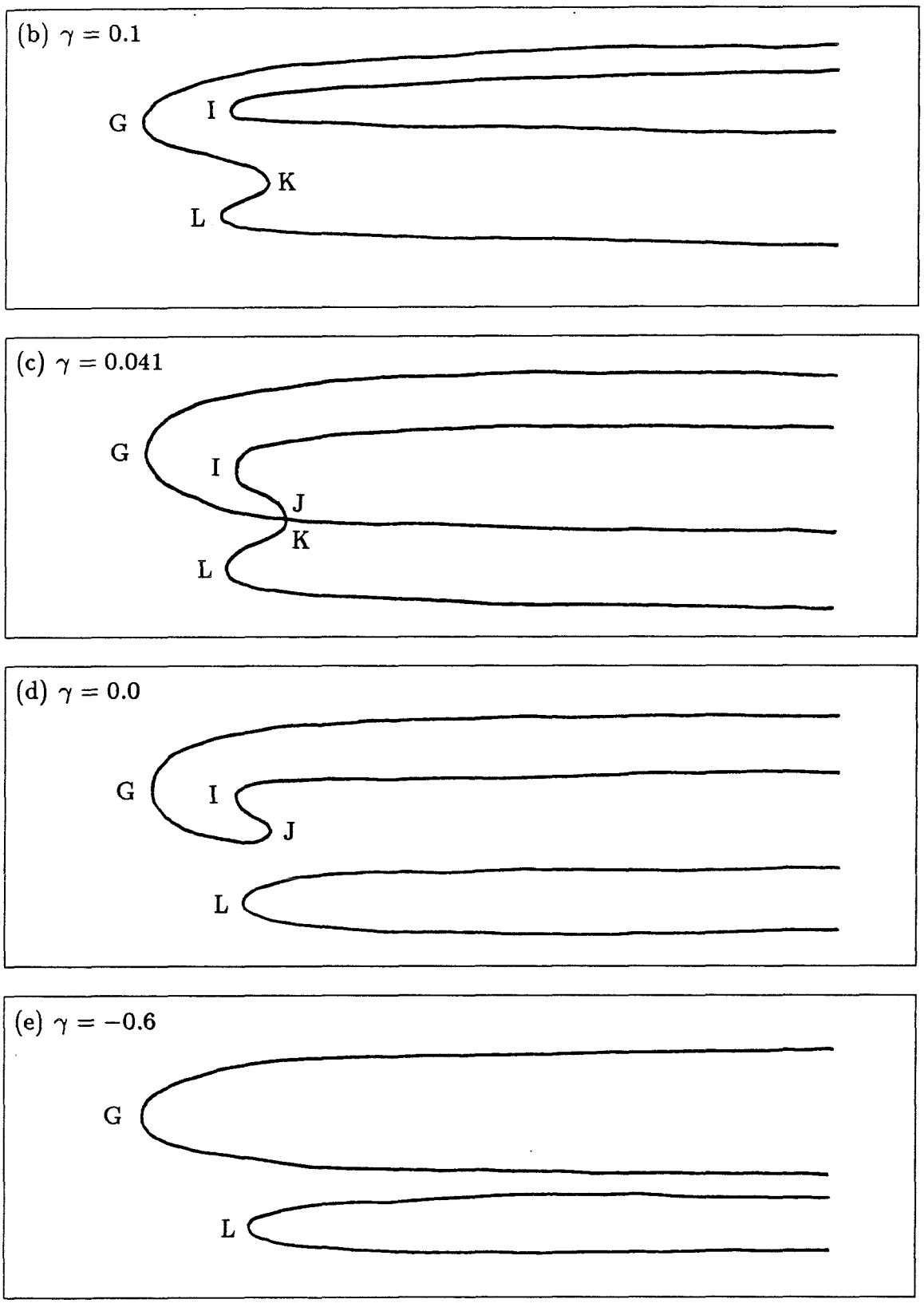

Figure 2.11 (cont.). A sketch of the cross-sections of sheet three.

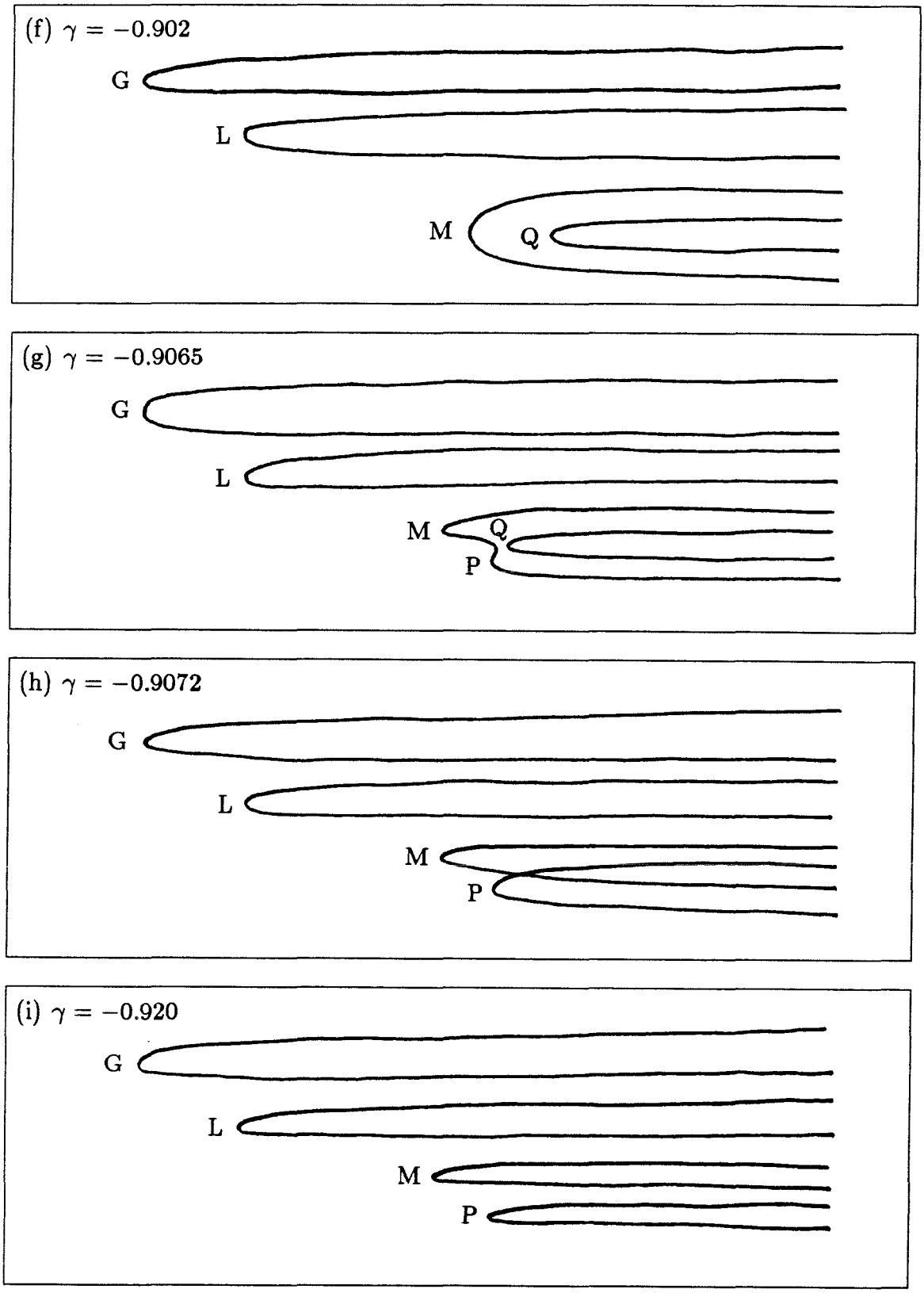

Figure 2.11 (cont.). A sketch of the cross-sections of sheet three.

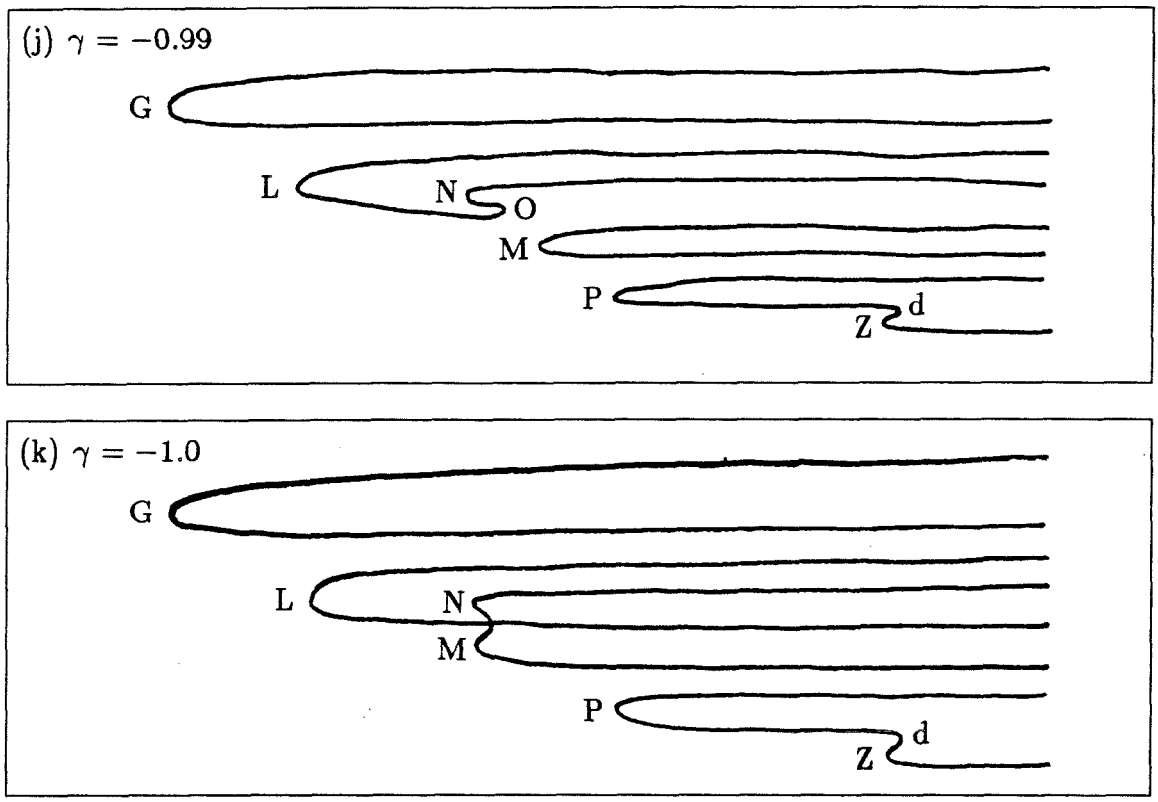

Figure 2.11 (cont.). A sketch of the cross-sections of sheet three.

in figs. 2.1 and 2.10. $R'_G(\gamma) = 0$ for $\gamma \approx .86$, and each point on the fold is a hyperbolic point (with respect to some slice nearly parallel to the γ-axis).

Mapping out the subsheet above fold G, we find that it is single-valued. This is not the case, however, for the bottom of fold G. The butterfly consisting of folds I, J, K and L is a part of this subsheet. One can trace the development of the butterfly in figs. 2.11a–e. Figure 2.11a shows the cross-section for γ values above the cusp where folds K and L meet. The picture below the cusp, where both folds exist, is shown in fig. 2.11b. The cross-sectional slice along the dividing line of the butterfly, or more precisely, of the cusp of folds J and K, is shown in fig. 2.11c. Here, we can clearly see the pitchfork bifurcation. The situation on the other side of this cusp is drawn in fig. 2.11d. Finally, fig. 2.11e depicts the solution branches for values of γ below the cusp of folds I and J.

The rest of the subsheet on the bottom of fold G is flat except in a small region close to $\gamma = -1$. Tracing out the transverse path at $\gamma = -1$ on the bottom of fold L, we find a pitchfork bifurcation point at R = 380.5. It turns out that this point is the center cusp of another butterfly. Only half of the butterfly appears in $\gamma \geq -1$, however. The folds making up this butterfly in this region are folds M, N and O (see figs. 2.11j-k).

Since the butterfly is not very big, its existence is only felt in the rest of the sheet by the presence of the subsheets on the top and bottom of fold M. The top of fold M is flat. But the bottom behaves just like the top of fold H in sheet two. There are up to three solutions on this subsheet, all joining at the cusp of folds P and Q. Just as was the case for fold D, there is a hyperbolic point (with respect to R) near the cusp. In addition, for larger values of R, there is an isola and another hyperbolic point.

The last folds we find in the sheet occur on the bottom of fold P. For $\gamma = -1$ we find folds d and Z at R = 871 and 859, respectively. As γ is increased, these approach each other and coalesce.

This completes the description of sheet three. All that remains now is to use Lemma 2.2.4 to see if any more sheets can be found. Applying this to fold G just gets us back to sheet one. Fold I is symmetric at $\gamma = 1$, and fold L is symmetric at $\gamma = -1$. Similarly, the bifurcation point at R = 380.5 is symmetric. Folds M and N are antisymmetric. However, they are images of each other under the transformation in Lemma 2.2.4. It is of interest to note that this was the only place we found where an antisymmetric solution transformed to another solution on the same sheet. The remaining folds on this sheet are antisymmetric, and we find that fold P maps to fold R, fold d maps to fold S, and fold Z maps to fold T, all on sheet four.

2.3.4 Sheet Four

Sheet four is another relatively simple sheet. Its folds are plotted in fig. 2.12. The cross-sections of this sheet are sketched in fig. 2.13.

Tracing out the transverse path on the top of fold R at $\gamma = -1$, we find that the three new folds obtained are indeed on the same sheet. Figure 2.13e shows their locations. Unlike folds d and Z from which they were obtained, folds S and T do not approach each other but instead diverge.

Continuing fold R we find that it extends all the way across to $\gamma = 1$, having taken a circuitous route which reaches out as far as R = 1003. Away from $\gamma = -1$, the top subsheet is flat. But for $\gamma \geq .4$ we find a fold (W) in the bottom subsheet. The bottom of fold W then extends all the way down to R $\approx$ 350, where we find fold X. This can be continued back across the domain Ω to $\gamma = -1$. Its bottom subsheet is single-valued.

These are all the folds in sheet four. Applying Lemma 2.2.4 at $\gamma = 1$, fold R transforms to fold U, fold W to fold k, and fold X maps to fold V, all on sheet five. At $\gamma = -1$, fold X maps to fold Y on sheet six, and the rest have been dealt with before.

2.3.5 Sheets Five and Six

We conclude with sheets five and six, the two simplest sheets. Since they are both obtained by applying Lemma 2.2.4 to fold X, perhaps there is reason to consider this as just one sheet. But since they are not actually connected for R and γ in the domain Ω, we keep with our convention and classify them as different sheets. The folds in these sheets are shown in fig. 2.14. Sheet five has $\gamma > 0$. The cross-sections of these sheets are shown in figs. 2.15 and 2.16.

Sheet six merely consists of two flat subsheets: the top and bottom of fold Y. Sheet five is almost as simple, but the top of fold V has a cusp in it, which generates

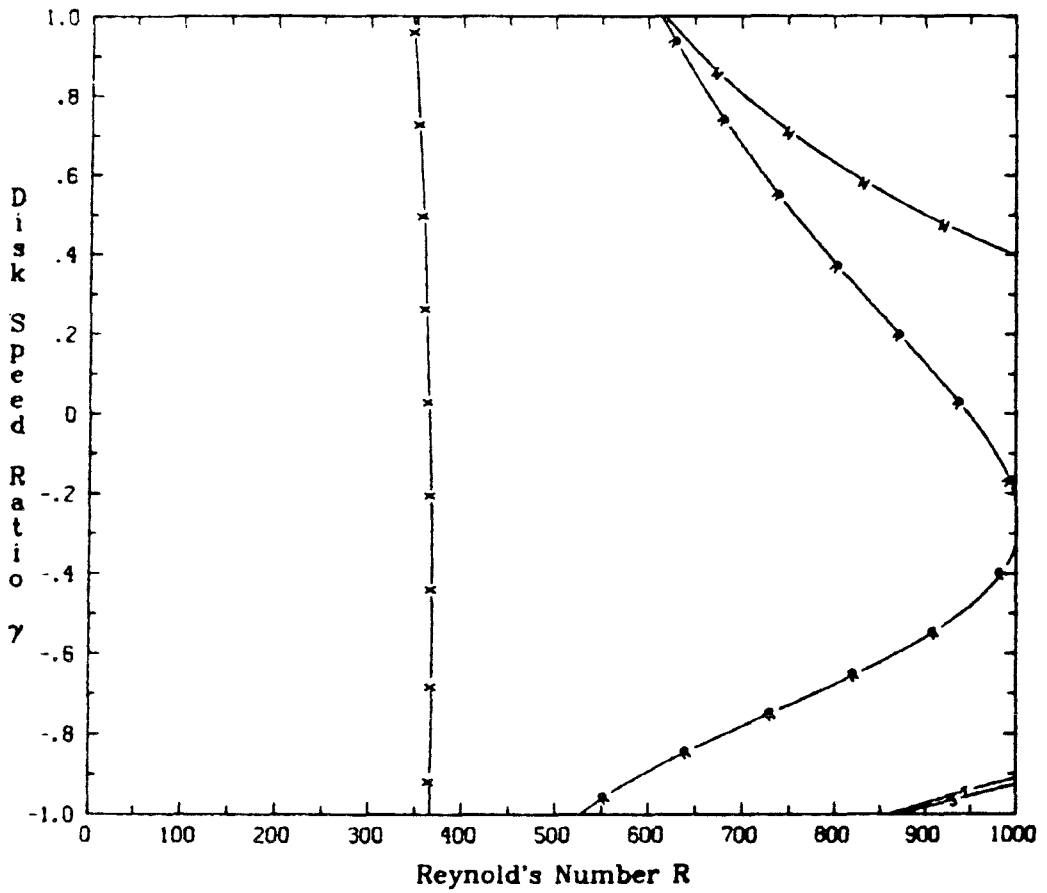

Figure 2.12. A plot of the folds in sheet four.

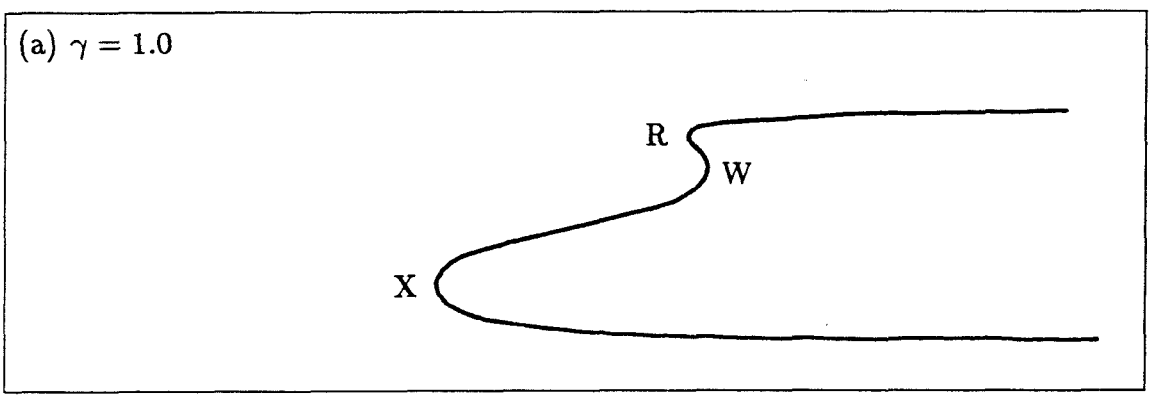

Figure 2.13. A sketch of the cross-sections of sheet four.

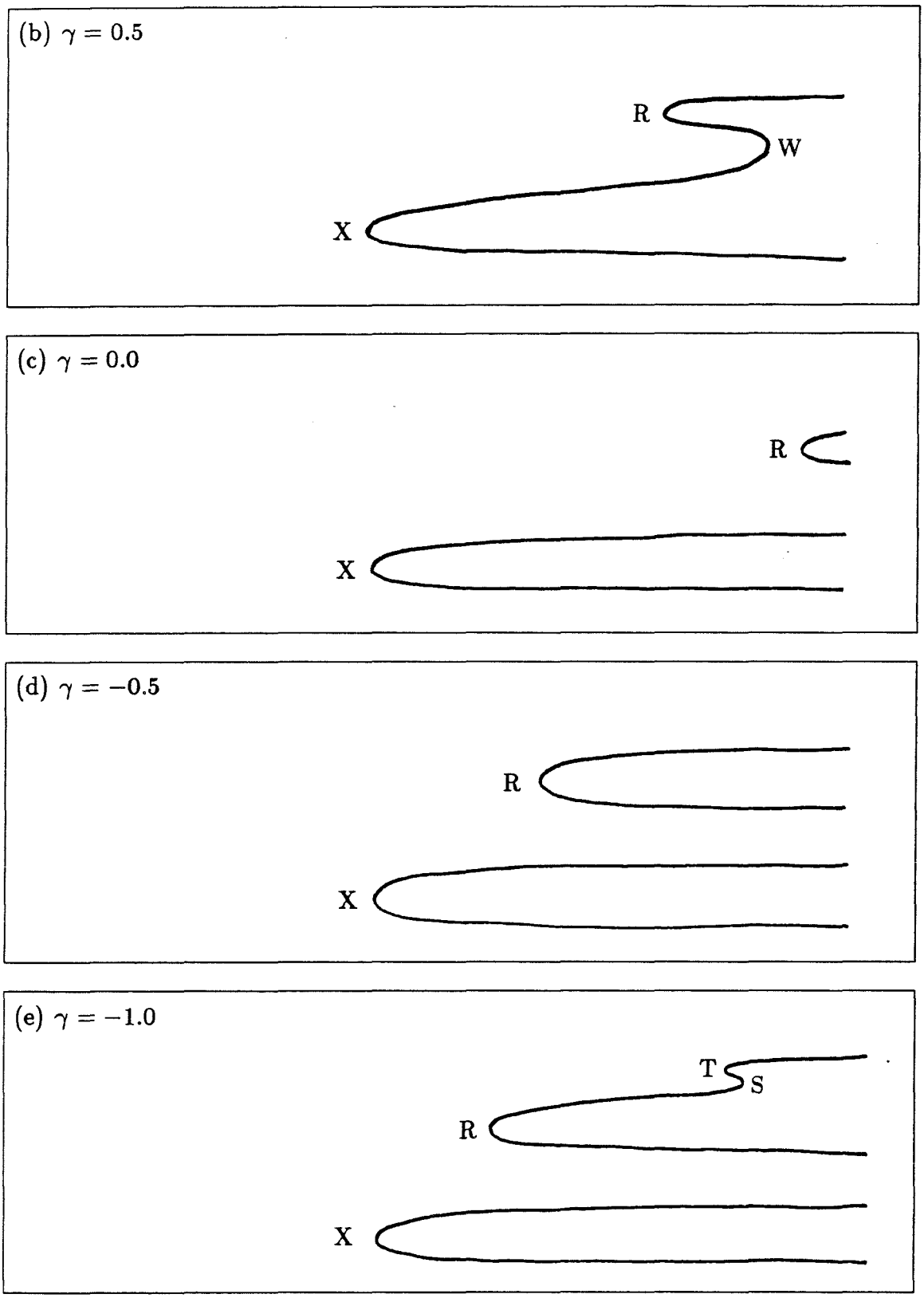

Figure 2.13 (cont.). A sketch of the cross-sections of sheet four.

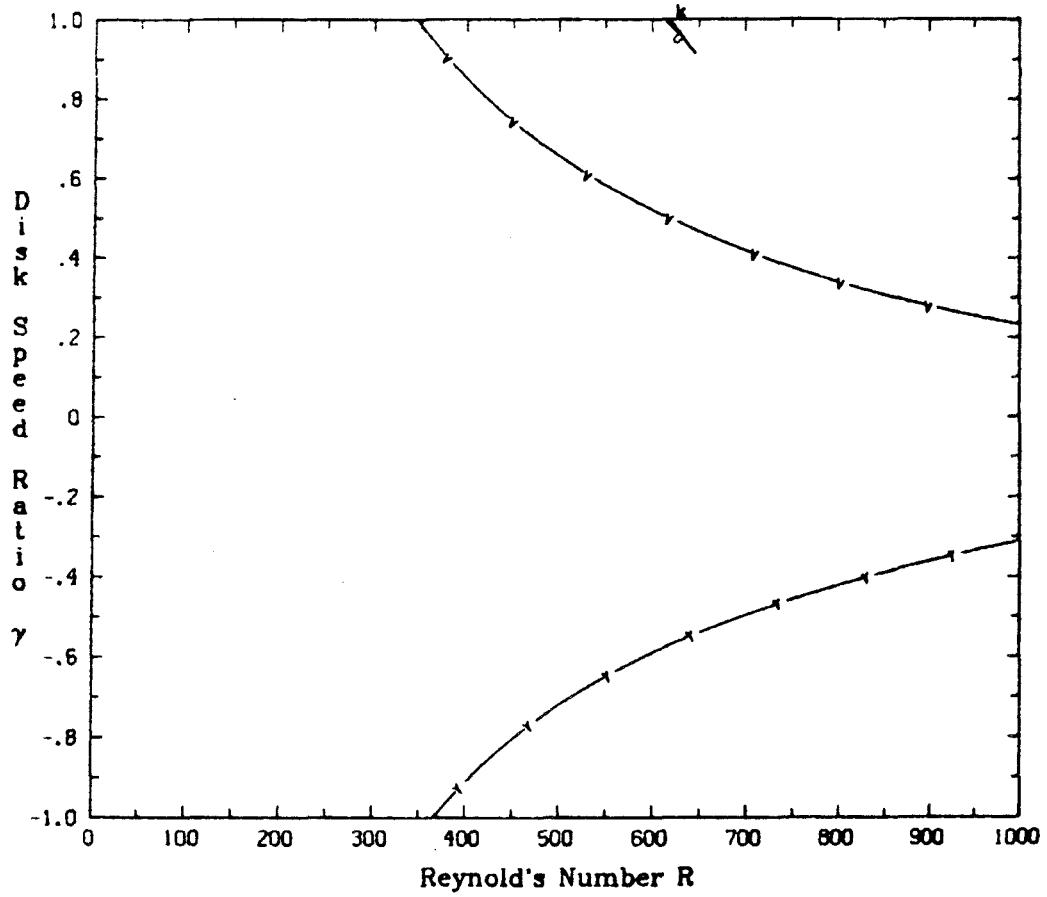

Figure 2.14. A plot of the folds in sheets five and six.

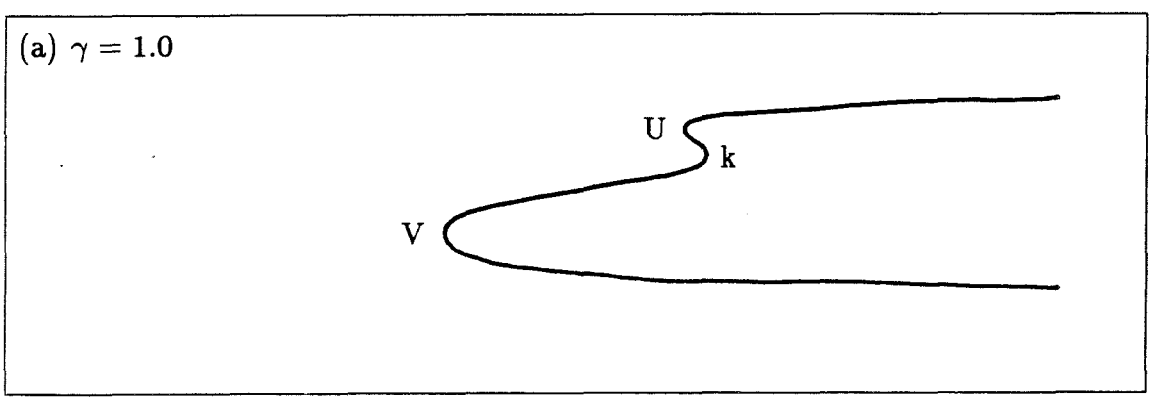

Figure 2.15. A sketch of the cross-sections of sheet five.

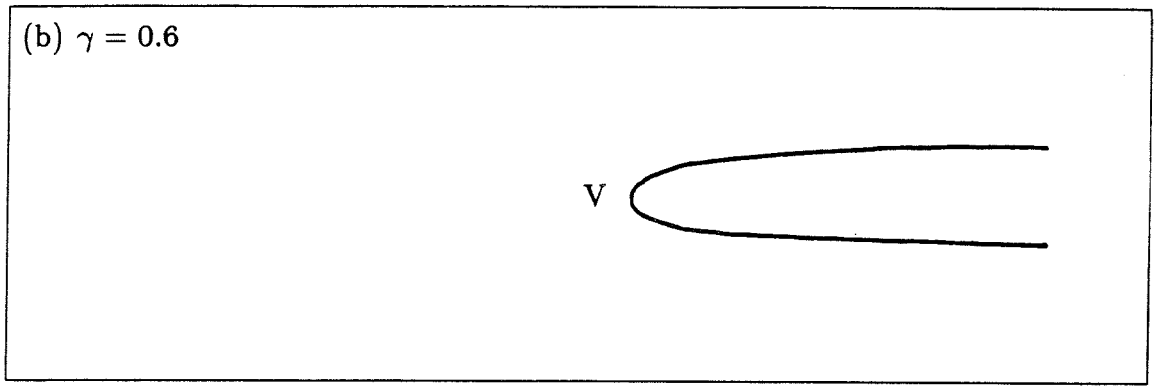

Figure 2.15 (cont.). A sketch of the cross-sections of sheet five.

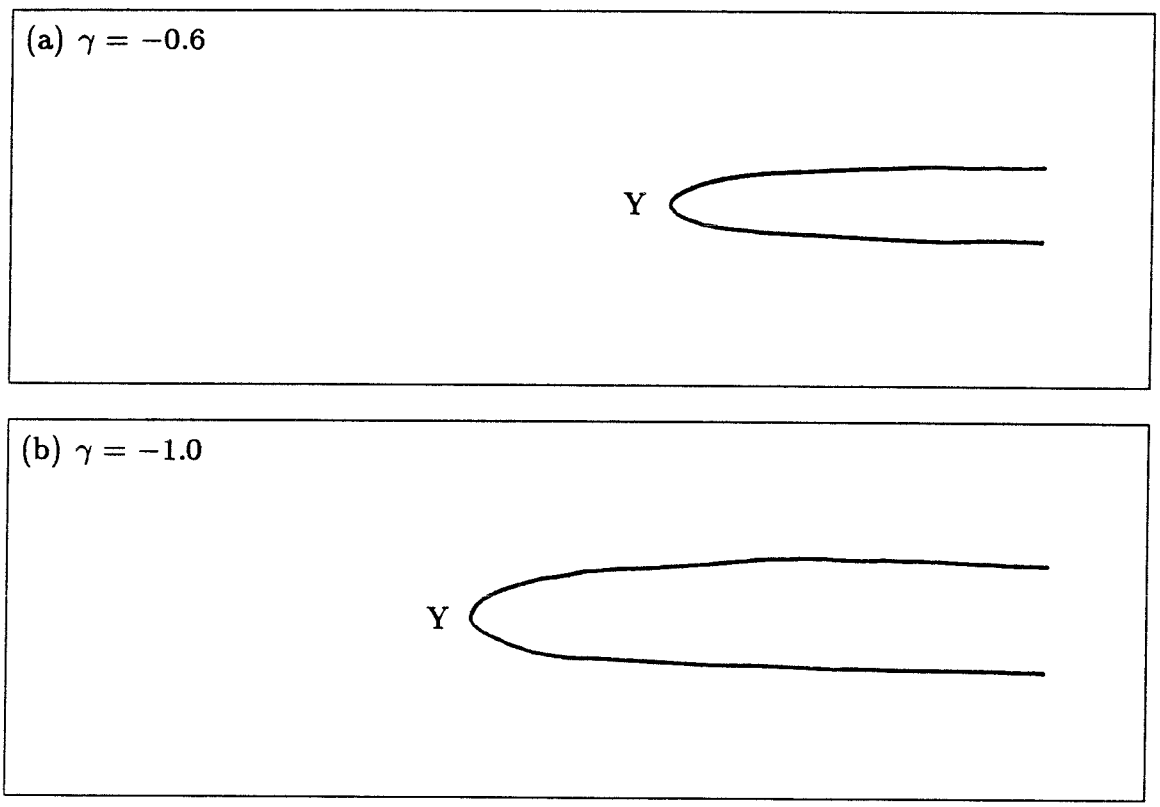

Figure 2.16. A sketch of the cross-sections of sheet six.

two more solutions for $613 < R < 619$ and γ near 1.

All of the folds on these two sheets were found by applying Lemma 2.2.4 to folds on other sheets. Thus, we can generate no more solution sheets by this technique and so we are finished mapping out the solution surface in $R \leq 1000$, $|\gamma| \leq 1$.

2.4 Previous Investigations

As was made evident in Section 2.1, there has been a great deal of work done on this problem. Most of the work, however, has merely involved calculating solutions at a few isolated R and γ values. We would now like to show how this previous work fits into the picture of the solution surface which we described in Section 2.3. So that the results here may be compared with the work of other authors, we have collected together the velocity profiles for all the solutions at R = 625 and γ = 1, 0 and -1, and these have been presented in the Appendix.

The first studies of this problem were made by by Batchelor and Stewartson. Both agreed that for $\gamma \geq 0$ the angular velocity of the main body of the fluid should rotate with a speed between those of the two disks. Such solutions are located on the main branch of sheet one in fig. 2.7a, and velocity profiles are shown in figs. A1.5 ($\gamma = 1$) and A1.10 ($\gamma = 0$). In the literature this has become known as the "Batchelor branch." For $\gamma < 0$ Batchelor predicted a solution in which the main body of the fluid would be divided into two regions of nearly constant angular velocity, separated from the disks and each other by three boundary layers. Stewartson disagreed, saying that, outside of boundary layers on the disks, the fluid should have no angular velocity. Solutions of this form do indeed exist on sheet one (Stewartson, in fact, obtained them experimentally) and are found on the bottom of fold E in figs. 2.7a–b, which has been called the "Stewartson branch," on the bottom of fold A in figs. 2.7e–g, and on the main branch in fig. 2.7h. The velocity profiles are shown in figs. A1.9 and A1.12. No solutions of the type Batchelor predicted were found.

The majority of the work following Batchelor and Stewartson has been numerical. Lance and Rogers calculated solutions on the main branch (the solution branch extending from R = 0) of sheet one for various values of R and γ. Pearson calculated steady state solutions from the time-dependent equations. He calcu-

lated solutions on the main branch of sheet one for $\gamma = 0$ (see fig. 2.7a) and for values of R up to 1000 (fig. A1.10). For $\gamma = -1$ and R = 1000 he calculated the solution on the main bifurcation branch of fig. 2.7h. Velocity profiles are shown in fig. A1.12. He also calculated solutions for R = 100 for values of γ from -1 to -0.04. These are on the main branch of fig. 2.7g, and, if R had been continued to larger values, they would be on the lower bifurcation branch of fig. 2.7h. See fig. A1.13 for the velocity profiles of these solutions.

Mellor, Chapple and Stokes appear to have been the first investigators to calculate solutions off sheet one. They report two-cell solutions for $\gamma = 0$ and Reynold's number between 58 and 72, which corresponds to solutions on the bottom of fold G in fig. 2.11d, but did not show the solution profiles in [34]. We have plotted the velocities for the continuation of this solution branch out to R = 625 in fig. A1.25. They also calculated solutions on sheet one. In addition to the main branch, they obtained solutions on the top and bottom of fold E (see fig. 2.7a). The velocity profiles of these two solutions are shown in figs. A1.8 and A1.9, respectively. Furthermore, they report calculating a three-cell solution branch. From their sketch of a typical three-cell solution, we may infer that these were on the bottom of fold C in fig. 2.7a (the velocities are plotted in fig. A1.7). Nguyen, *et al.* also calculated solutions on the main branch of sheet one and on the bottom of fold E for $\gamma = 0$, and Wilson and Schryer, integrating the time-dependent equations, obtained solutions for R up to 10,000 for the main branch and the top of fold E.

In their first paper, Holodniok, Kubíček and Hlaváček calculated five solution branches for $\gamma = 0.8$: three on sheet one and two on sheet two (see figs. 2.7a and fig. 2.9a). They calculated for various values of R up to 625, and at this Reynold's number their solutions correspond to the main branch and the top and bottom of fold C on sheet one, and to the top of fold h and bottom of fold H on sheet two

(figs. A1.5, A1.1, A1.2, A1.16 and A1.19, respectively).

In their second paper, Holodniok, *et al.* once again presented results for R = 625, but this time they used continuation in γ and plotted results for the values 1, 0 and -1. For $\gamma = 1$ they calculated 12 of the 17 solutions we have found. These include all five on sheet one (figs. A1.1–5), all four on sheet two (figs. A1.16–19), and three of the four on sheet three (figs. A1.20–21 and A1.23). The bottom of fold I, as well as all solutions on sheets four and five, were not calculated. They calculated 8 of our 11 solutions for $\gamma = 0$. These are the five on sheet one (figs. A1.6–10) and three on sheet three (figs. A1.24–25 and A1.27). The top of fold L in fig. 2.11d was not calculated (see fig. A1.26) as well as the two solutions on sheet four (figs. A1.38–39). Finally, for $\gamma = -1$ they calculated 14 of the 19 solutions we have calculated. These are all five on sheet one (figs. A1.11–15), all but the top of fold L (cf. fig. 2.11k) on sheet three (figs. A1.28–29 and A1.31–35) and two (the top and bottom of fold R in fig. 2.13e) on sheet four (figs. A1.40–41). The two other solutions on sheet four and the two on sheet six were not found.

In observing the solutions obtained by Holodniok, *et al.*, one quickly notices that the number of solutions found for a given value of γ was always even. This fact demonstrates the necessity of calculating the solution sheets of a problem, or at least of being completely aware of them, because an even number of solutions implies that either the solution at R = 0 is not unique, or there exists another solution yet to be found. In either case further investigations would be needed.

The only previous investigator to use the approach of mapping out the solution surface was Szeto, and, in fact, the present work was modeled after his study. Szeto's plot of the folds in the solution surface is much like that presented here in fig. 2.1. But there are some major differences. First, there is no indication of the presence of sheets five and six as he did not find folds k, Q, V, X and Y. The only indication that sheet four exists is the presence of two partial fold paths near

$\gamma = -1$ and R $\approx$ 650, which are the images of each other under the transformation in Lemma 2.2.4. One infers that these are folds P and R, but neither is continued beyond $\gamma \approx -.9$. Also, there is no indication of fold h or the cusp where it meets fold D.

The power one is afforded by the use of fold continuation is made evident by comparing the structure obtained here for the butterfly I,J,K,L to that in Szeto's plot. Using only pseudo-arclength continuation, he did not find the cusp where folds J and K meet, and concluded that there was a single fold running from $\gamma = -1$ along fold L, meeting fold I smoothly and continuing on fold I to $\gamma = 1$. This left folds J and K and the remaining parts of folds I and L (near their cusps) as one big structure, which resembles a pair of lips. Using fold continuation, we have seen that this is actually a butterfly, and that the structure of sheet three is quite different than that depicted by Szeto. In addition, the butterfly in sheet one, which we found by fold continuation, was also missed.

The only real discrepancies between the two plots are the presence of two partial fold paths where folds L and O meet $\gamma = -1$, and an extra half butterfly near fold O which we do not have. Szeto claims that the partial fold path meeting fold L was obtained by applying Lemma 2.2.4 to fold L. But we have found that the solution there is symmetric and so cannot generate another fold. The extra half butterfly is claimed to be on one of the subsheets of this partial fold, and the other partial fold is obtained from the half butterfly. We have not been able to resolve these differences.

This brings us to the asymptotic studies. Fig. A1.12 shows a solution (on the main bifurcation branch of sheet one) which matches exactly the description of the solution whose existence was proved by McLeod and Parter and the solution found asymptotically by Matkowsky and Siegmann. This solution is also typical of the solutions described by Kreiss and Parter in their first paper [25]: namely,

the axial velocity decays at least as fast as $R^{-1/2}$ and the angular velocity tends to a constant away from layers at the disks. There are numerous other examples of this type of solution, for example, figs. A1.2, A1.8, A1.9, A1.10, A1.19.

In [27] Kreiss and Parter describe solutions to equations (2.2.2) which Szeto has called "large amplitude solutions." They do this by rescaling the variables so that the solutions are bounded but the disk speeds tend to zero as $R \to \infty$. They found that for sufficiently large R, the axial and angular velocities would consist of any number of cosine shaped humps. Moreover, in the limit of infinite Reynold's number, the axial velocity would be of only one sign, and the humps in the angular velocity would alternate sign. Several examples of these types of solutions are shown in appendix A1: one hump solutions are shown in figs. A1.4, A1.14, A2.20, A1.24, A1.26 and A1.28; two hump solutions are found in figs. A1.36–39 and A1.42–46.

There are some solutions, however, which could be contrary to Kreiss and Parter's results. The two hump solutions in figs. A1.22, A1.30 and A1.32 do not have axial velocities of only one sign. The same is true of the three hump solutions in figs. A1.34, A1.35, A1.40 and A1.41. This could, of course, be a result of the fact that these solutions are shown for a finite Reynold's number, one which may not be sufficiently large for the results of Kreiss and Parter to apply. On the other hand, these solutions could be the result of insufficient numerical resolution in the neighborhood of the zeroes of the axial velocity. The results of Kreiss and Parter indicate that the solutions may be extremely sensitive to errors in these regions, and overshoot could cause a hump to "flip over" to the incorrect sign, resulting in solutions which are not of one sign. If this were the case, though, one would not necessarily expect the same sign flippings to occur when different numerical methods are applied to the equations. However, these solutions were also found by either Szeto or Holodniok, *et al.*

To resolve these questions it will be necessary to employ a numerical scheme which will be able to greatly increase the resolution of these solutions in the neighborhoods of the axial velocity zeroes. As the code we used to calculate these solutions was only designed to work with uniform meshes, we have only been able to increase resolution by adding more points uniformly throughout the interval, and this has produced no changes in the results. In the future, this problem will have to be solved using a code designed to use nonuniform meshes.

Part II: Equilibrium Chaos

CHAPTER 3

Equilibrium Chaos

We consider two examples of differential equations with free parameters whose solution paths exhibit an infinite number of folds. In observing the behavior of these solution paths, as well as that for the von Kármán swirling flows [29], Keller [21] conjectured that, like the period doubling in the Lorenz map [31], the ratios of the parameter values at these folds approach definite limits, and he termed this behavior "equilibrium chaos." Here, we show that his conjecture was indeed correct for the examples presented here and we determine these limits analytically.

3.1 The Bratu Problem

The first example is the Bratu Problem:

$$u_{rr} + \frac{n-1}{r} u_r + \mu e^u = 0 \tag{3.1.1a}$$

$$u_r(0) = u(1) = 0. \tag{3.1.1b}$$

This equation was studied by Bratu [2] and more recently by Gel´fand [8] as a model for the thermal self-ignition of chemically reacting gases inside an n-dimensional spherical vessel. In his paper Gel´fand considered the physical values n = 1,2,3 and sought the number of solutions to the problem for each value of μ. Here we will follow Joseph and Lundgren [13] and not restrict n.

Following Gel´fand we define $\nu \equiv n-1$, $\mu \equiv 2\lambda^2$, $\xi \equiv r/\lambda$, and when these are substituted into (3.1.1), we obtain

$$u_{\xi\xi} + \frac{\nu}{\xi} u_\xi + 2e^u = 0 \tag{3.1.2a}$$

$$u_\xi(0) = 0 \tag{3.1.2b}$$

$$u(\lambda) = 0. \tag{3.1.2c}$$

In order to study the character of the solutions of (3.1.2), we turn to the phase plane. To make the equation autonomous we introduce the transformation

$$u = v - 2\ln\xi \tag{3.1.3a}$$

$$\eta = \ln\xi \tag{3.1.3b}$$

which, when substituted into (3.1.2a) yields

$$v_{\eta\eta} + (\nu-1)v_\eta - 2(\nu-1) + 2e^v = 0. \tag{3.1.4}$$

This lends itself to phase plane analysis most easily after one more transformation. We let

$$z \equiv e^v = \xi^2 e^u \tag{3.1.5}$$

and

$$\psi \equiv v_\eta. \tag{3.1.6}$$

Then (3.1.4) becomes

$$\psi_\eta + (\nu-1)\psi - 2(\nu-1) + 2z = 0.$$

Using $z_\eta = v_\eta e^v = \psi z$, we obtain the first order system

$$\psi_\eta = 2(\nu-1) - (\nu-1)\psi - 2z \tag{3.1.7a}$$

$$z_\eta = \psi z. \tag{3.1.7b}$$

This system has two singular points. Linearization about $\psi = 2$, $z = 0$ shows that this is a saddle point for $\nu > 1$. When we linearize about the other singular point at $\psi = 0$, $z = \nu - 1$, we obtain the eigenvalues

$$-\frac{\nu-1}{2} \pm \sqrt{\left(\frac{\nu-1}{2}\right)^2 - 2(\nu-1)}$$

which means that this is a stable spiral (focus) point for $1 < \nu < 9$, and a saddle point for $\nu < 1$ or $\nu > 9$.

In order to solve (3.1.2), we need to find a trajectory for which the boundary conditions $u_\xi(0) = 0$ and $u(\lambda) = 0$ hold. In terms of the new variables

$$\frac{du}{d\xi} = \frac{du}{d\eta}\frac{d\eta}{d\xi} = \frac{du}{d\eta}\frac{1}{\xi} = \left[\frac{dv}{d\eta} - 2\right]\frac{1}{\xi}$$
$$= \frac{\psi - 2}{\xi}.$$

Therefore, $u_\xi = 0$ along $\psi = 2$. Now $\xi = 0$ corresponds to $\eta = -\infty$, so to have $u_\xi(0) = 0$, we need a trajectory which tends to $\psi = 2$ as the independent variable η tends to $-\infty$. But this is just the trajectory emanating from the saddle point in the positive z direction (we are only interested in real values of v, so $z = e^v > 0$). Figure 3.1 shows this trajectory which spirals into the focus for $1 < \nu < 9$.

We still need to satisfy the last boundary condition (3.1.2c). But using (3.1.5) we see that this just requires that the trajectory intersect the line $z = \lambda^2$ when $\eta = \ln \lambda$, and due to the translation invariance of the autonomous system (3.1.7), we are guaranteed that there is a solution for which $\eta = \ln \lambda$ at the point of intersection.

Now, if we label the intersection points of the trajectory with the z-axis as $z_1, z_2, z_3, \ldots, z_\infty$, where the index increases as η increases and z_∞ is the focus (see fig. 3.1), we can immediately see that (3.1.2) has no solutions for $\lambda > \sqrt{z_1}$ since the trajectory lies to the left of z_1 (note that $z_\eta = \psi z = 0$ at z_i). As λ is

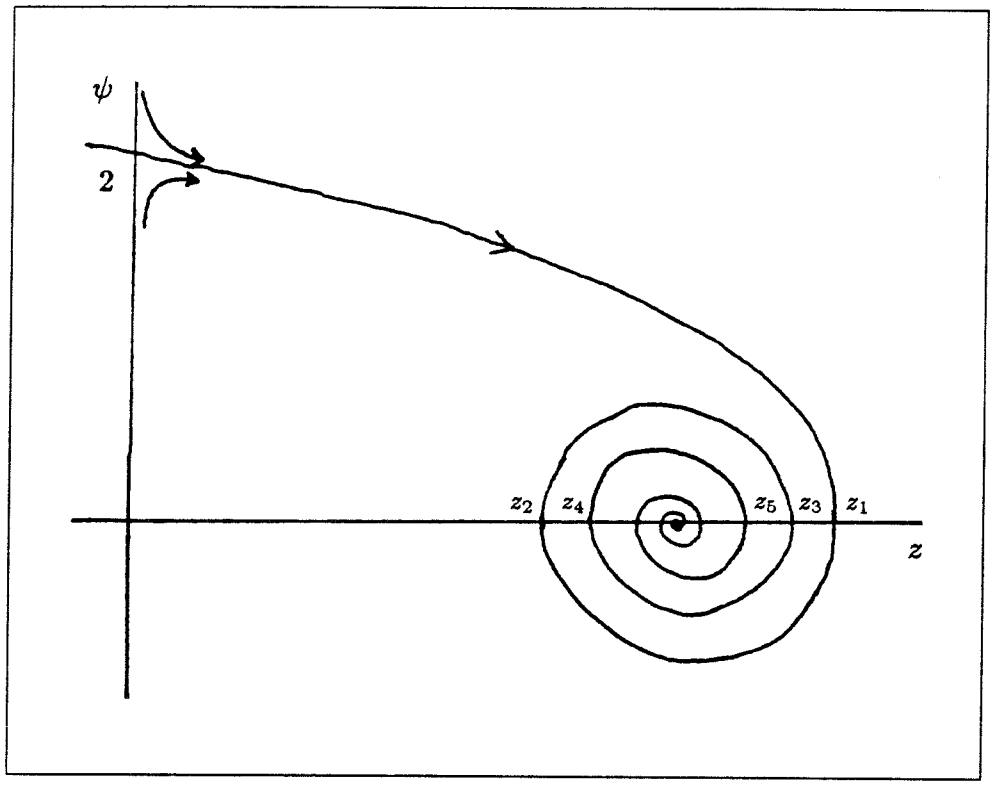

Figure 3.1. The trajectory emanating from the saddle point at $\psi = 2$, $z = 0$ is the only one for which the boundary condition (3.1.2b) is satisfied.

decreased, we find that the number of intersections of the line $z = \lambda^2$ with the trajectory will jump by two as each z_i is crossed; for $z > z_\infty = \nu - 1$, the jumps will be positive, and for $z < z_\infty$, the jumps will be negative. From this we see that each z_i corresponds to a fold in the solution curve of (3.1.2), and the value of λ at each fold is given by $\lambda_i = \sqrt{z_i}$. The solution curve is plotted in fig. 3.2.

The accumulation of these folds about the value $\lambda_\infty = \sqrt{\nu - 1}$ bears a striking resemblance to the accumulation of the period doubling bifurcations in the Lorenz map. It was this that led Keller to the conjecture that the ratio of the spacings between folds approaches a limit and to question whether that limit is "universal." To address these matters we look at the equation for the trajectory in the neighborhood of the spiral point. Linearizing about the spiral point, we

obtain the system

$$z'_\eta = (\nu - 1)\psi'$$

$$\psi'_\eta = -2z' - (\nu - 1)\psi'$$

where $z' = z - (\nu - 1)$ and $\psi' = \psi - 0$. The eigenvalues of the coefficient matrix above are

$$S_{1,2} = \frac{1-\nu}{2} \pm \sqrt{\left(\frac{1-\nu}{2}\right)^2 - 2(\nu - 1)}\,,$$

and if we use polar coordinates $r^2 = \psi'^2 + z'^2$, $\varphi = \tan^{-1}(\psi'/z')$, the solution of the linearized system may be written as (cf. [35])

$$r = C_1 \exp\{(S_1 + S_2)\eta/2\}$$

$$\varphi = \left[(S_1 - S_2)(\eta + C_2)\right]/2i.$$

Eliminating η yields

$$\begin{aligned} r &= C \exp\{(S_1 + S_2)i\varphi/(S_1 - S_2)\} \\ &= C \exp\left\{\frac{(1-\nu)i\varphi}{2\sqrt{\left(\frac{1-\nu}{2}\right)^2 - 2(\nu-1)}}\right\} \\ &= C \exp\left\{\sqrt{\frac{\nu-1}{9-\nu}}\,\varphi\right\} \\ &= C \exp\left\{\sqrt{\frac{n-2}{10-n}}\,\varphi\right\}. \end{aligned}$$

Defining $\beta \equiv \sqrt{(n-2)/(10-n)}$, we can write a sequence of the intersection points z_i as

$$z_i = \nu - 1 + Ce^{\beta 2\pi i}$$

$$z_{i+2} = \nu - 1 + Ce^{\beta 2\pi(i-1)}$$

$$z_{i+4} = \nu - 1 + Ce^{\beta 2\pi(i-2)}$$

Therefore, the ratio of the spacings between folds on one side of λ_∞ is

$$\begin{aligned}\frac{\lambda_i - \lambda_{i+2}}{\lambda_{i+2} - \lambda_{i+4}} &= \frac{z_i^{1/2} - z_{i+2}^{1/2}}{z_{i+2}^{1/2} - z_{i+4}^{1/2}} \\ &= \frac{\sqrt{\nu - 1 + Ce^{\beta 2\pi i}} - \sqrt{\nu - 1 + Ce^{\beta 2\pi(i-1)}}}{\sqrt{\nu - 1 + Ce^{\beta 2\pi(i-1)}} - \sqrt{\nu - 1 + Ce^{\beta 2\pi(i-2)}}} \\ &= \frac{\sqrt{1 + \frac{C}{\nu - 1}e^{\beta 2\pi i}} - \sqrt{1 + \frac{C}{\nu - 1}e^{\beta 2\pi(i-1)}}}{\sqrt{1 + \frac{C}{\nu - 1}e^{\beta 2\pi(i-1)}} - \sqrt{1 + \frac{C}{\nu - 1}e^{\beta 2\pi(i-2)}}}.\end{aligned}$$

For large i this gives

$$\begin{aligned}\frac{\lambda_i - \lambda_{i+2}}{\lambda_{i+2} - \lambda_{i+4}} &\sim \frac{e^{\beta 2\pi i} - e^{\beta 2\pi(i-1)}}{e^{\beta 2\pi(i-1)} - e^{\beta 2\pi(i-2)}} = \frac{1 - e^{-2\beta\pi}}{e^{-2\beta\pi}\left(1 - e^{-2\beta\pi}\right)} \\ &= e^{2\pi\beta}.\end{aligned}$$

Therefore,

$$\frac{\lambda_i - \lambda_{i+2}}{\lambda_{i+2} - \lambda_{i+4}} \to e^{2\pi\sqrt{\frac{n-2}{10-n}}} \qquad \text{as } i \to \infty. \tag{3.1.8}$$

Thus, for those values of n for which a spiral point exists in the phase plane $(2 < n < 10)$, we obtain an infinite sequence of folds in the solution curve, and the ratios of the spacings between folds approaches the limit in (3.1.8). We have used the box scheme and pseudo-arclength continuation to solve (3.1.1) numerically. The resulting folds are plotted in fig. 3.2.

Similarly, one can also find that

$$\frac{\lambda_i - \lambda_{i+1}}{\lambda_{i+1} - \lambda_{i+2}} \to -e^{\pi\sqrt{\frac{n-2}{10-n}}} \qquad \text{as } i \to \infty.$$

To see how fast these limits are approached we have calculated several of the λ_i's for the case of a spherical vessel $(n = 3)$. In this case the limiting value is $e^{2\pi/\sqrt{7}} = 10.74908703$ for the one-sided limit and its negative square root $-e^{\pi/\sqrt{7}} = -3.278580032$ using folds on both sides of $\lambda_\infty = 1$. The ratios are presented in Table 3.1 where we have defined

$$\Lambda_i \equiv \frac{\lambda_{2i-1} - \lambda_{2i+1}}{\lambda_{2i+1} - \lambda_{2i+3}} \qquad \text{and} \qquad \mathrm{R}_i \equiv \frac{\lambda_i - \lambda_{i+1}}{\lambda_{i+1} - \lambda_{i+2}}.$$

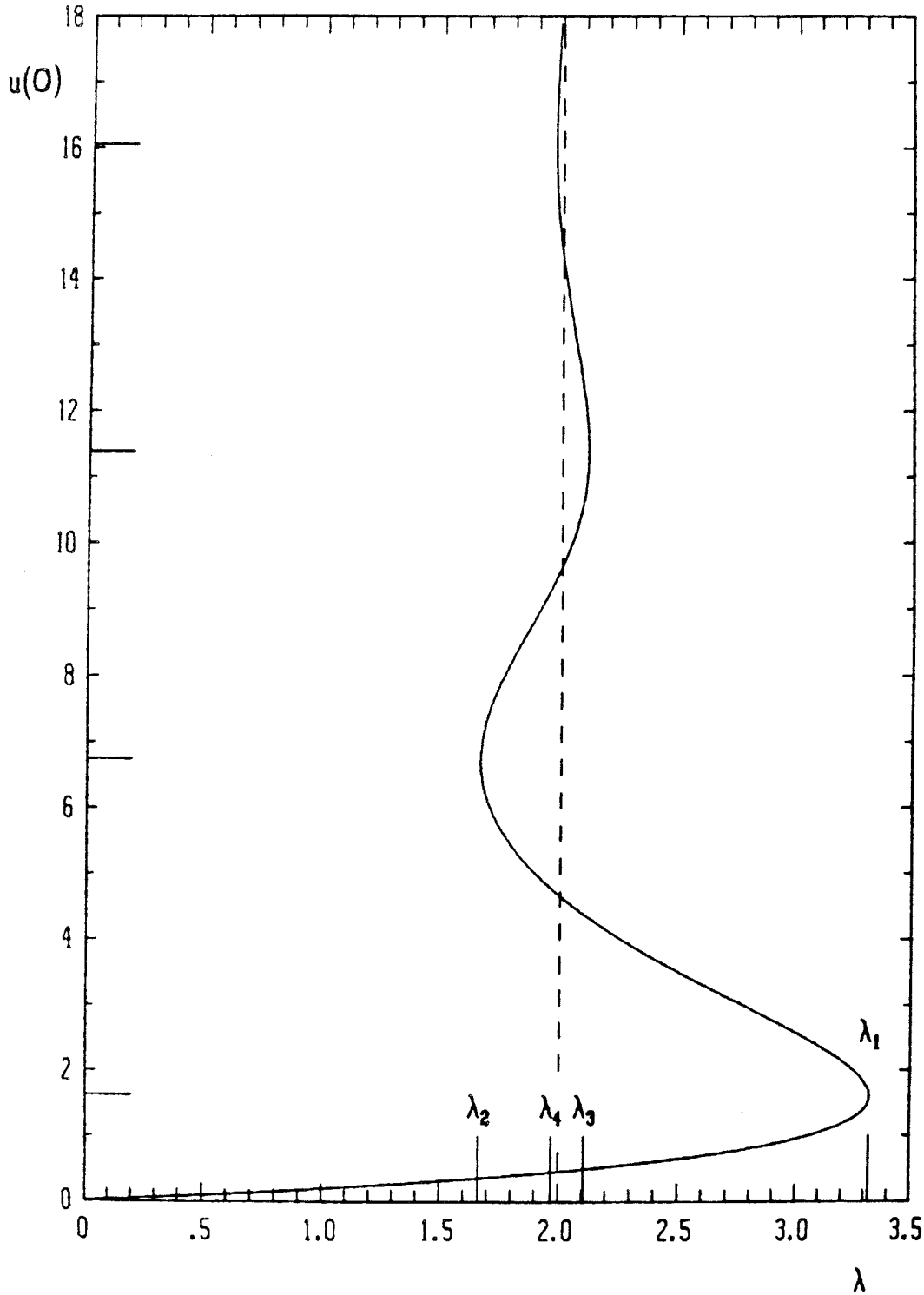

Figure 3.2. A plot of the value at zero of solutions of the Bratu problem as a function of λ. The folds are labeled by the values λ_i, where $\lambda_\infty = 2$ is the limiting value. Spacing between the folds approaches the value given in equation (3.1.8).

i	Λ_i	R_i
1	12.31121336	-3.73063
2	10.89192609	-3.149978
3	10.76236061	-3.318577627
4	10.75032171	-3.266454742
5	10.74920190	-3.282285217
6	10.7490977	-3.277450264
7	10.749088	-3.278924883
8	10.74909	-3.278474943
9		-3.278612087
10		-3.278570255
11		-3.278583014
⋮	⋮	⋮
∞	10.74908703	-3.278580032

Table 3.1. A study of the approach of the single-sided (Λ_i) and double-sided (R_i) fold spacing ratios to their limiting values for the Bratu problem in $n = 3$ dimensions.

Values of λ_i accurate to 16 figures were used to compile this table. Significant figures are lost in the calculation of Λ_i for $i \geq 6$ due to the differencing, so the ratios for $i > 8$ are not shown.

3.2 Buckling of Circular Membranes

Clearly, the results of Section 3.1 rely upon the presence of a stable focus in the phase plane of the differential equation. So any equation which possesses similar behavior in its phase plane will give rise to this same limiting behavior. As a second example, consider the generalization of the equation describing the equilibrium states of a circular shallow elastic membrane whose surface is subject to an axisymmetric pressure and edge thrusts [23]:

$$\frac{d^2u}{dr^2} + \frac{n-1}{r}\frac{du}{dr} + \frac{\lambda^\beta r^\mu}{(1-\alpha u)^{\beta-1}} = 0 \qquad (3.2.1a)$$

$$\lim_{r\to 0}\left|\frac{1}{r}\frac{du}{dr}\right| < \infty \tag{3.2.1b}$$

$$u(1) = 0 \tag{3.2.1c}$$

where $\mu \geq 0$, $\beta > 1$.

The study of (3.2.1) is similar to that done for (3.1.1) above. Following Kosecoff [23] we introduce the transformation

$$x = \ln r \tag{3.2.2a}$$

$$v(x) = (1 - \alpha u)r^{\gamma} \tag{3.2.2b}$$

where

$$\gamma \equiv -(\mu + 2)/\beta < 0. \tag{3.2.3}$$

Substituting (3.2.2) into (3.2.1a) we obtain

$$\frac{d^2v}{dx^2} - (2\gamma + 2 - n)\frac{dv}{dx} + \gamma(\gamma + 2 - n)v - \alpha\lambda^{\beta}v^{1-\beta} = 0. \tag{3.2.4}$$

Letting $\theta \equiv \gamma + 2 - n = \gamma - (n-2) = -\dfrac{\mu+2}{\beta} - (n-2)$, (3.2.4) becomes

$$\frac{d^2v}{dx^2} - (\gamma + \theta)\frac{dv}{dx} + \gamma\theta v - \alpha\lambda^{\beta}v^{1-\beta} = 0. \tag{3.2.5}$$

Now, $r = 1$ corresponds to $x = 0$ which, when used in (3.2.1c) and (3.2.2b), gives

$$v(0) = 1. \tag{3.2.6}$$

Using (3.2.2) the boundary condition (3.2.1b) becomes

$$\lim_{x\to -\infty} e^{-x(\gamma+2)}\left|\frac{dv}{dx} - \gamma v\right| < \infty. \tag{3.2.7}$$

To simplify the phase plane analysis we make one more transformation:

$$y(x) = \alpha\lambda^{\beta}v^{-\beta} \tag{3.2.8a}$$

$$z(x) = \frac{1}{v}\frac{dv}{dx}, \tag{3.2.8b}$$

which, when substituted into (3.2.5)-(3.2.7), gives the system

$$y_x = -\beta y z \tag{3.2.9a}$$

$$z_x = y - (z-\gamma)(z-\theta) \tag{3.2.9b}$$

$$\lim_{x\to-\infty} e^{-x(\gamma+2)}\,|z-\gamma|\,|y|^{-1/\beta} < \infty \tag{3.2.9c}$$

$$y(0) = \alpha\lambda^{\beta}. \tag{3.2.9d}$$

This system has three singular points for $n > 2$:

$$P_1: \quad y = 0, \quad z = \gamma$$

$$P_2: \quad y = 0, \quad z = \theta$$

$$P_3: \quad y = \gamma\theta, \quad z = 0.$$

P_1 is always a saddle point, and P_2 is an unstable node. When $(\gamma+\theta)^2 - 4\beta\gamma\theta < 0$, P_3 is a stable focus; otherwise, it is a stable node. Since we are interested in solutions with an infinite number of folds, we consider only the case where P_3 is a spiral point.

In [23] Kosecoff has performed a detailed study of the phase plane. He found that, as was the case for Bratu's equation, the only trajectories satisfying the boundary condition (3.2.9c) are the two leaving the saddle point P_1 (see fig. 3.3.) The trajectory which leaves in the positive y direction is attracted to the spiral point P_3. Imposing the boundary condition (3.2.9d) is as simple as finding the intersection of the trajectory with the line $y = \alpha\lambda^{\beta}$ and setting $x = 0$ at that point by the translation invariance property.

So, just as in the Bratu problem, the number of solutions is given by the number of intersections of a vertical line with the trajectory which spirals into the focus. Thus, the intersections of this trajectory with the y-axis give us the values of the folds in the solution curve of (3.2.1).

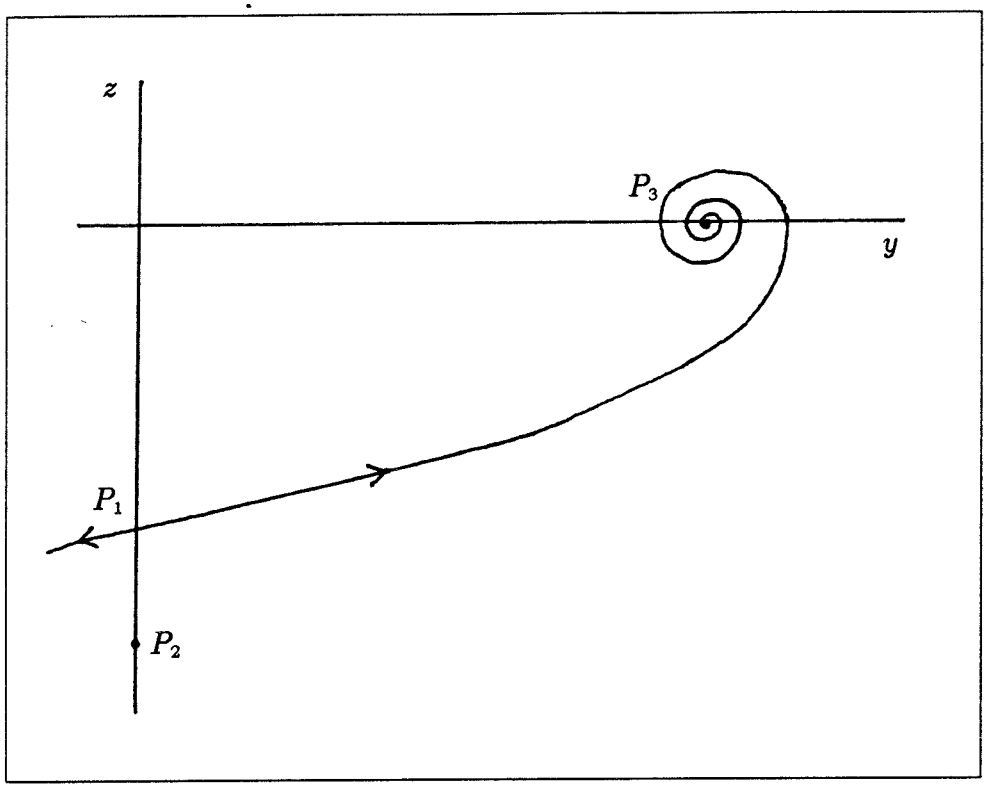

Figure 3.3. The trajectory emanating from the saddle point in the positive y direction is the only one for which the boundary condition (3.2.1b) is satisfied.

Linearizing about P_3 we find the integral curve

$$r = C \exp\left\{ \frac{(\gamma+\theta)i\varphi}{2\sqrt{\left(\frac{\gamma+\theta}{2}\right)^2 - \beta\gamma\theta}} \right\},$$

which, when written in terms of the original problem parameters, becomes

$$r = C \exp\left\{ \frac{-\varphi}{\sqrt{(\beta-1) - \frac{\beta^3(n-2)^2}{[2(\mu+2)+\beta(n-2)]^2}}} \right\}$$

$$\equiv Ce^{-\varphi/\Omega}.$$

Thus, the intersection points are given by

$$y_i = \gamma[\gamma - (n-2)] + Ce^{-2\pi i/\Omega},$$

where $y_i = \left(\alpha\lambda^\beta\right)_i$. Taking ratios as before,

$$\lim_{i\to\infty} \frac{y_i - y_{i+2}}{y_{i+2} - y_{i+4}} = \lim_{i\to\infty} \frac{\left(\alpha\lambda^\beta\right)_i - \left(\alpha\lambda^\beta\right)_{i+2}}{\left(\alpha\lambda^\beta\right)_{i+2} - \left(\alpha\lambda^\beta\right)_{i+4}}$$

$$= e^{2\pi/\Omega}. \tag{3.2.10}$$

Here, we have treated $\alpha\lambda^\beta$ as a single parameter, and it may be varied in any way that is desired.

To conclude we consider the question of "universality." The expressions (3.1.8) and (3.2.10) demonstrate clearly that there are no universal limiting values. In fact, by varying the parameters in the equations (e.g., n), the ratios obtained can take on any value from 1 to ∞. This, then, brings to mind the question as to how "universal" the Feigenbaum numbers really are. Of course, universality has been demonstrated in the case of some one-parameter families of maps [5]. But we wonder whether a mechanism similar to that presented here could be at work in some of the other places where this limiting behavior has been observed.

Part III: A Mesh Selection Algorithm for Two-Point Boundary Value Problems

CHAPTER 4

A Mesh Selection Algorithm for Two-Point Boundary Value Problems

4.1 Introduction

Here we will describe some of the work done toward the development of a code generator for solving two-point boundary value problems. The goals of this project are to design a code which will write programs to solve specific two-point boundary value problems depending on parameters. The code will take a description of the problem from the user and tailor a program suited for his particular problem. For example, if the problem depends on parameters, provisions for continuation will undoubtedly be desired, and thus provided. But in the case where the problem does not depend upon parameters, or where the user does not wish to employ continuation, those provisions will not be included in the code, thus making it smaller and more efficient.

As this is an ambitious project, it was decided that to get things going, we should start off with something manageable. So initially the class of problems we will be treating is restricted to first order systems with separated end conditions. Ideally, one would like to choose the method of solution of a problem based on the individual characteristics of the problem. But many problems can be treated by a good basic solution method. The first phase of the project was therefore aimed at developing such a method. The method proposed for solving these two-point boundary value problems is the box scheme using a variable mesh. This approach is designed to allow the solution of non-stiff systems and also moderately stiff

systems arising from continuation. In subsequent phases of the project, the code will be expanded to deal with more general problems and a wider variety of solution methods tailored for particular classes of problems.

This initial phase was split into two parts: the code generator and the numerical solver. The code generator was written by Dr. David Brown and allows the user to input his problem as it stands. Subroutines describing the problem are then generated to supply the numerical routines with the information necessary to solve the problem. These subroutines are combined with the numerical routines to form a complete FORTRAN source code which will solve just this particular problem. Source code is generated in order to allow the program to be customized to the problem at hand and to permit portability of the generated code.

In this work we will describe the basic solution method. The major part of the method is the mesh refinement algorithm. The next section will detail the theoretical basis for the method which chooses meshes by equidistributing the global error of the solution. The algorithm itself will be presented in the following section. We will close by presenting the behavior of the algorithm on some test problems.

4.2 Theoretical Considerations for Mesh Selection

We consider two-point boundary value problems of the form

$$Ny(x) \equiv y'(x) - f(x, y; \lambda) = 0, \qquad a < x < b; \tag{4.2.1a}$$

$$g(y(a), y(b); \lambda) = 0. \tag{4.2.1b}$$

Here y and f are n-vectors, λ is an m-vector and f is assumed to be in $C^M[a,b]$ for a sufficiently large M. Our goal is to design an algorithm for solving (4.2.1) which can be used as the basis for the code generator. Since continuation in λ is an important feature of the code, we seek to design a mesh refinement algorithm

which will tend to keep the number of grid points used to a minimum. Other authors [30] have proposed schemes which start with a basic mesh with a small number of grid points and then only add points. For continuation problems, where a great advantage can be gained by knowing the mesh used for the previous solution, this type of algorithm would be very inefficient. Therefore, we wish to design an algorithm which can decrease the number of mesh points used as well as increase it.

To solve two-point boundary value problems efficiently Keller and Pererya [22] have developed centered compact schemes. These schemes are applicable to systems of any order, but as our present work deals only with first order systems, our attention will be focused on just the first of these, the box scheme:

$$N_h u_j \equiv \frac{u_j - u_{j-1}}{h_j} - f\left(x_{j-1/2}, \frac{u_j + u_{j-1}}{2}; \lambda\right) = 0, \qquad 1 \le j \le J \tag{4.2.2a}$$

$$g(u_0, u_J; \lambda) = 0. \tag{4.2.2b}$$

Here, $x_0 \equiv a$, $x_j = x_{j-1} + h_j$ and $x_J \equiv b$. In addition to being compact, this scheme is also ideal for use with a variable mesh as it only employs two-point formulae.

In [16] Keller has derived the error expansions for the box scheme on a series of successively refined meshes. The zero-th order mesh is that defined in (4.2.2). Successive meshes are defined by

$$\begin{aligned} &x_0^{(k)} = a; \qquad x_j^{(k)} = x_{j-1}^{(k)} + h_j^{(k)}, \qquad 1 \le j \le J^{(k)}; \\ &x_{J^{(k)}}^{(k)} = b; \qquad h^{(k)} \equiv \max_j h_j^{(k)} \le K \min_j h_j^{(k)}; \end{aligned} \tag{4.2.3}$$

where the $h_j^{(k)}$'s are defined in terms of a piecewise C^∞-function $\phi(x)$ which has at worst jump discontinuities restricted to the points of the zero-th order mesh. Specifically, we have that

$$h_j^{(k)} = h^{(k)} \phi(x_{j-1/2}^{(k)}) \equiv h^{(k)} \phi\left(\tfrac{1}{2}(x_j^{(k)} + x_{j-1}^{(k)})\right), \qquad h^{(k+1)} < h^{(k)}.$$

Using this notation the global error can be expressed as

$$u_j^{(k)} - y(x_j^{(k)}) = \sum_{\nu=1}^{L} \left(\frac{h_j^{(k)}}{2} \right)^{2\nu} \varepsilon_\nu(x_j^{(k)}) + O\left({h^{(k)}}^{2L+2} \right). \tag{4.2.4}$$

The $\varepsilon_\nu(x)$ satisfy linear two-point boundary value problems of the form

$$\varepsilon_\nu'(x) - A(x)\varepsilon_\nu(x) = \phi^2 \Theta(x),$$

$$B_a \varepsilon_\nu(a) + B_b \varepsilon_\nu(b) = \gamma_\nu.$$

Θ_ν and γ_ν are just recursively defined expressions involving the local trunction errors of the box scheme. For example,

$$\Theta_1 = -\frac{1}{3!} y'''(x_{j-1/2}^{(k)}) + \frac{1}{2!} \frac{\partial f}{\partial y} \left(x_{j-1/2}^{(k)}, y(x_{j-1/2}^{(k)}), \lambda \right) y''(x_{j-1/2}^{(k)}),$$

which is just the first coefficient in the local truncation error expansion. See Keller [15] for the definitions of Θ_ν and γ_ν for the case when f is linear in y, and Gragg [9] for more general expressions.

The expansion (4.2.4) is derived by showing that

$$N_h \left[u_j^{(k)} - y(x_j^{(k)}) - \sum_{\nu=1}^{L} \left(\frac{h_j^{(k)}}{2} \right)^{2\nu} \varepsilon_\nu(x_j^{(k)}) \right] = O\left({h^{(k)}}^{2L+2} \right).$$

Then one uses the stability of the box scheme for initial value problems to obtain the result. Specifically, this is done by showing that the result holds for $j = 0$ and marching in j up to $j = J^{(k)}$. But this could just as well be done by demonstrating the result for $j = J^{(k)}$ and marching down to $j = 0$. In this case one would obtain an expression identical to (4.2.4) except that $h_j^{(k)}$ would be replaced by $h_{j+1}^{(k)}$. We shall take advantage of both of these expansions of the global error.

Given these expressions we can use an idea due to de Boor [6] to select a mesh for the problem. We wish to choose the net to minimize the global error. To

define what we mean by minimize, we first need some notation. Let $|\cdot|$ denote a vector norm for the the n-vectors $u_j^{(k)}$, y and ε_ν. (In our numerical work we have used the infinity norm.) Define $\|\cdot\|_{(j)}^{(k)}$ by

$$\|z\|_{(j)}^{(k)} \equiv \sup_{x_{j-1}^{(k)} \le x \le x_j^{(k)}} |z(x)|,$$

where z is an n-vector. Finally, let

$$\|u^{(k)} - y(x^{(k)})\|_\infty \equiv \max_j |u_j^{(k)} - y(x_j^{(k)})|.$$

Now we may proceed. From (4.2.4) we obtain

$$\begin{aligned} |u_j^{(k)} - y(x_j^{(k)})| &\le \left(\frac{h_j^{(k)}}{2}\right)^2 |\varepsilon_1(x_j^{(k)})| + O\left(h^{(k)^4}\right) \\ &\le \left(\frac{h_j^{(k)}}{2}\right)^2 \|\varepsilon_1\|_{(j)}^{(k)} + O\left(h^{(k)^4}\right). \end{aligned}$$

Therefore,

$$\|u^{(k)} - y(x^{(k)})\|_\infty \le \max_j \left(\frac{h_j^{(k)}}{2}\right)^2 \|\varepsilon_1\|_{(j)}^{(k)} + O\left(h^{(k)^4}\right). \tag{4.2.5}$$

From this estimate we have that, for $h^{(k)}$ sufficiently small,

$$\|u^{(k)} - y(x^{(k)})\|_\infty \le C \max_j \left(\frac{h_j^{(k)}}{2}\right)^2 \|\varepsilon_1\|_{(j)}^{(k)}, \tag{4.2.6}$$

where the constant C is independent of k since the $\varepsilon_\nu(x)$ are independent of the mesh and $h^{(k)} \le h^{(0)}$.

Now the mesh selection strategy is clear. We choose the $h_j^{(k)}$ to minimize

$$\max_j \left(\frac{h_j^{(k)}}{2}\right)^2 \|\varepsilon_1\|_{(j)}^{(k)},$$

which (see [6]) simply requires setting

$$\left(\frac{h_j^{(k)}}{2}\right)^2 \|\varepsilon_1\|_{(j)}^{(k)} = \text{constant}, \qquad j = 1, \ldots, J^{(k)}. \tag{4.2.7}$$

Thus, to obtain a specified global error tolerance ERRGLB, we need to choose this constant to be ERRGLB/C, where C comes from equation (4.2.6). If the higher order terms in (4.2.5) are small, then C will be near unity. Indeed, the value of the constant needed in (4.2.7) provides an estimate of the importance of these higher order terms and hence gives us a rough idea of how well the mesh has been chosen.

In order to perform this equidistribution of the global error, however, we need to know $\varepsilon_1(x)$. But we can obtain an estimate of this from Richardson extrapolation. If we choose the $(k+1)$-st mesh such that $x_{l_j}^{(k+1)} = x_j^{(k)}$, $j = 1, \ldots, J^{(k)}$, then we may write

$$u_j^{(k)} - y(x_j^{(k)}) = \left(\frac{h_j^{(k)}}{2}\right)^2 \varepsilon_1(x_j^{(k)}) + O\left(h^{(k)\,4}\right) \qquad 1 \le j \le J^{(k)} \qquad (4.2.8a)$$

$$u_{l_j}^{(k)+1} - y(x_{l_j}^{(k+1)}) = \left(\frac{h_{l_j}^{(k+1)}}{2}\right)^2 \varepsilon_1(x_{l_j}^{(k+1)}) + O\left(h^{(k+1)\,4}\right), \qquad (4.2.8b)$$

Subtracting (4.2.8b) from (4.2.8a) and solving for $\varepsilon_1(x_j^{(k)})$, we find

$$\hat{\varepsilon}_1(x_j^{(k)}) = 4\left\{\frac{u_j^{(k)} - u_{l_j}^{(k+1)}}{h_j^{(k)\,2} - h_{l_j}^{(k+1)\,2}}\right\} + O\left(h^{(k)\,2}\right) \qquad 1 \le j \le J^{(k)}. \qquad (4.2.9)$$

where the $\hat{}$ indicates that this estimate is based on the global error expansion obtained by marching to the right (equation (4.2.4)). If we had used the alternate form of the global error we would have obtained

$$\tilde{\varepsilon}_1(x_j^{(k)}) = 4\left\{\frac{u_j^{(k)} - u_{l_j}^{(k+1)}}{h_{j+1}^{(k)\,2} - h_{l_{j+1}}^{(k+1)\,2}}\right\} + O\left(h^{(k)\,2}\right) \qquad 0 \le j \le J^{(k)} - 1. \qquad (4.2.10)$$

There is really no reason to favor one estimate over the other. So for the sake of symmetry it seems reasonable to combine the two by averaging. Thus, we obtain

$$\begin{aligned} \varepsilon_1(x_0^{(k)}) &\approx \tilde{\varepsilon}_1(x_0^{(k)}) \\ \varepsilon_1(x_j^{(k)}) &\approx \frac{1}{2}\left[\hat{\varepsilon}_1(x_j^{(k)}) + \tilde{\varepsilon}_1(x_j^{(k)})\right], \qquad 1 \le j \le J^{(k)} - 1 \\ \varepsilon_1(x_{J^{(k)}}^{(k)}) &\approx \hat{\varepsilon}_1(x_{J^{(k)}}^{(k)}) \end{aligned} \qquad (4.2.11)$$

Now, if we let $\kappa \equiv \max_j h_j^{(k)}/h_{j+1}^{(k)} \leq K$, then comparing (4.2.9) and (4.2.10) we have that

$$\frac{1}{\kappa^2}\hat{\varepsilon}_1(x_j^{(k)}) \leq \tilde{\varepsilon}_1(x_j^{(k)}) \leq \kappa^2 \hat{\varepsilon}_1(x_j^{(k)}), \qquad 1 \leq j \leq J^{(k)} - 1.$$

This suggests that keeping κ relatively small will give us a better estimate of ε_1. There is a trade-off, though, since this could interfere with the selection of the most equidistributing mesh. However, in our numerical examples we have found that even for stiff problems the mesh selected has been unaffected by enforcing values of $\kappa \approx 4$.

4.3 The Mesh Selection Algorithm

Here we describe the algorithm we use to implement the mesh selection strategy described in Section 4.2. In order to implement this stategy, the algorithm must accomplish several things at the same time. Ultimately, of course, it must solve the two-point boundary value problem. But in order to do this, it needs to estimate the leading global error term $\varepsilon_1(x)$ and from this estimate choose an equidistributing mesh. Naturally, there is a great interplay among these different sections of the algorithm and errors in one of them tend to compound by deleteriously affecting the other two. Therefore, it is necessary to proceed cautiously, especially at the beginning, in order to obtain approximations which are consistent with each other; this will produce the best results in the fastest way.

The basic structure of the algorithm is this: Solve the problem on a given starting mesh using Newton's method (assuming the problem is nonlinear). Check to see if the error is satisfactory. If so, we are done. If not, we refine the mesh, re-solve and check the error. We repeat the refinement loop until the error is satisfactory or until we have iterated more than an acceptable number of times. In this case the refinement loop diverges and we report our most recent attempt

at a solution. As a starting mesh we use a uniform net with a small number of points, say 10, or, if we are in the middle of a continuation, we use the mesh from the last solution. More elaborate initial guesses such as an Euler extrapolation of the last two meshes could also be considered.

To decide whether the error is satisfactory we first estimate it by performing a Richardson extrapolation. Then we calculate the maximum error and the average error (based on infinity norms). The error is considered well distributed if MAXERR $\leq 2 *$ AVGERR. The criteria for a satisfactory error, then, are that the error is well distributed and that MAXERR $\leq$ ERRGLB, where ERRGLB is a preset error tolerance. ERRGLB is not intended to be a measure of the final absolute error since if the error is satisfactory, we employ the Richardson extrapolation already carried out to increase the accuracy to $O(h^4)$. Instead, ERRGLB is used to control the density of mesh points selected and so should not be made too small. We have used values on the order of 10^{-2} in our calculations. To decrease the error beyond the limits of the fourth order method, higher order extrapolations (or deferred corrections) should be performed on the final mesh rather than increasing the number of points by lowering ERRGLB. Due to its use, however, ERRGLB does provide a (generous) upper bound for the true error in the solution.

To perform the mesh refinement we estimate ε_1 as in equation (4.2.11). This estimate is only improved as long as the error is still considered not well distributed. Once it has reached this level of refinement, we freeze $\varepsilon_1(x)$ at its present value and use this estimate in subsequent refinements. With a given estimate for ε_1, either frozen or in transition, we then pick a value for the variable ERRTOL and let this be the constant in the right-hand side of (4.2.7). Proceeding to the right from $j = 1$, we solve successively for the $h_j^{(k)}$'s by bisection. As mentioned above, it is prudent to keep the ratio of successive step sizes from becoming too

big or too small. So if a step size ratio is bigger than κ or smaller than $1/\kappa$, where κ is a pre-specified constant, we adjust the step to keep the ratio within these limits. In addition, we define a maximum allowable step size in order to keep the constant K in (4.2.3) under control and to enforce sufficient resolution of plotted results.

When we get to the right-hand boundary, we extend $\varepsilon_1(x)$ to the right by setting it equal to its value at $x = b$. The resulting mesh thus extends beyond $x = b$. But the x_j as chosen define a mesh function on $[a, b+\epsilon]$ onto which we may interpolate a mesh which exactly fits on $[a, b]$. All the step sizes on this mesh are slightly smaller than those on the original overlapping mesh, so they are no longer quite equidistributed. But (4.2.7) is satisfied for the current value of ERRTOL if we replace the "=" with a "$\leq$." To help insure that a poor estimate of ε_1 does not cause too much damage, we impose the further restriction that the number of mesh points may not increase by more than 100% nor decrease by more than 33%. With the mesh so chosen, the previously obtained solution is then interpolated onto this mesh and used as an initial guess for the new solution. The problem is then re-solved and the error again checked.

Choosing a value for ERRTOL is a very important part of the process. As explained in the text after equation (4.2.7), ERRTOL should end up being equal to ERRGLB/C, where C comes from (4.2.6). If the leading term in the error expansion is a good estimate of the error, then $C \geq 1$ will be near unity. Thus, ERRTOL will ultimately be slightly less than ERRGLB. But in order to keep the different sections of the solution process consistent with each other, this final value must be approached carefully.

The specific method of approach is chosen by classifying the current error as NONUNI, TOOBIG or TOOSML. NONUNI means that ε_1 has not yet been well enough approximated to be used. TOOBIG means that ε_1 is good

enough to trust (and so its value has been frozen), but the maximum error is still too big. Finally, TOOSML indicates that ε_1 is well enough approximated, but the error is so small that there are too many points in the mesh. In order to perform continuation efficiently, it is necessary to remove the extra points.

The error is defined as NONUNI if it is not well distributed. In this case we have to proceed carefully to keep the three sections of the solution process consistent with each other. It is pointless to try to use a lot of mesh points at this point since they are not going to be placed in the proper positions. So we build up the number of mesh points gradually by enforcing three refinements with ERRTOL equal successively to 2 * ERRGLB, 1.5 * ERRGLB and ERRGLB. In practice we have found that these three refinements are generally sufficient to make the error well distributed. Of course, this would not be the case for a problem where the higher order terms in the error expansion are so important that the "well distributed" criterion cannot be satisfied even if ε_1 were known exactly. To deal with such cases, even if the error is still not well distributed after these three refinements, we freeze ε_1 anyway. Further refinements are then made according to whether the error is TOOBIG or TOOSML, and we relax the "well distributed" requirement.

The error is defined as TOOBIG if the error is well distributed (except for the case mentioned above) and AVGERR $\geq$ ERRGLB/2, but MAXERR $>$ ERRGLB. At this point we are basically trying to find the proper value of C. The last value was too small for the last estimate of ε_1. If we are willing to keep refining ε_1 with this value of C held fixed, it might turn out that this value is large enough for a sufficiently well approximated ε_1. This approach would produce a mesh with the fewest number of points. But it would also be costly and not guaranteed to succeed. So we proceed by decreasing ERRTOL by a factor of ERRMAX/ERRGLB or

15%, whichever causes the biggest decrease in ERRTOL. In the case of a not well distributed error, the factor ERRMAX/ERRGLB could be a great deal too large. In this case we treat ERRMAX as if it were only half as high above ERRGLB as it really is, and so multiply ERRTOL by $2 * \text{ERRGLB}/(\text{ERRMAX} + \text{ERRGLB})$ to obtain its new value. For the case of the first iteration, we use ERRTOL = ERRGLB.

The last error classification is TOOSML. This is when the error is well distributed (except as noted above), MAXERR $\leq$ ERRGLB, but AVGERR $<$ ERRGLB/2. We could certainly stop refining at this point, but the last value of C was clearly bigger than it needed to be. We can save ourselves the added cost of starting future solutions with too many mesh points at the expense of one more iteration now if we decrease C some and solve again. Considering this to be a wise investment, we multiply ERRTOL by $\max\{1.15, \frac{1}{2}\text{ERRGLB}/\text{ERRMAX}\}$ and solve again. For the case of the first iteration, we use ERRTOL = ERRGLB. To prevent cycling, the factors used for adjusting ERRTOL when the error is TOOBIG or TOOSML are reduced if the new value of ERRTOL would be greater than a previous TOOBIG value or smaller than a previous TOOSML value. A TOOSML solution is accepted if the next predicted ERRTOL value would cause the error to be TOOBIG.

4.4 Examples

Now we present examples of the meshes produced by this algorithm for some test problems. In the figures to follow, NPTS is the number of intervals used in the solution, MSHCNT is the total number of meshes tried on the problem (i.e., one more than the number of refinements since the initial mesh is counted); the other program variables have been defined above. The mesh used is indicated by the tick marks on the upper axis.

Problem 4.4.1

$$y_1' = y_2,$$

$$y_2' = \frac{1}{\varepsilon}(y_1 + \cos^2 \pi x) + 2\pi^2 \cos 2\pi x,$$

$$y_1(0) = y_1(1) = 0.$$

Exact solution:

$$y_1(x) = \frac{e^{-\sqrt{\frac{1}{\varepsilon}}}}{1 + e^{-\sqrt{\frac{1}{\varepsilon}}}} e^{\sqrt{\frac{1}{\varepsilon}}x} + \frac{1}{1 + e^{-\sqrt{\frac{1}{\varepsilon}}}} e^{-\sqrt{\frac{1}{\varepsilon}}x} - \cos^2 \pi x,$$

$$y_2(x) = \frac{\sqrt{\frac{1}{\varepsilon}} e^{-\sqrt{\frac{1}{\varepsilon}}}}{1 + e^{-\sqrt{\frac{1}{\varepsilon}}}} e^{\sqrt{\frac{1}{\varepsilon}}x} + \frac{\sqrt{\frac{1}{\varepsilon}}}{1 + e^{-\sqrt{\frac{1}{\varepsilon}}}} e^{-\sqrt{\frac{1}{\varepsilon}}x} + \pi \sin 2\pi x.$$

Stöer and Bulirsch [42] used this problem with $\varepsilon = 0.025$ to compare various two-point boundary value problems. It was selected because of the difficulties it poses for methods based on standard initial value problem techniques. The solution has boundary layers of width $O(\sqrt{\varepsilon})$ at both boundaries.

In fig. 4.1 the solution for $\varepsilon = 0.025$ is shown. This was obtained from an initial uniform mesh with ten intervals. The value of ERRGLB used was $5 \cdot 10^{-2}$ and the true error in the solution was calculated to be $1.818 \cdot 10^{-4}$, consistent with the fourth order scheme used. This solution was then continued to $\varepsilon = 0.001$ and 0.00025, the mesh from the previous solution being used as the starting mesh for the current solution. The computed solutions are shown in figs. 4.2 and 4.3. The actual errors for these solutions are $2.93 \cdot 10^{-4}$ and $1.520 \cdot 10^{-3}$, respectively.

Problem 4.4.2

$$y_1' = y_2,$$

$$\varepsilon y_2' = y_1 - (x^3 - \tfrac{1}{2}x)y_2,$$

$$y_1(-1) = 1, \quad y_1(1) = 2.$$

This was given in [24] as a test problem for an upwind differencing scheme. The solution y_1 is smooth as $\varepsilon \to 0$ except for corner layers at $\pm\sqrt{0.5}$. In figs. 4.4 and 4.5, we present the calculated solutions for $\varepsilon = 0.01$ and 0.0001, respectively.

The first solution was obtained by using an initial uniform mesh with ten intervals. This was then continued to $\varepsilon = 0.001$ and the final mesh for this value of ε used to start off the solution for fig. 4.5.

The final example is a model problem based on the equations describing the electric potential and charge distribution in a semi-conductor under the influence of an external electric field [3].

Problem 4.4.3

$$
\begin{aligned}
y_1' &= y_2, \\
y_2' &= 1 - y_3, \\
y_3' &= y_4, \\
\varepsilon y_4' &= -y_3(1 - y_3) - y_4 y_2, \\
y_1(0) = 0, &\quad y_1(1) = \alpha, \\
y_3(0) = 1, &\quad y_3(1) = 0.
\end{aligned}
$$

Here, y_1 represents the potential in the semi-conductor and y_3 is the electron density.

For α between 0 and 1 and ε small, the solutions have two outer regions and one internal layer connecting them. In the left outer region, y_1 is nearly zero and y_3 is almost identically equal to one. On the right, y_1 is quadratic and y_3 is essentially zero. Plots of the solutions for two values of ε are shown in figs. 4.6 and 4.7. These were obtained by continuation in ε. As $\alpha \to 1$, the left outer region disappears as the internal layer moves over to the left-hand boundary. Plots of the solutions for $\alpha = 1$ are shown in figs. 4.8 and 4.9.

No sophisticated continuation techniques were used in any of the three test problems. Except for the beginning solutions in a continuation run, which were obtained by starting with a uniform ten-interval mesh, all mesh refinements began with the mesh from the previous solution. The continuation steps used in these

test problems were quite a bit larger than we would normally expect to use in real problems (e.g., the flow between rotating coaxial disks). Nevertheless, the algorithm was able to handle most situations without a great deal of difficulty. The use of the large steps, without any Euler-like predictor, did, of course, mean that the initial nets were poor starting places. Typically, this caused the initial error to be poorly distributed and began the three-step improvement process. For some of the problems, these three steps were sufficient to refine the mesh (hence, MSHCNT = 4). For more abrupt continuation steps or for more difficult problems, a couple of extra refinements were required beyond this to bring the error down below the tolerance.

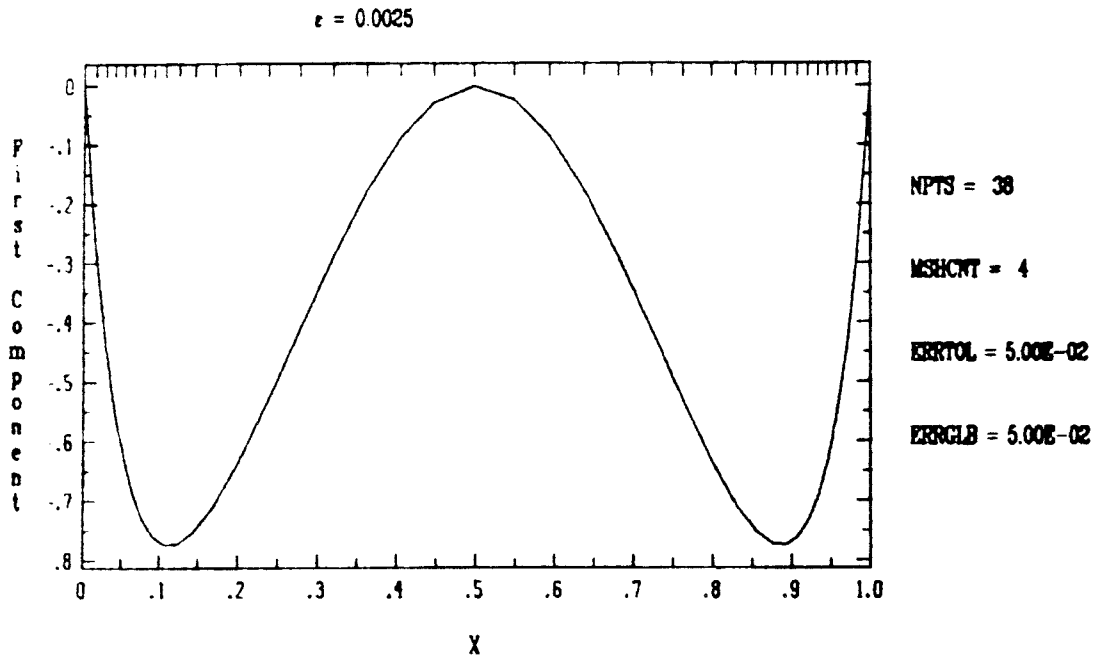

Figure 4.1a. Solution of $y'' = (1/\varepsilon)(y + \cos^2 \pi x) + 2\pi^2 \cos 2\pi x$, $y(0) = y(1) = 0$.

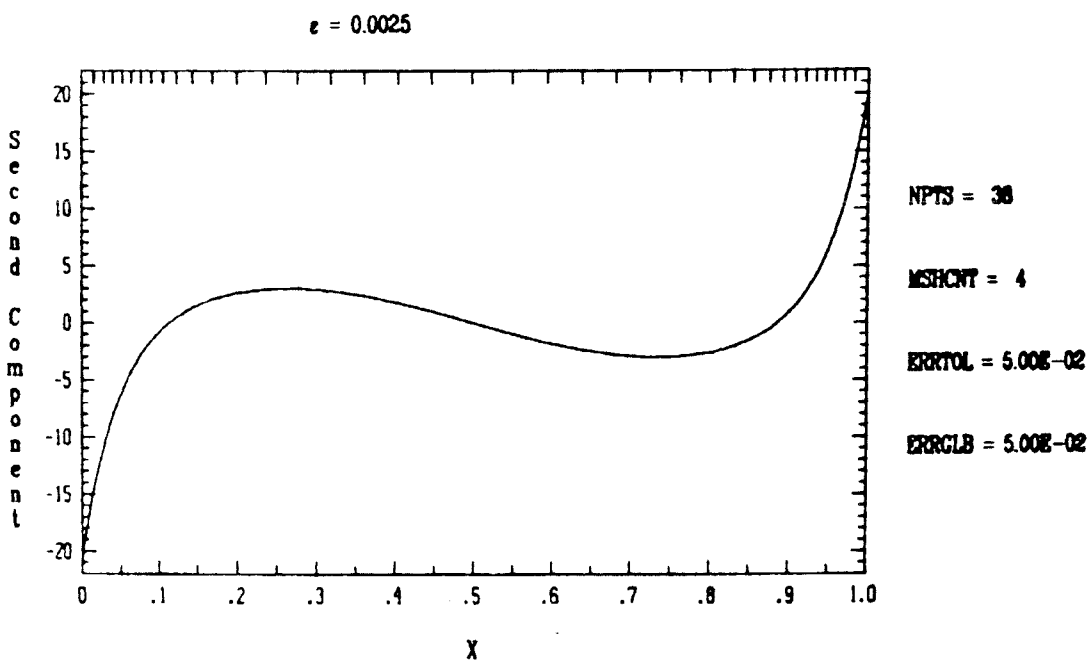

Figure 4.1b. Derivative of above solution.

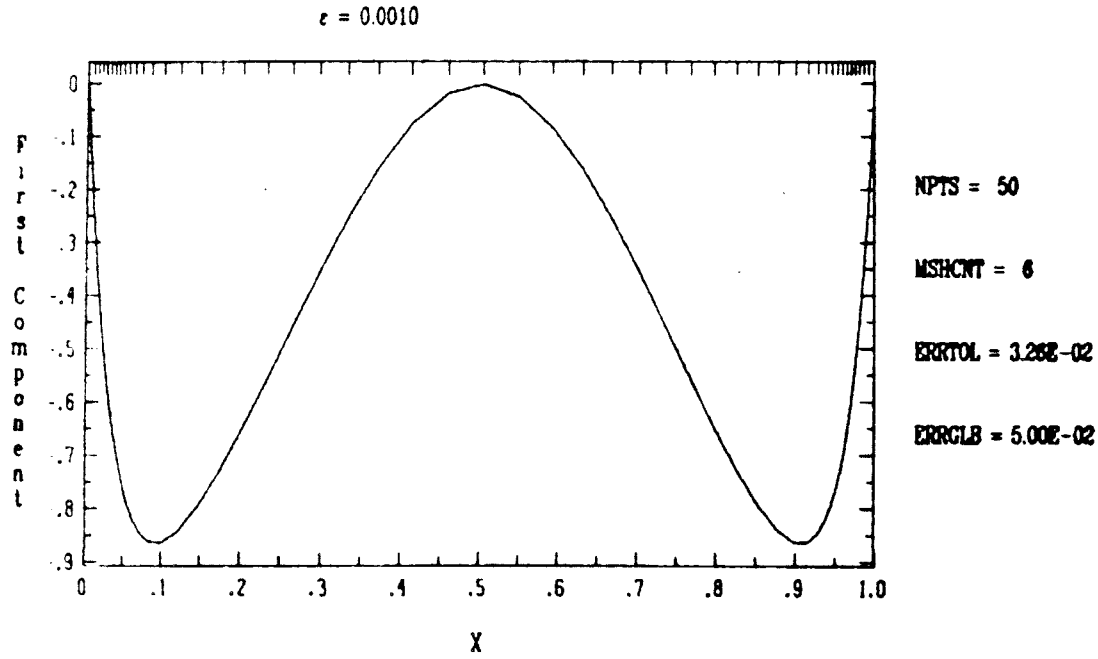

Figure 4.2a. Solution of $y'' = (1/\varepsilon)(y + \cos^2 \pi x) + 2\pi^2 \cos 2\pi x$, $y(0) = y(1) = 0$.

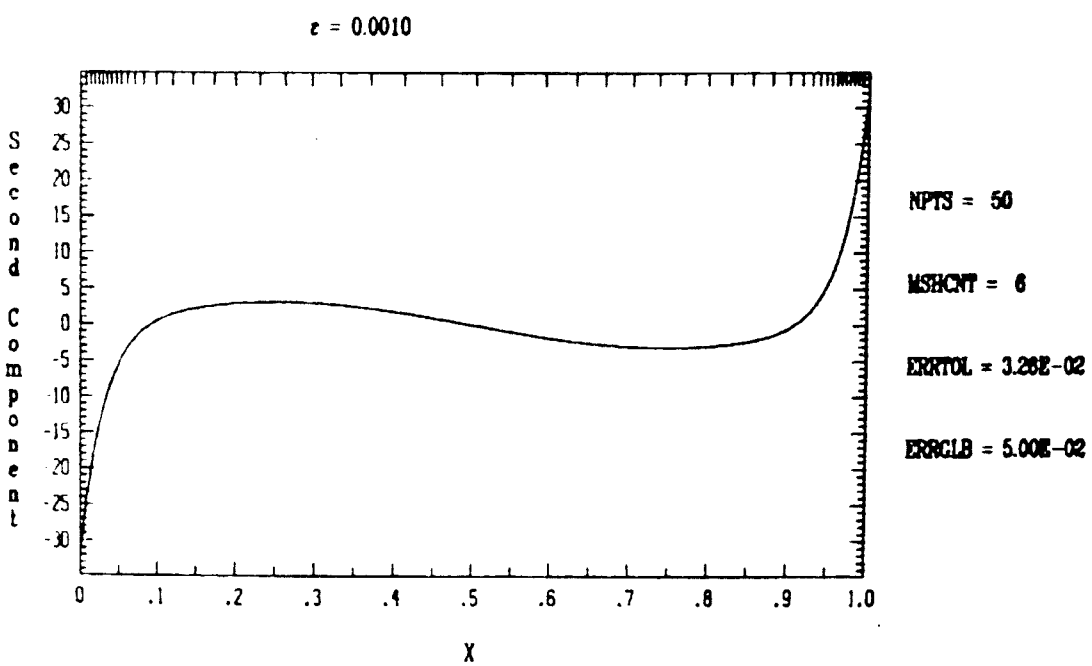

Figure 4.2b. Derivative of above solution.

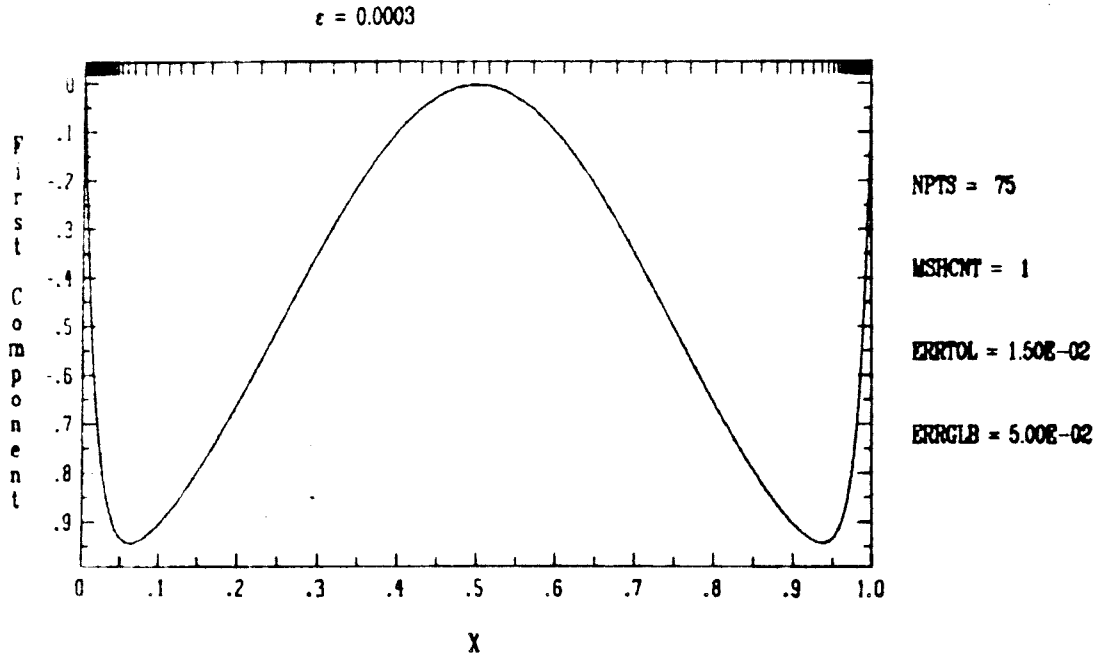

Figure 4.3a. Solution of $y'' = (1/\varepsilon)(y + \cos^2 \pi x) + 2\pi^2 \cos 2\pi x$, $y(0) = y(1) = 0$.

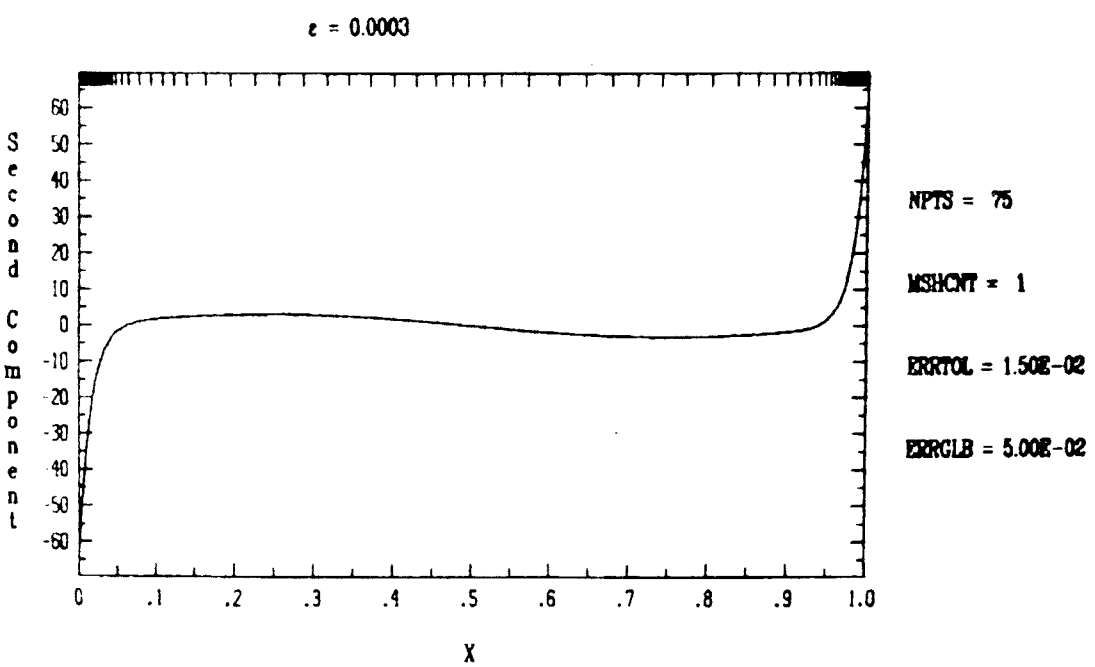

Figure 4.3b. Derivative of above solution.

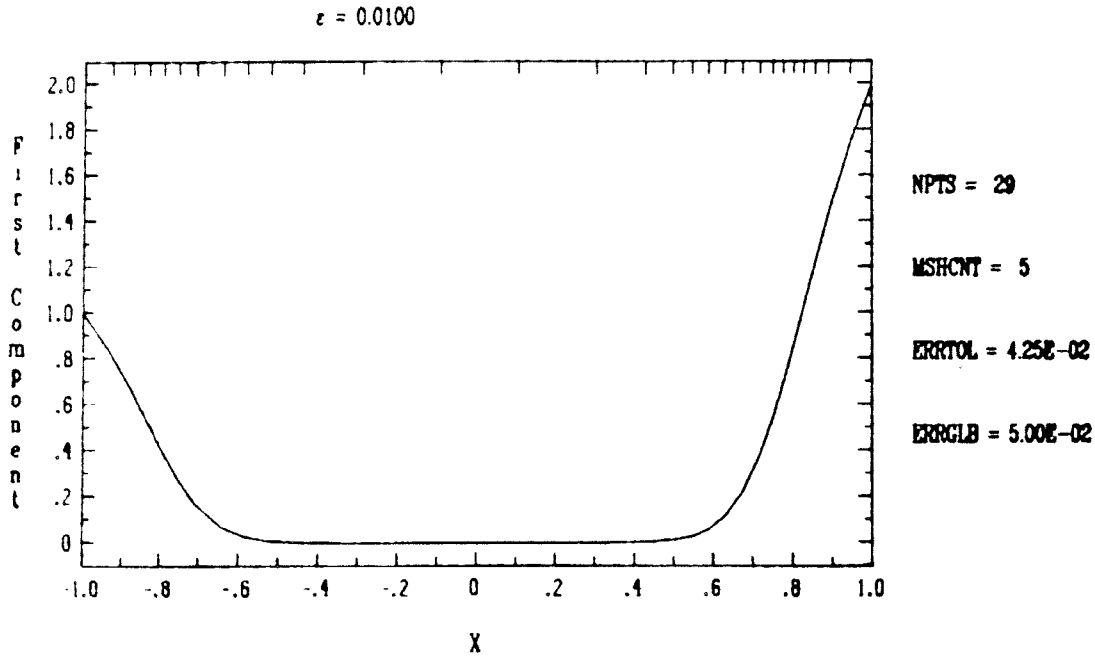

Figure 4.4a. Solution of $\varepsilon y'' + (x^3 - \frac{1}{2}x)y' - y = 0$, $y(-1) = 1$, $y(1) = 2$.

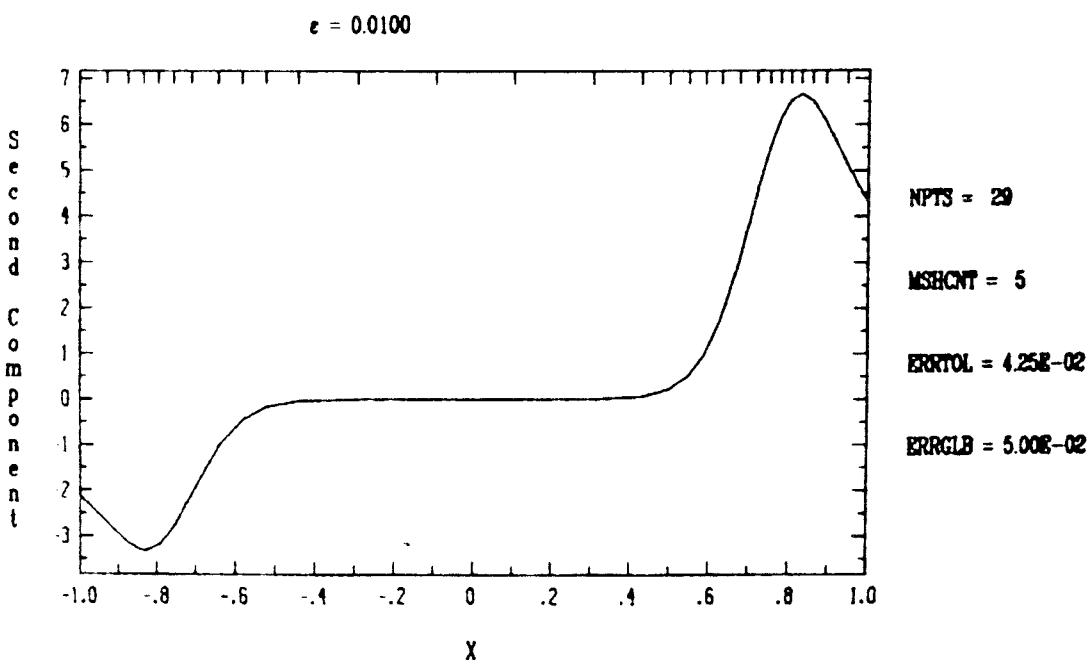

Figure 4.4b. Derivative of above solution.

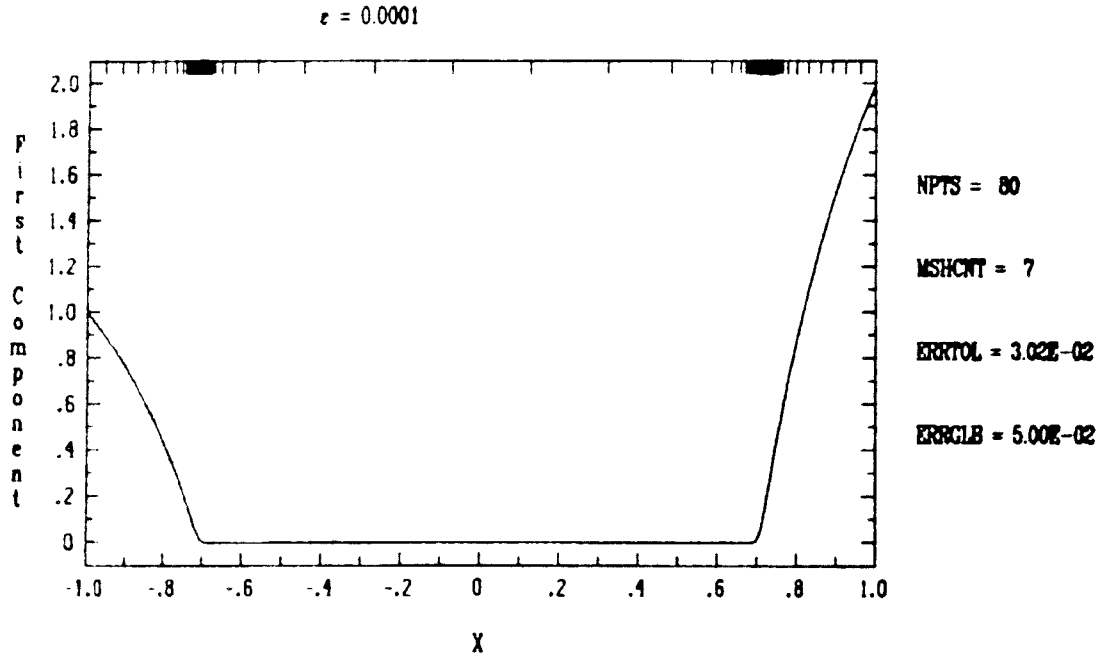

Figure 4.5a. Solution of $\varepsilon y'' + (x^3 - \frac{1}{2}x)y' - y = 0$, $y(-1) = 1$, $y(1) = 2$.

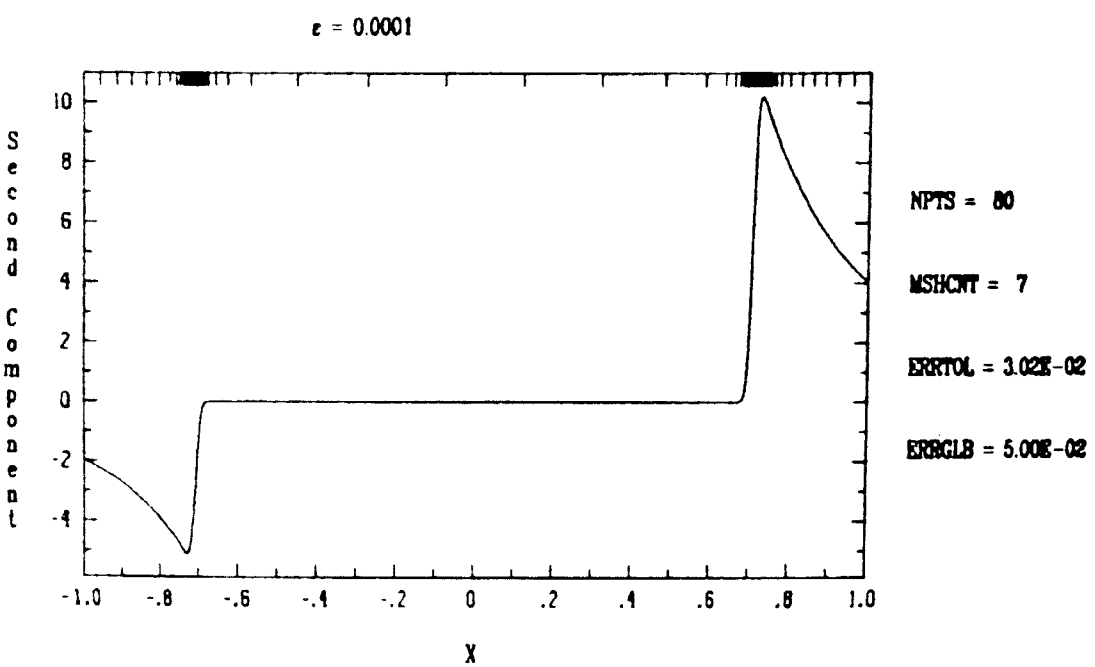

Figure 4.5b. Derivative of above solution.

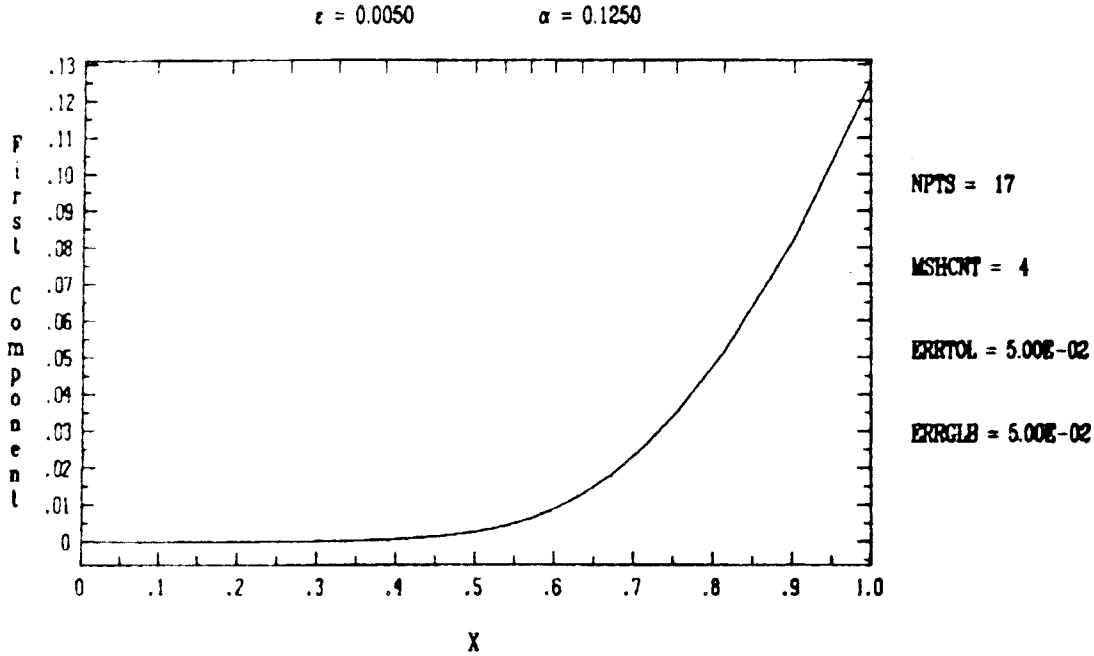

Figure 4.6a. The solution u of $u'' = 1 - v$, $\varepsilon v'' + (vu')' = 0$, $u(0) = 0$, $u(1) = \alpha$, $v(0) = 1$, $v(1) = 0$.

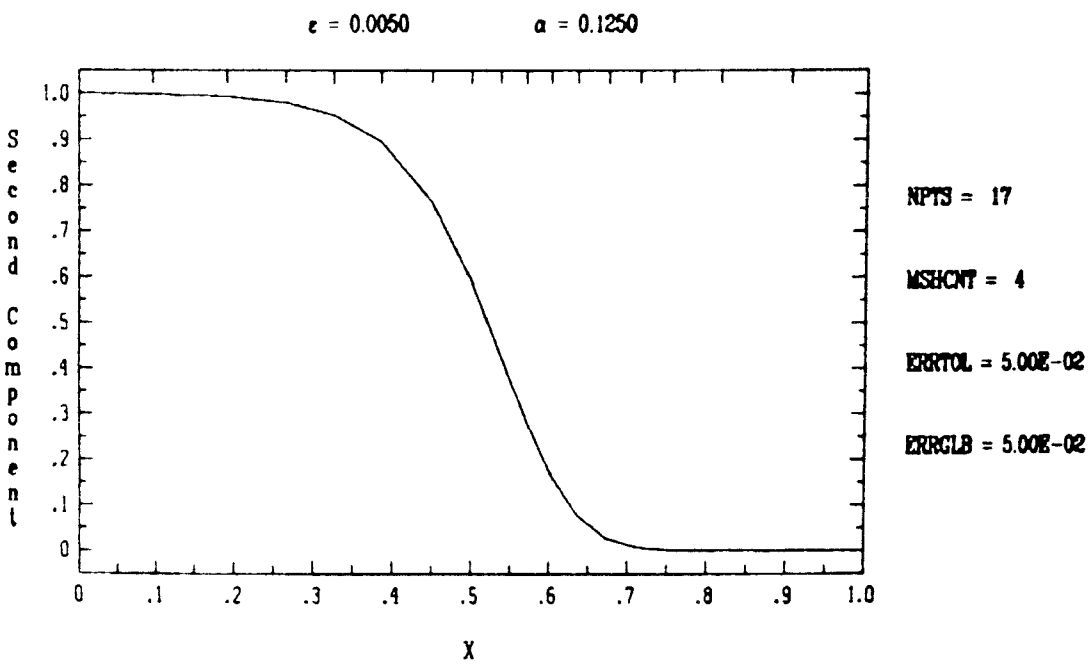

Figure 4.6b. The solution v of $u'' = 1 - v$, $\varepsilon v'' + (vu')' = 0$, $u(0) = 0$, $u(1) = \alpha$, $v(0) = 1$, $v(1) = 0$.

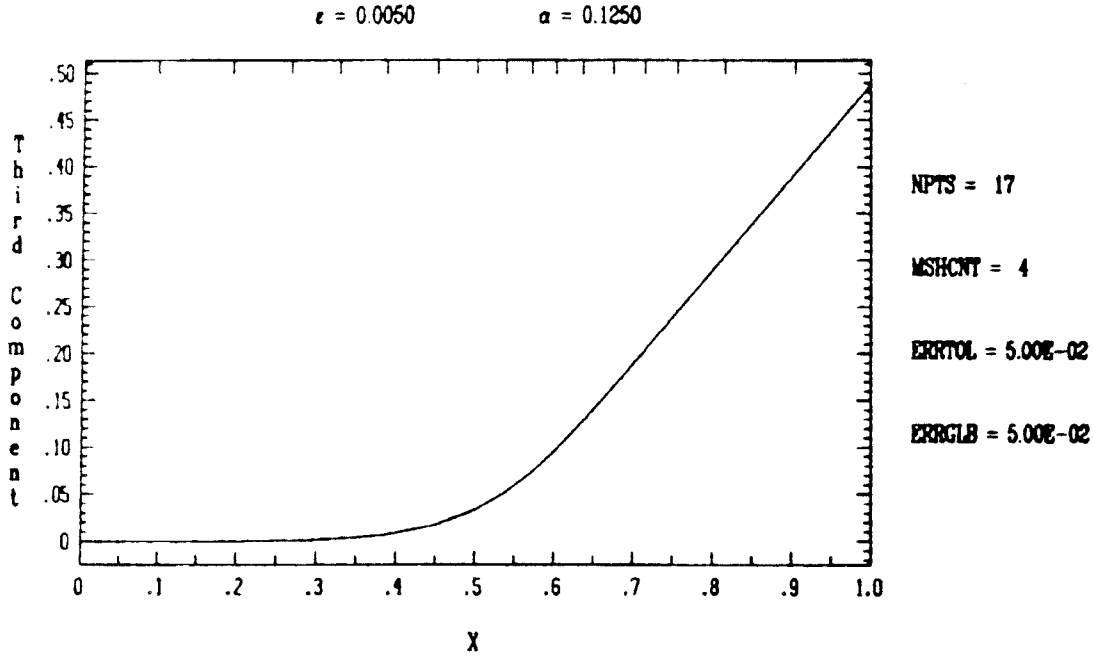

Figure 4.6c. Derivative of solution u in fig. 4.6a

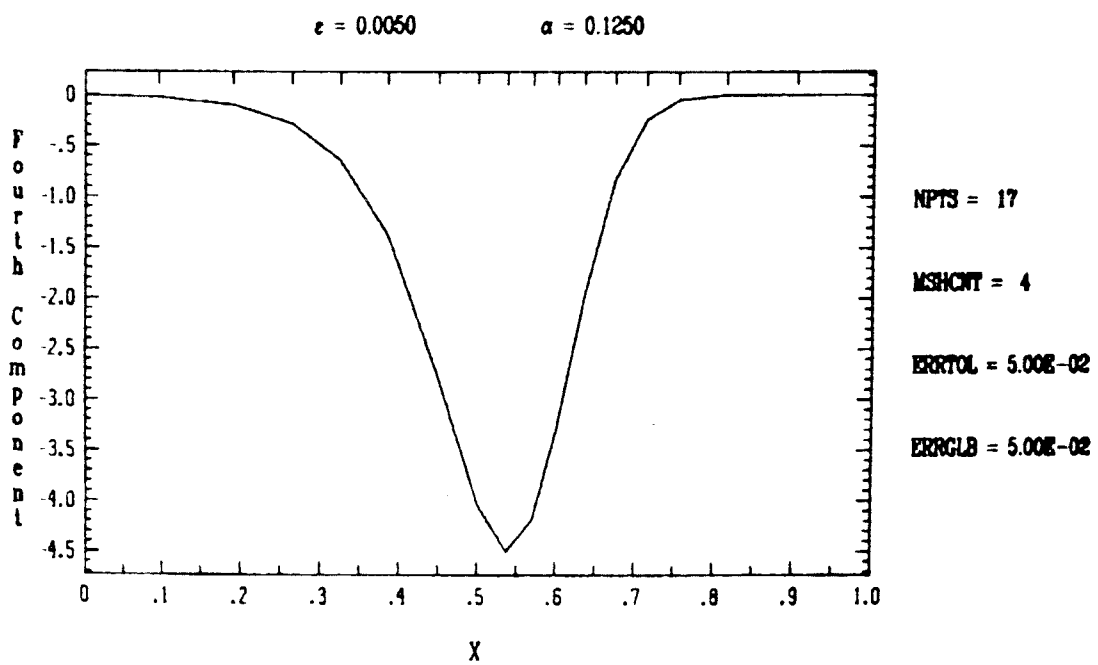

Figure 4.6d. Derivative of solution v in fig. 4.6b

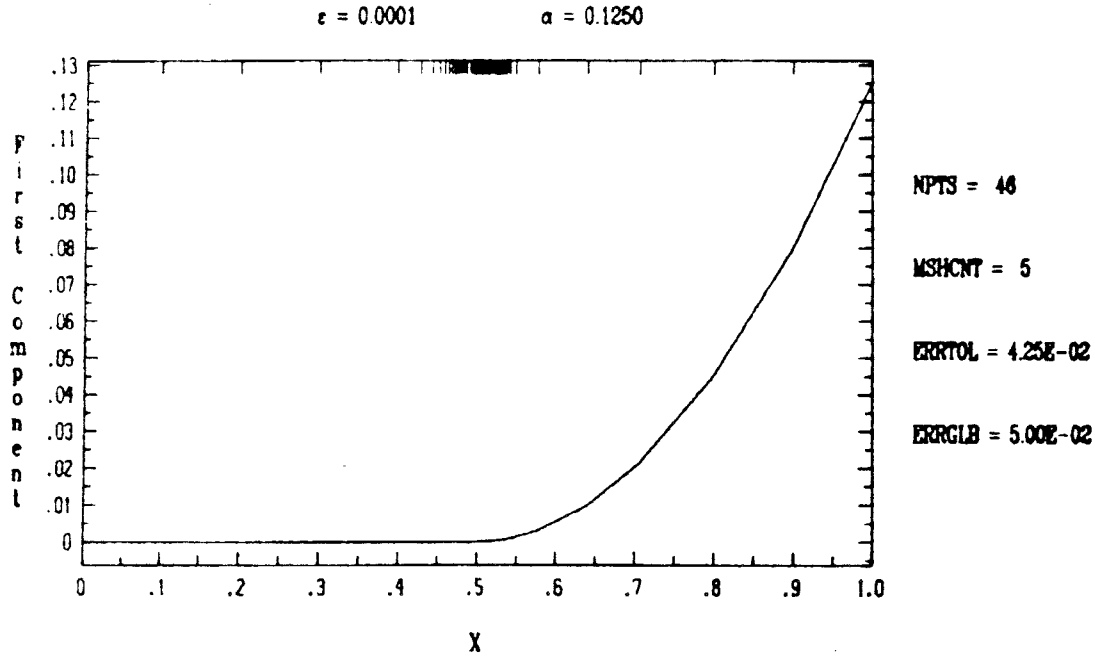

Figure 4.7a. The solution u of $u'' = 1 - v$, $\varepsilon v'' + (vu')' = 0$, $u(0) = 0$, $u(1) = \alpha$, $v(0) = 1$, $v(1) = 0$.

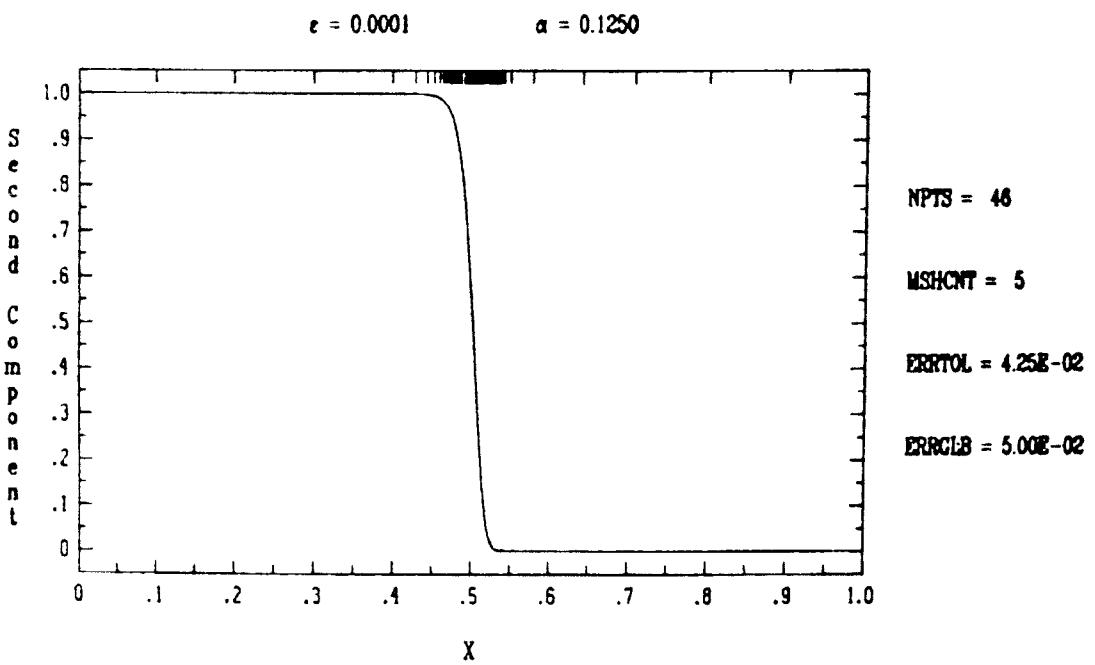

Figure 4.7b. The solution v of $u'' = 1 - v$, $\varepsilon v'' + (vu')' = 0$, $u(0) = 0$, $u(1) = \alpha$, $v(0) = 1$, $v(1) = 0$.

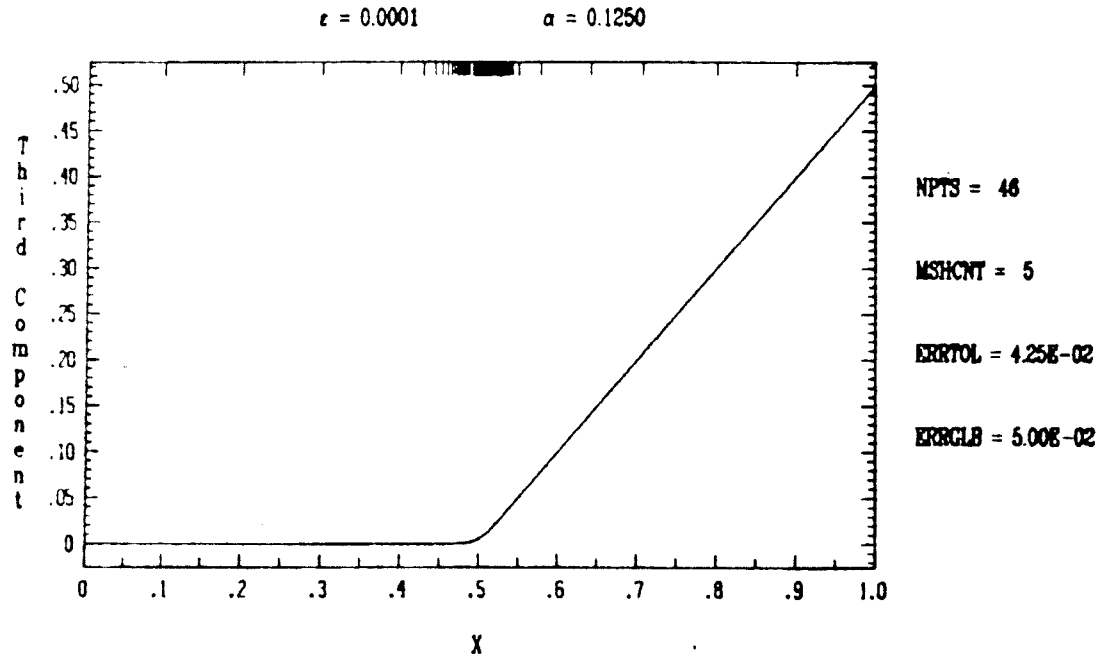

Figure 4.7c. Derivative of solution u in fig. 4.7a

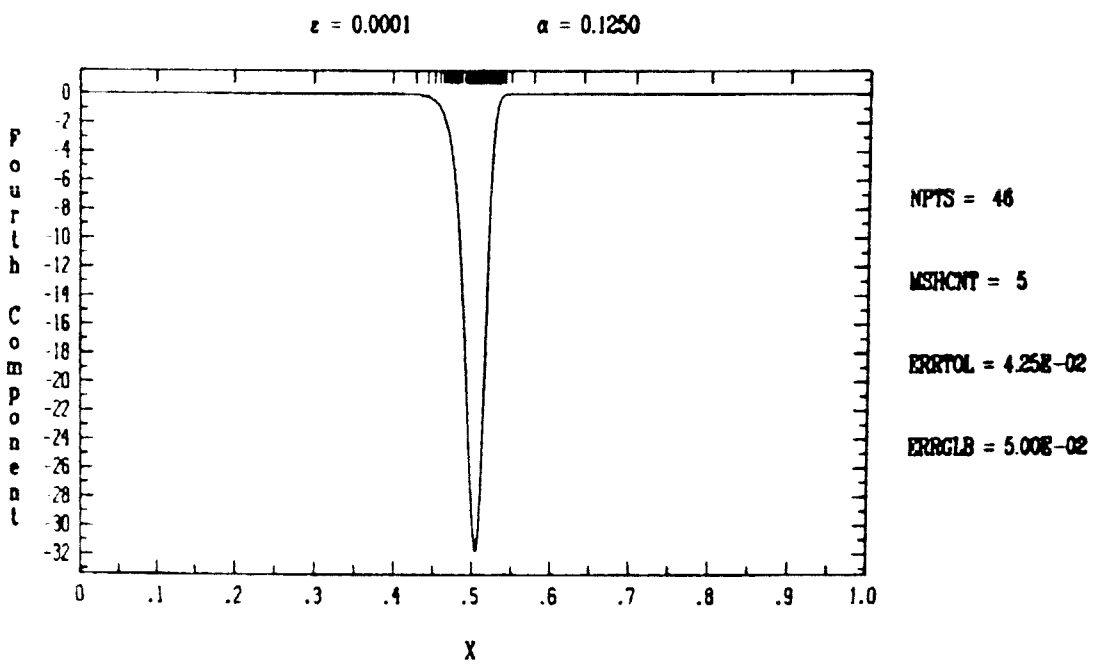

Figure 4.7d. Derivative of solution v in fig. 4.7b

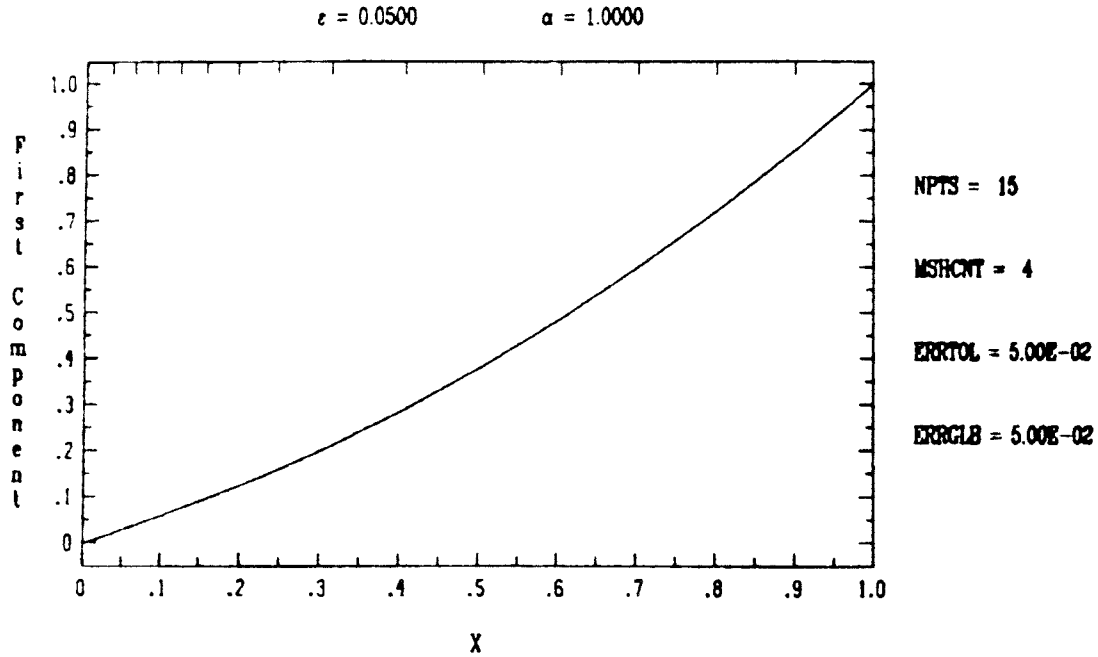

Figure 4.8a. The solution u of $u'' = 1 - v$, $\varepsilon v'' + (vu')' = 0$, $u(0) = 0$, $u(1) = \alpha$, $v(0) = 1$, $v(1) = 0$.

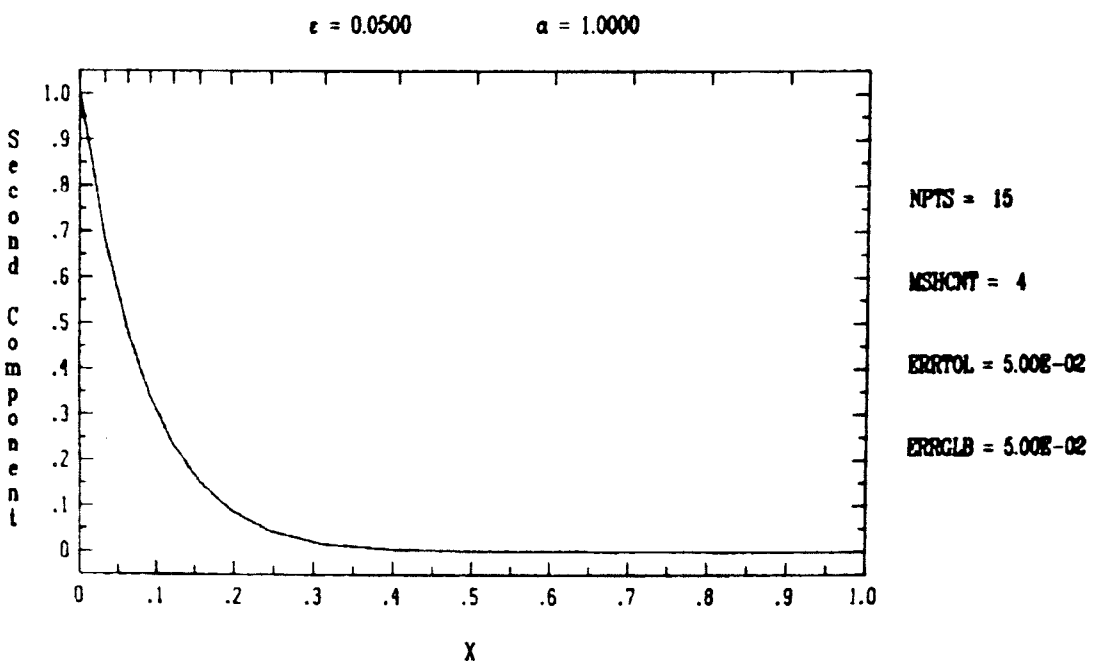

Figure 4.8b. The solution v of $u'' = 1 - v$, $\varepsilon v'' + (vu')' = 0$, $u(0) = 0$, $u(1) = \alpha$, $v(0) = 1$, $v(1) = 0$.

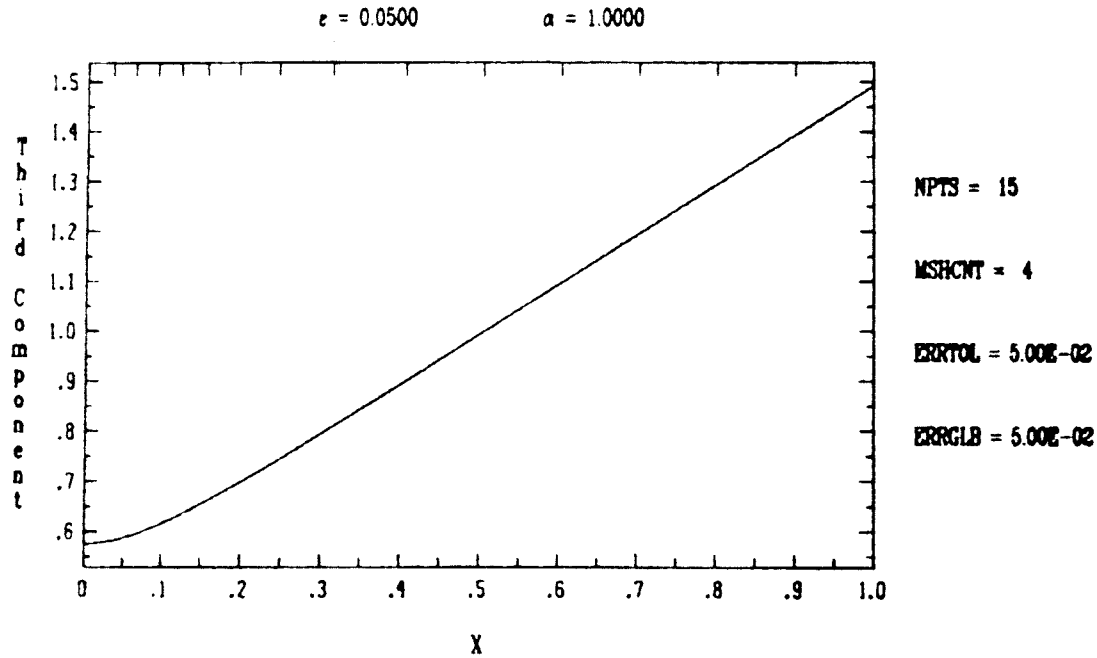

Figure 4.8c. Derivative of solution u in fig. 4.8a

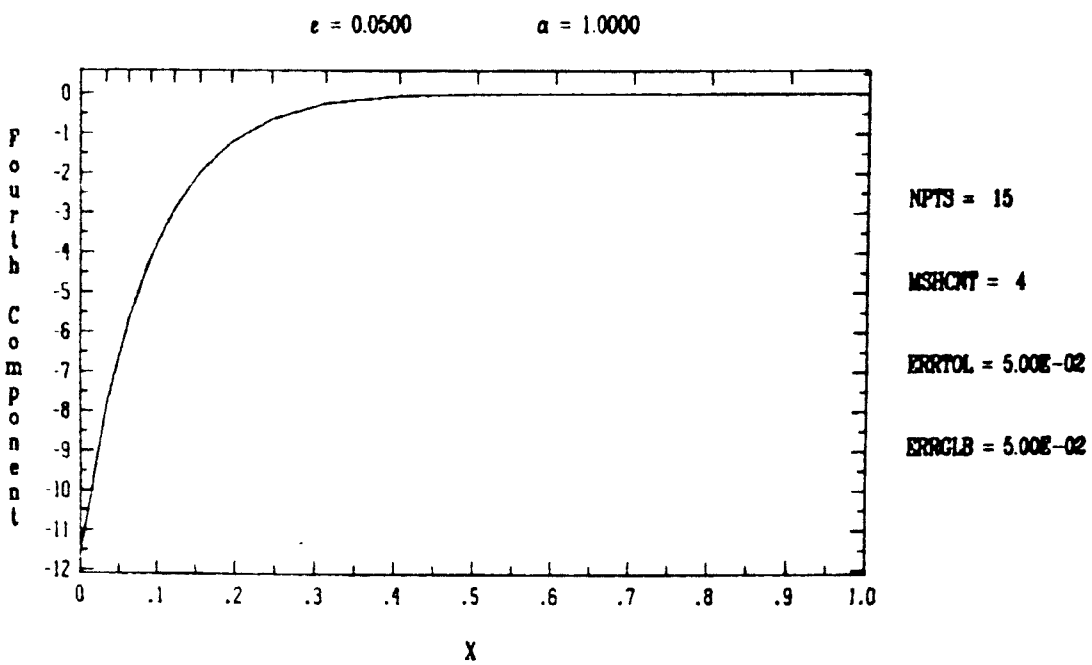

Figure 4.8d. Derivative of solution v in fig. 4.8b

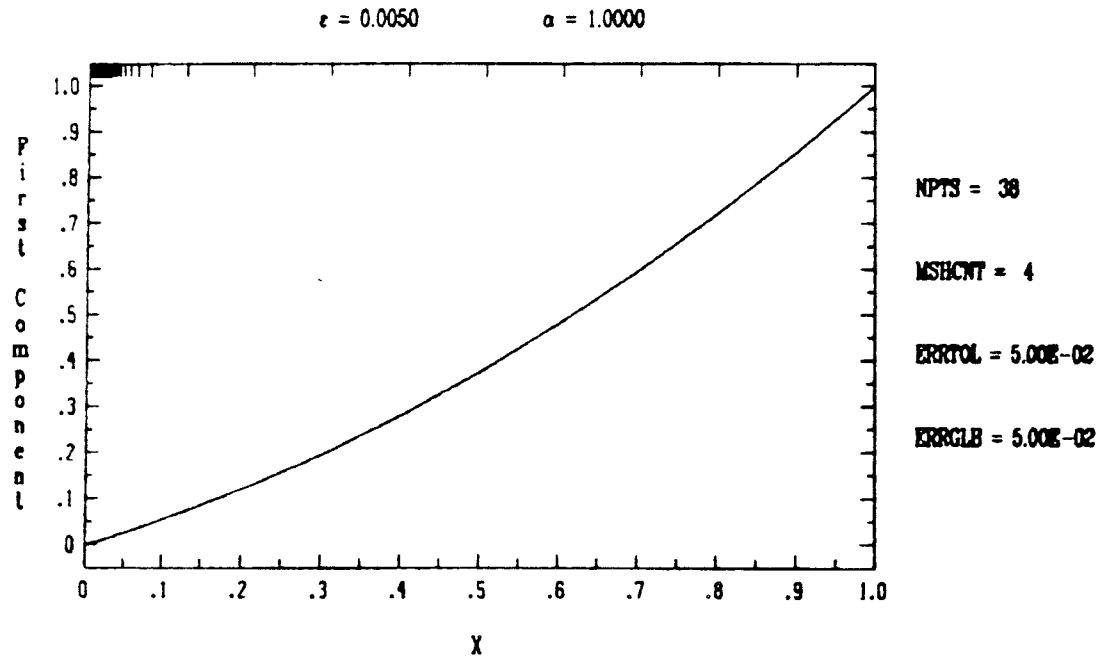

Figure 4.9a. The solution u of $u'' = 1 - v$, $\varepsilon v'' + (vu')' = 0$, $u(0) = 0$, $u(1) = \alpha$, $v(0) = 1$, $v(1) = 0$.

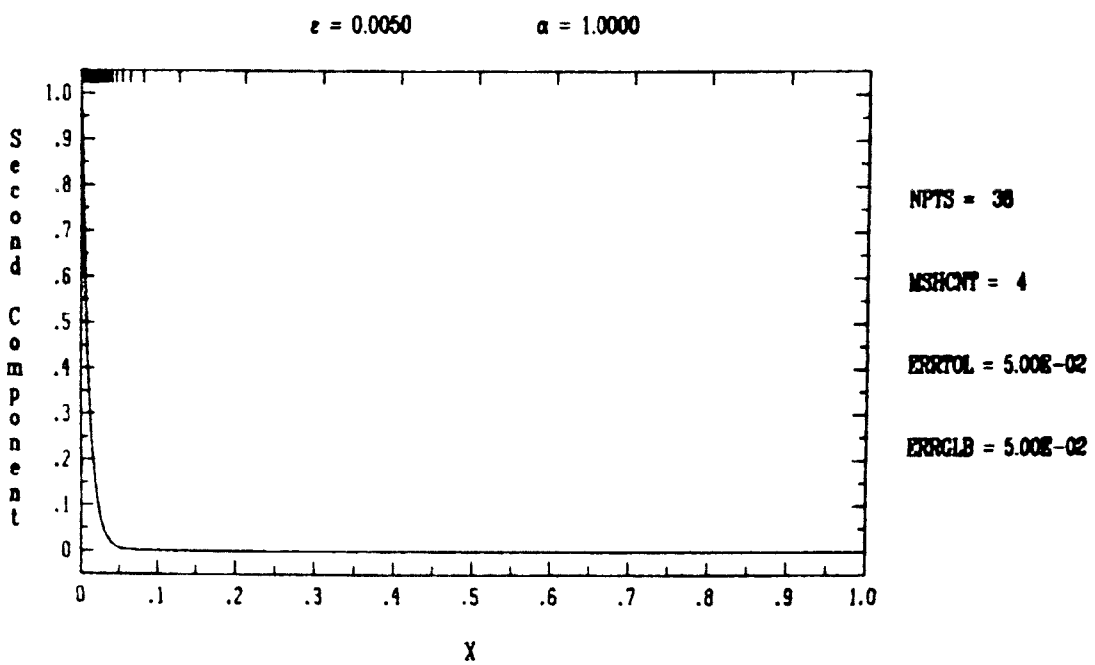

Figure 4.9b. The solution v of $u'' = 1 - v$, $\varepsilon v'' + (vu')' = 0$, $u(0) = 0$, $u(1) = \alpha$, $v(0) = 1$, $v(1) = 0$.

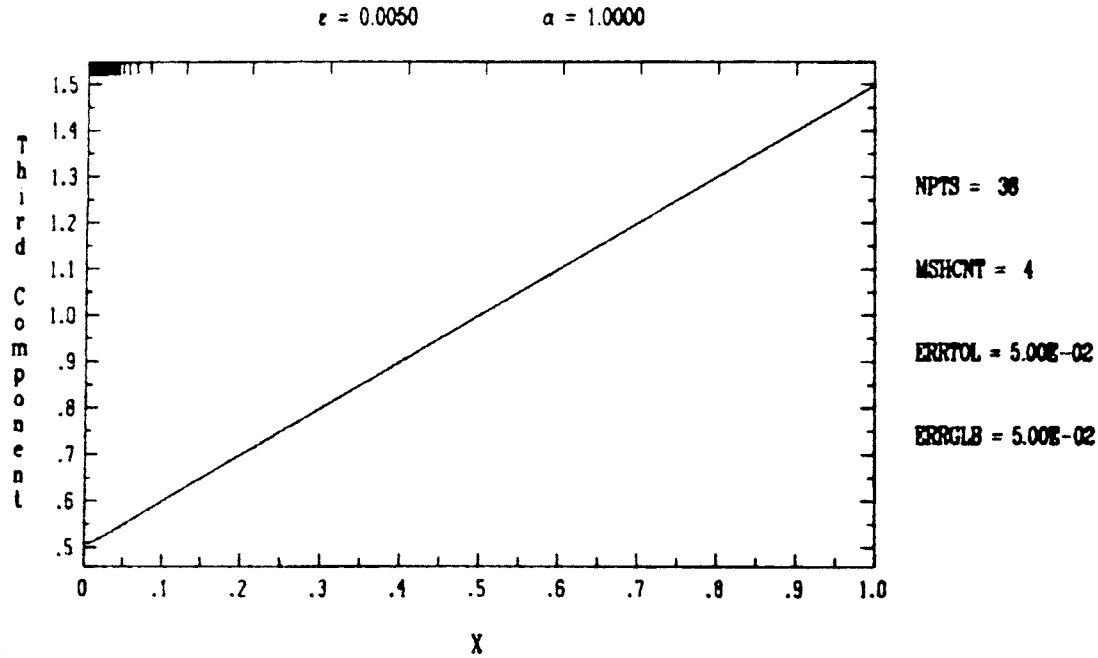

Figure 4.9c. Derivative of solution u in fig. 4.9a

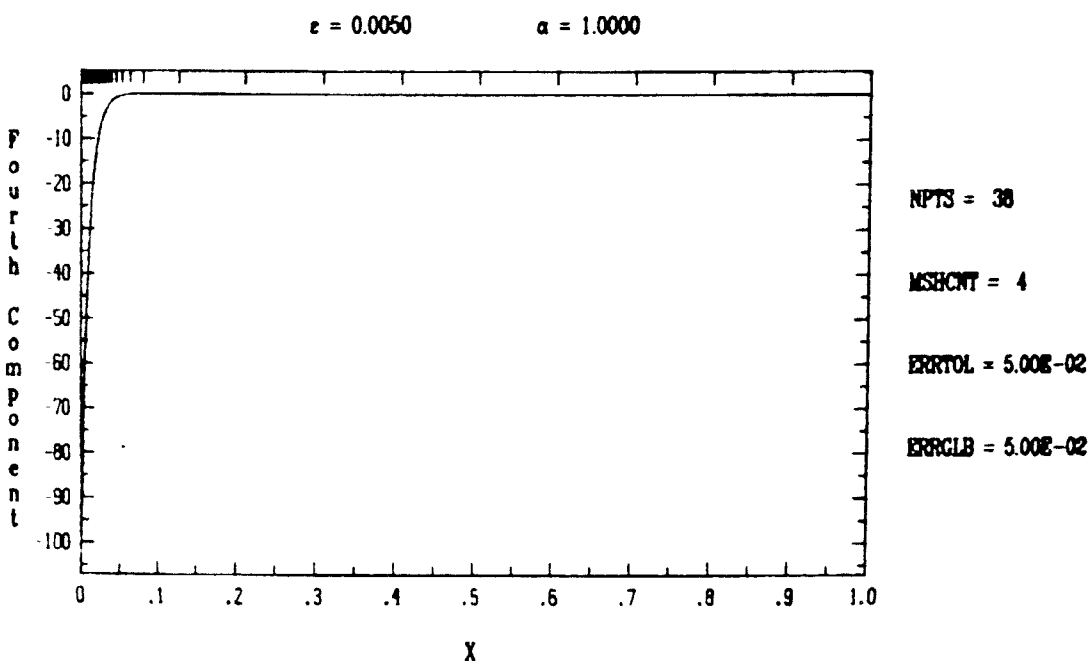

Figure 4.9d. Derivative of solution v in fig. 4.9b

APPENDIX

Rotating Disk Velocity Profiles

Here we present the velocity profiles at R = 625 and γ = 1, 0 and -1 for the flow between two rotating, coaxial disks. There are 47 solutions at these three values of γ.

The solutions are ordered first according to the solution sheet on which they are found. The solutions on each sheet are then divided into groups depending on their γ value. Finally, solutions for the same value of γ are ordered top to bottom as they appear in the figures in Chapter 2.

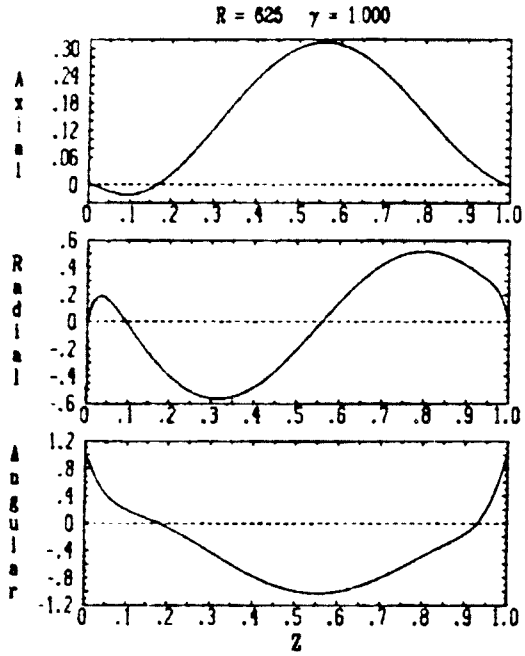

Figure A1.1. Velocity profiles for sheet one, top of fold C.

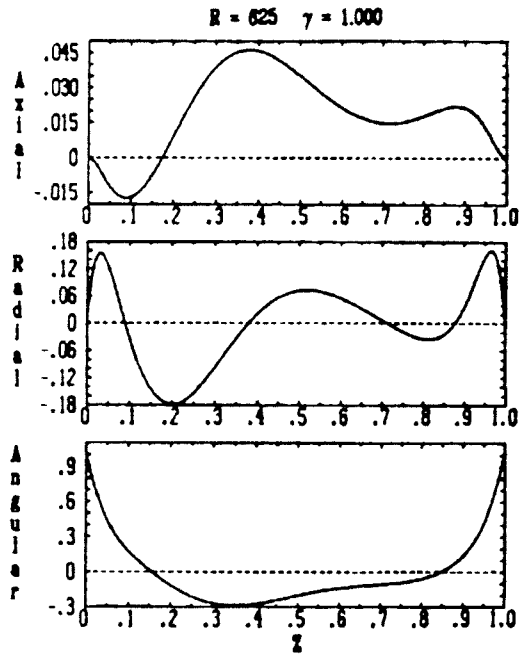

Figure A1.2. Velocity profiles for sheet one, bottom of fold C.

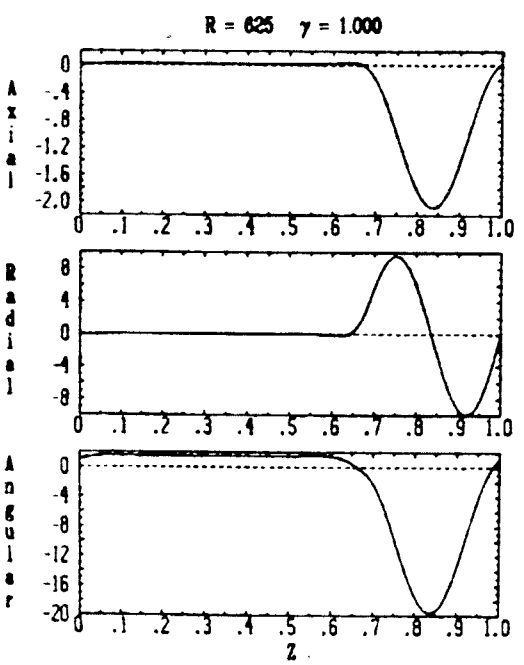

Figure A1.3. Velocity profiles for sheet one, top of fold E.

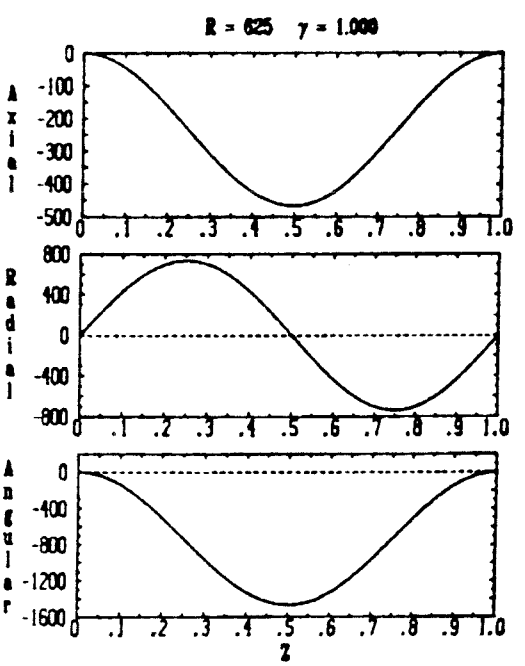

Figure A1.4. Velocity profiles for sheet one, bottom of fold E.

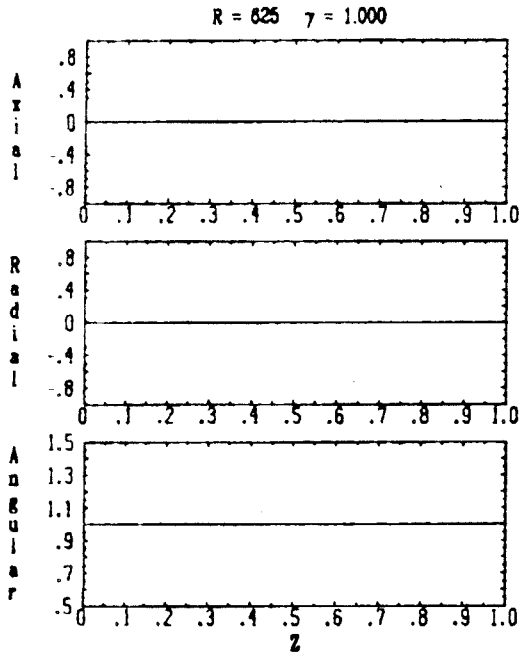

Figure A1.5. Velocity profiles for sheet one, main branch.

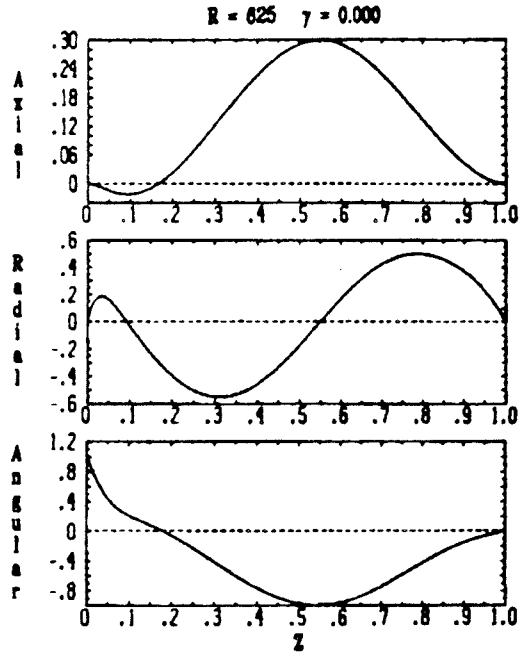

Figure A1.6. Velocity profiles for sheet one, top of fold C.

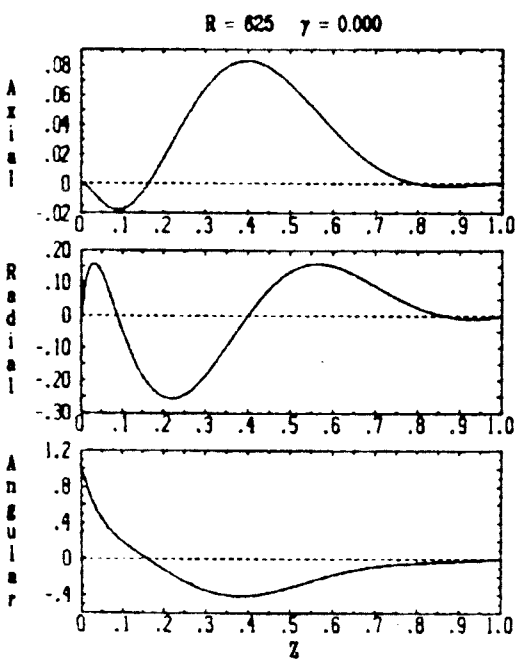

Figure A1.7. Velocity profiles for sheet one, bottom of fold C.

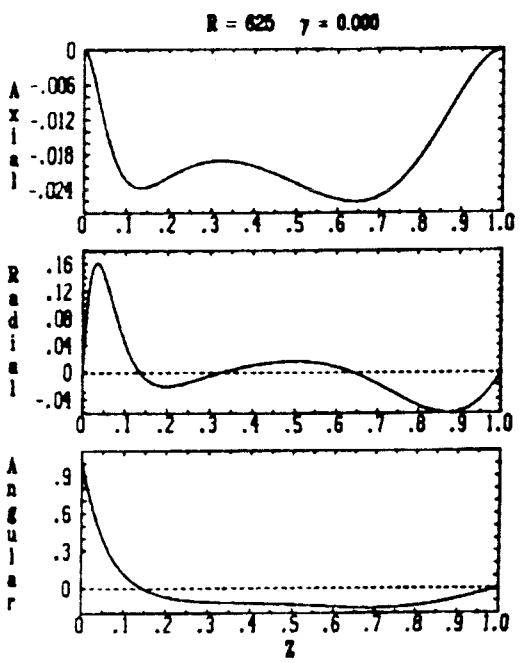

Figure A1.8. Velocity profiles for sheet one, top of fold E.

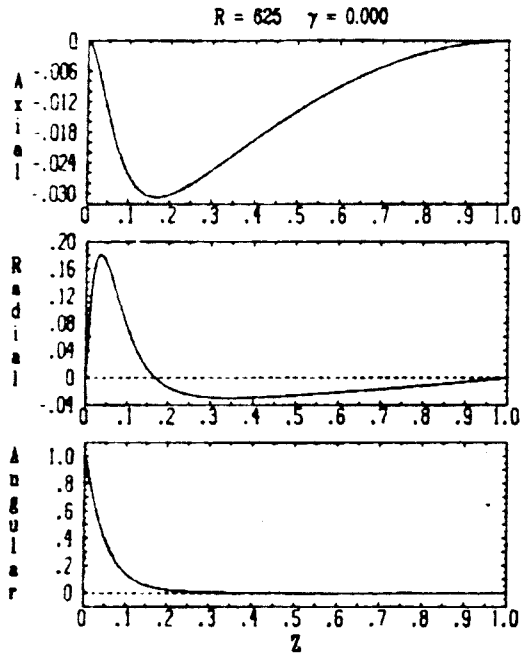

Figure A1.9. Velocity profiles for sheet one, bottom of fold E.

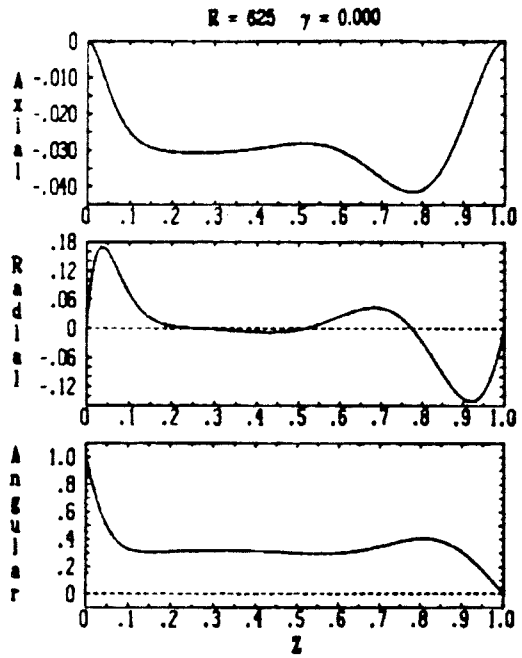

Figure A1.10. Velocity profiles for sheet one, main branch.

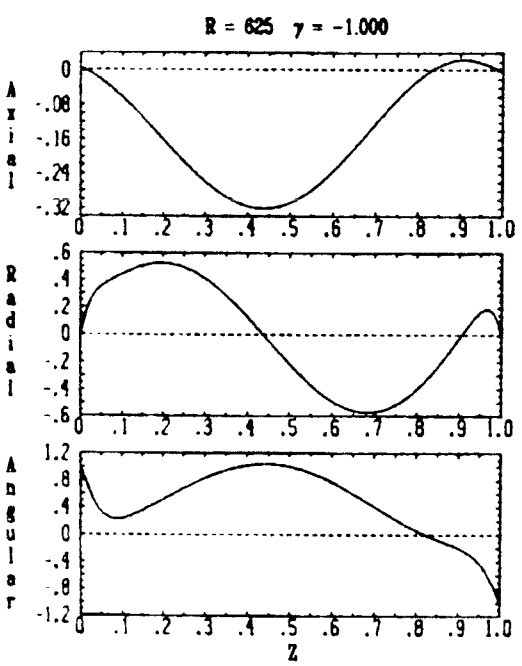

Figure A1.11. Velocity profiles for sheet one, upper bifurcation branch.

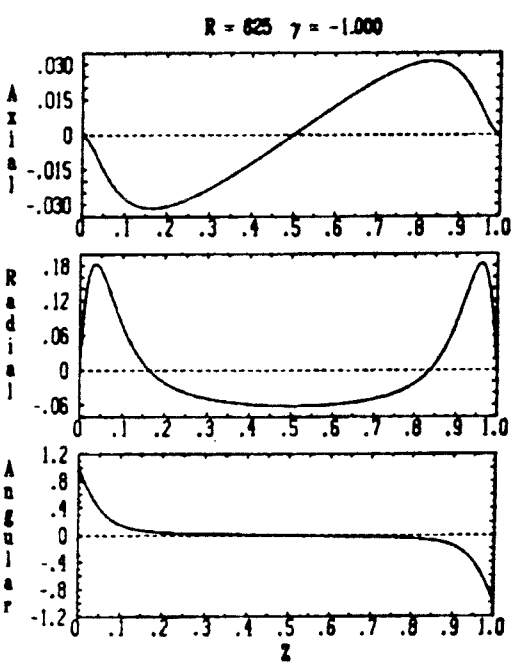

Figure A1.12. Velocity profiles for sheet one, main bifurcation branch.

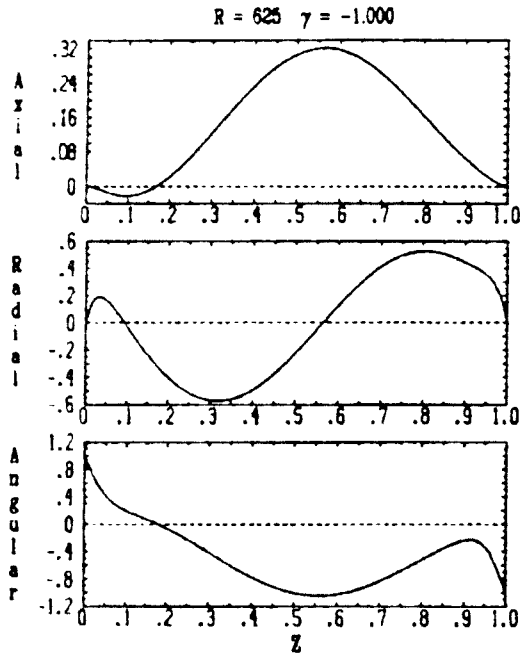

Figure A1.13. Velocity profiles for sheet one, lower bifurcation branch.

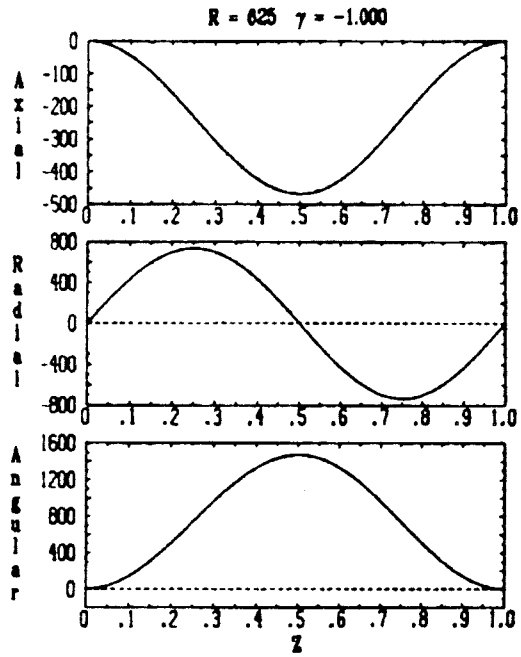

Figure A1.14. Velocity profiles for sheet one, top of fold F.

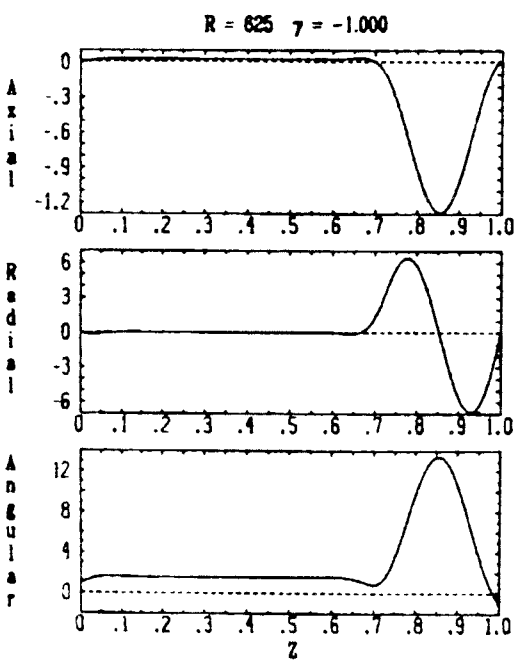

Figure A1.15. Velocity profiles for sheet one, bottom of fold F.

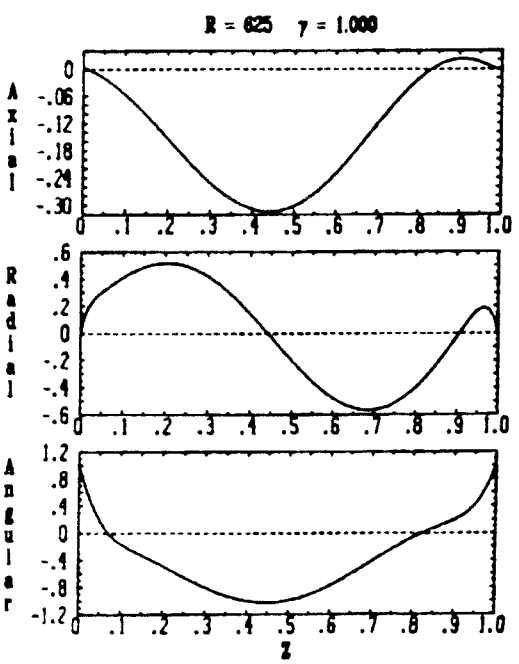

Figure A1.16. Velocity profiles for sheet two, top of fold h.

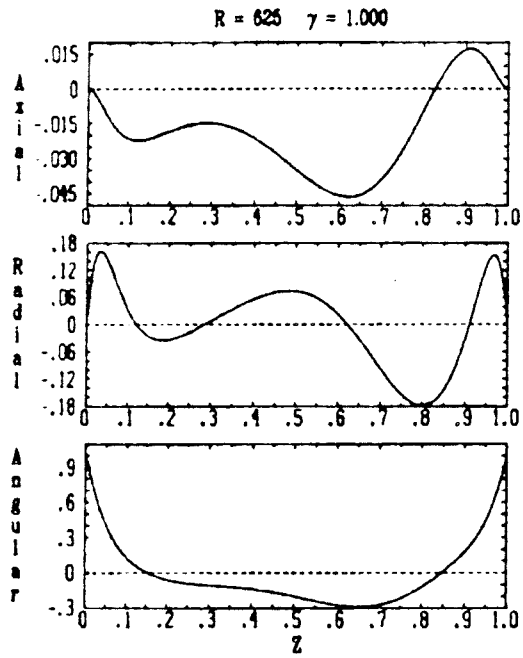

Figure A1.17. Velocity profiles for sheet two, bottom of fold h.

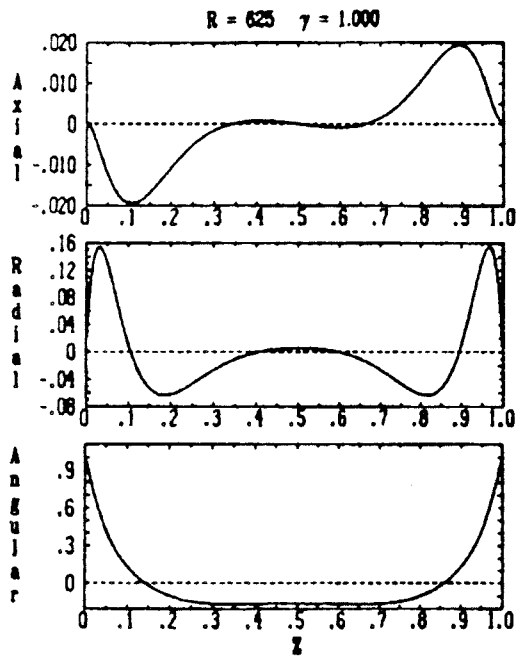

Figure A1.18. Velocity profiles for sheet two, top of fold H.

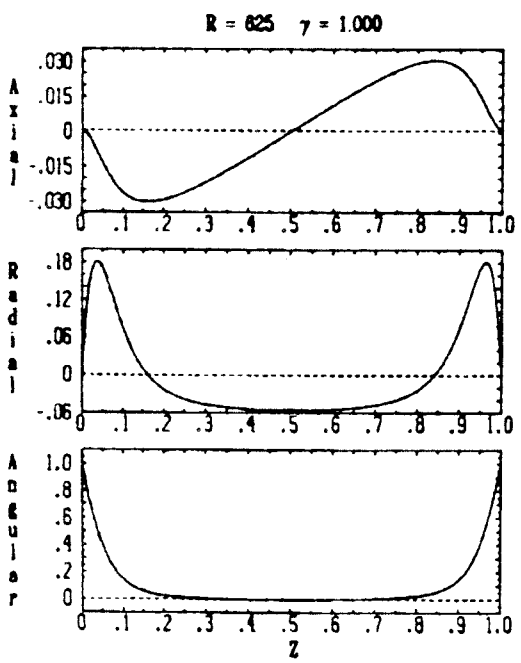

Figure A1.19. Velocity profiles for sheet two, bottom of fold H.

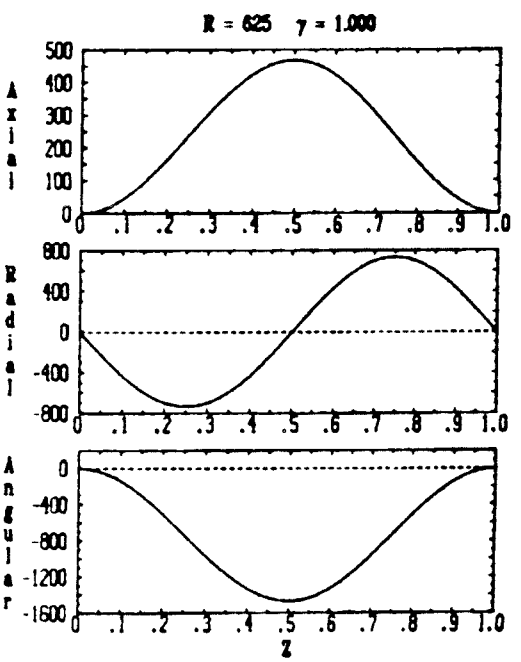

Figure A1.20. Velocity profiles for sheet three, top of fold G.

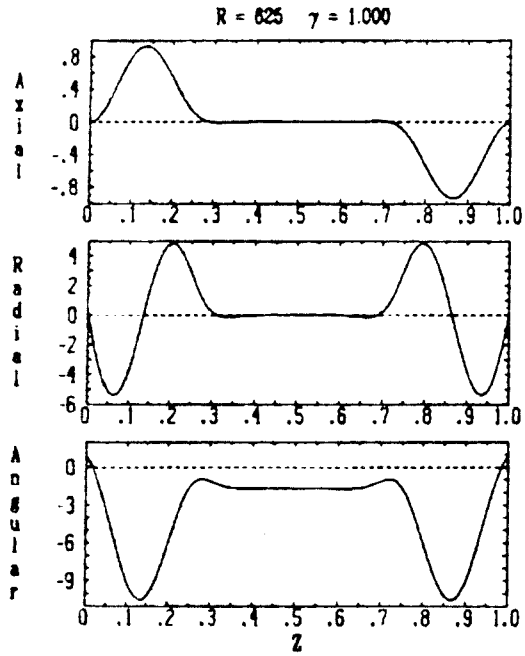

Figure A1.21. Velocity profiles for sheet three, top of fold I.

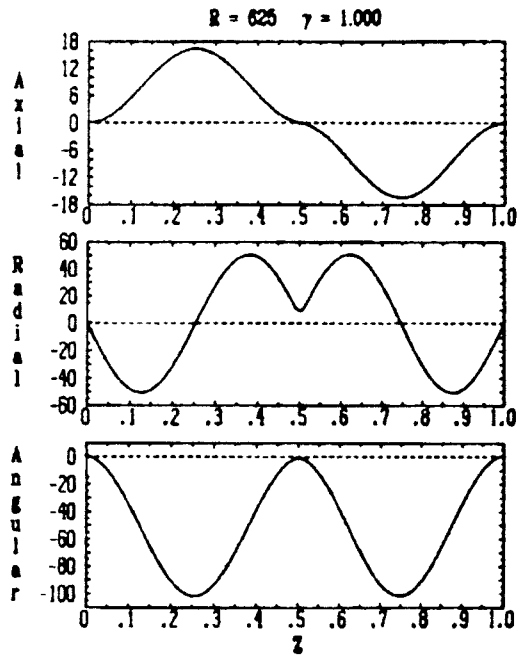

Figure A1.22. Velocity profiles for sheet three, bottom of fold I.

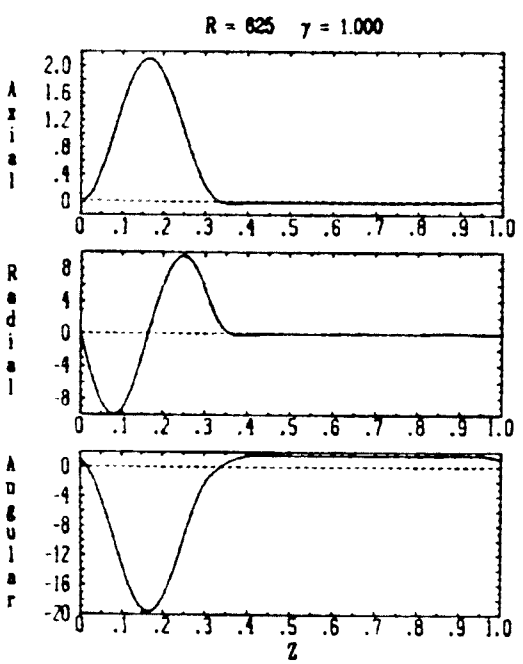

Figure A1.23. Velocity profiles for sheet three, bottom of fold G.

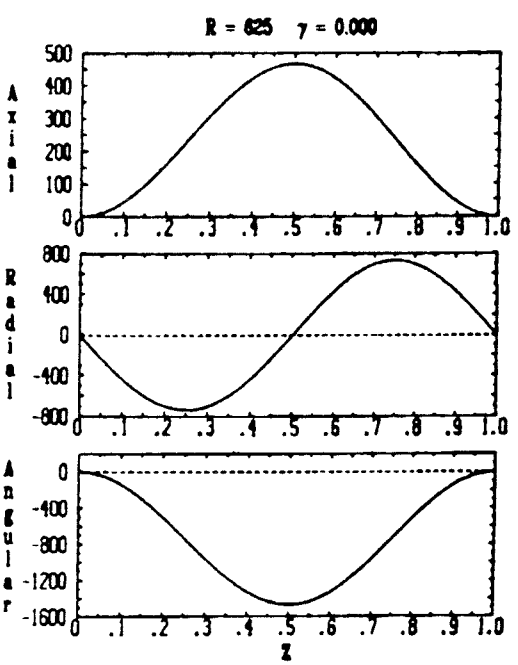

Figure A1.24. Velocity profiles for sheet three, top of fold G.

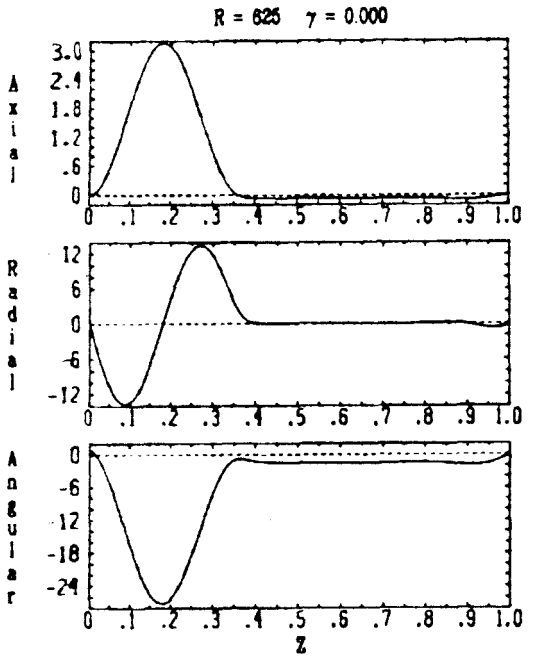

Figure A1.25. Velocity profiles for sheet three, top of fold I.

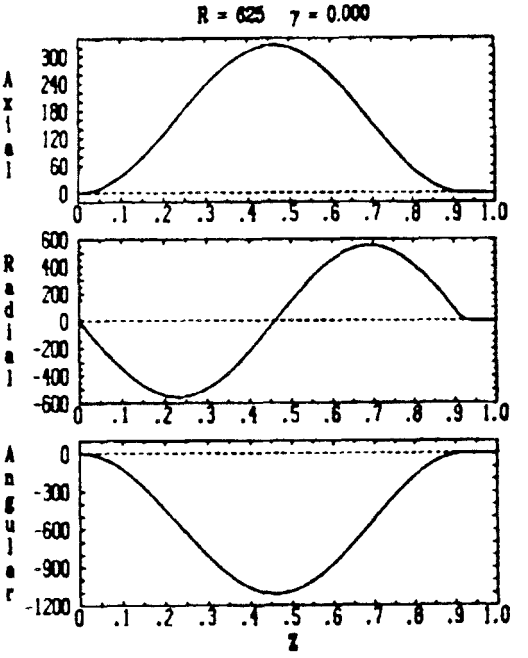

Figure A1.26. Velocity profiles for sheet three, top of fold L.

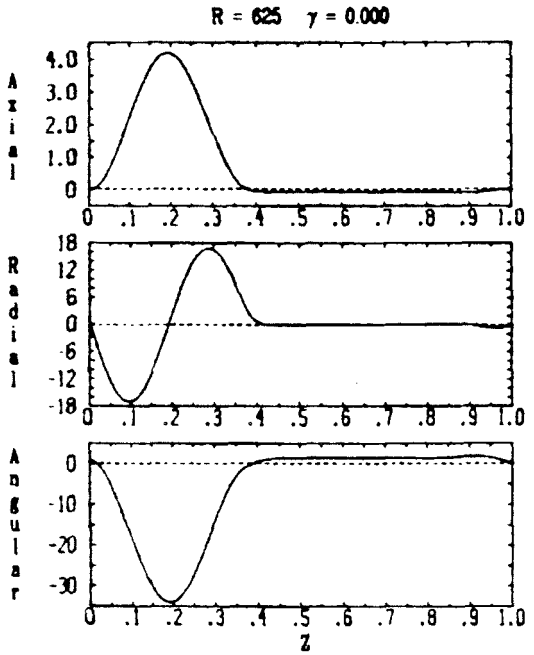

Figure A1.27. Velocity profiles for sheet three, bottom of fold L.

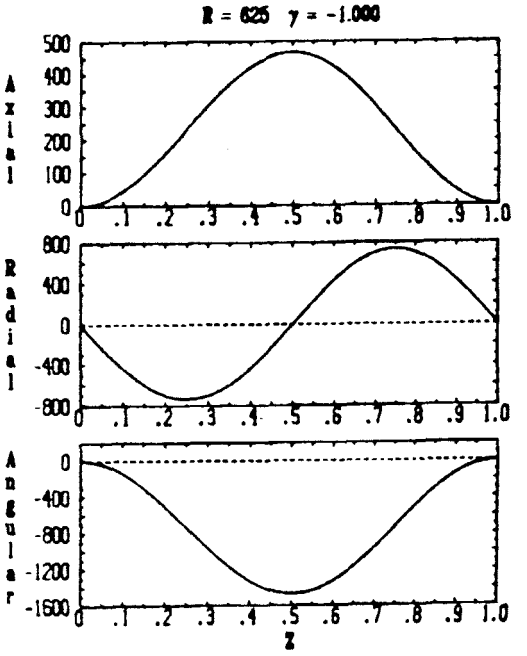

Figure A1.28. Velocity profiles for sheet three, top of fold G.

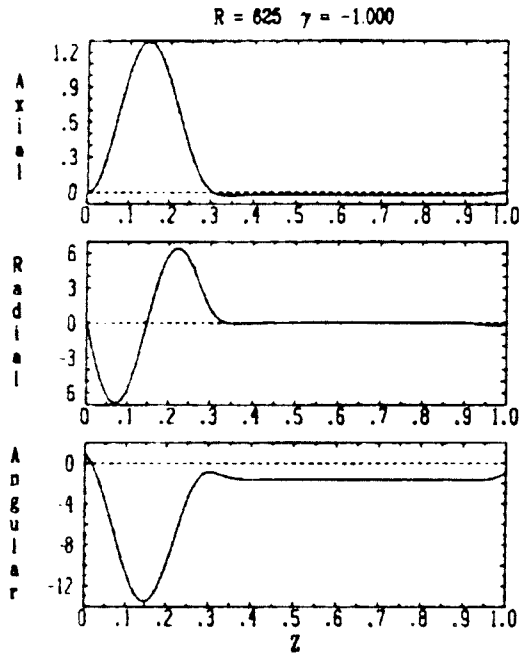

Figure A1.29. Velocity profiles for sheet three, bottom of fold G.

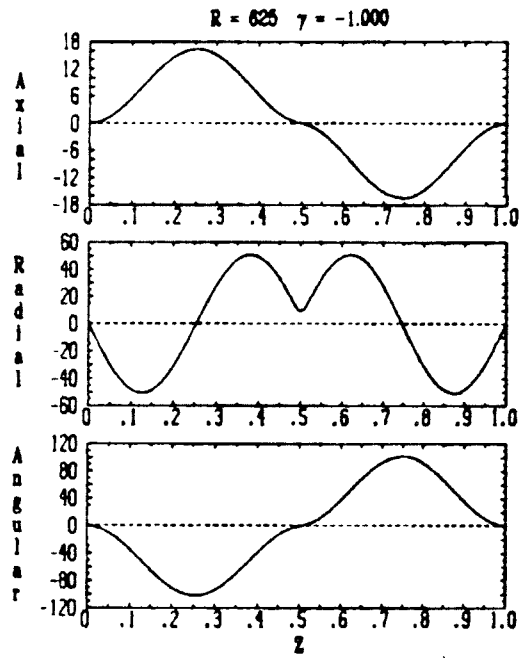

Figure A1.30. Velocity profiles for sheet three, top of fold L.

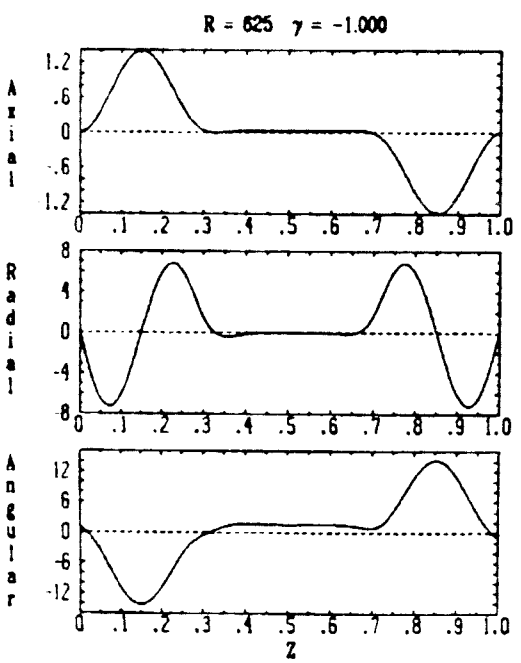

Figure A1.31. Velocity profiles for sheet three, top of fold N.

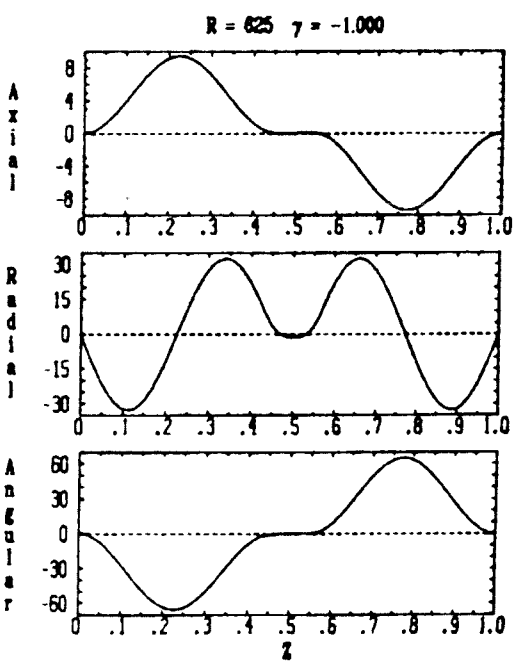

Figure A1.32. Velocity profiles for sheet three, bottom of fold L.

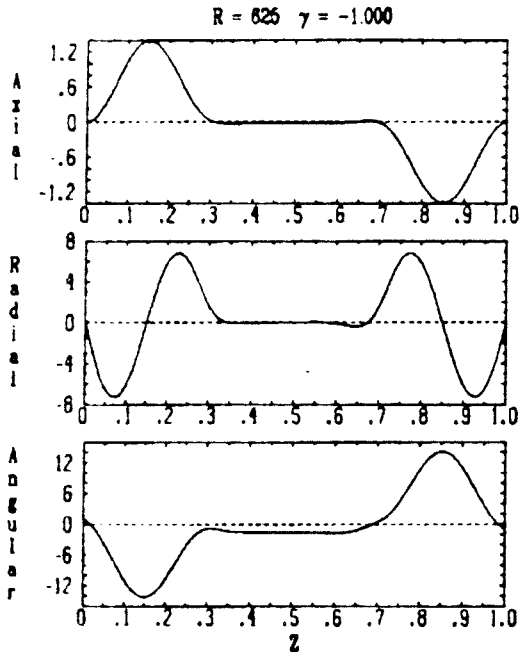

Figure A1.33. Velocity profiles for sheet three, bottom of fold M.

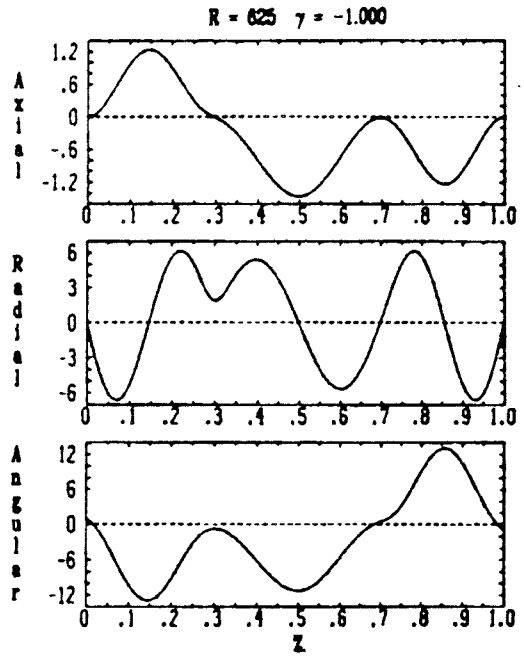

Figure A1.34. Velocity profiles for sheet three, top of fold P.

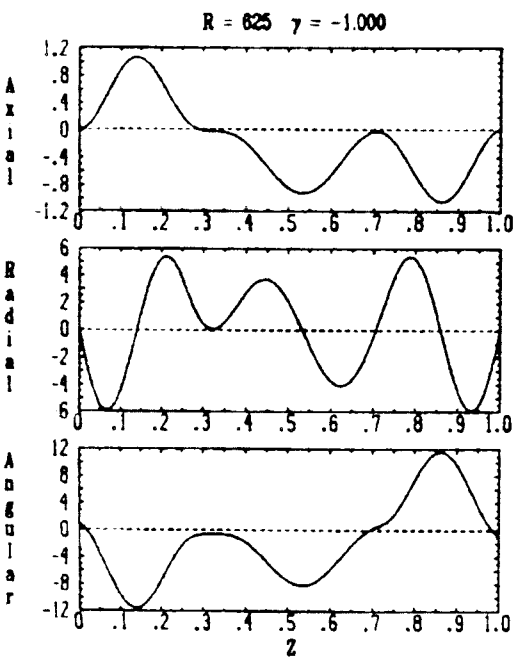

Figure A1.35. Velocity profiles for sheet three, bottom of fold P.

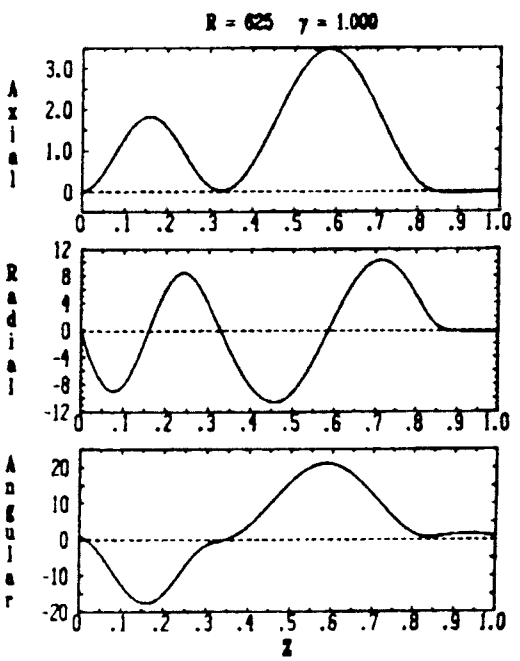

Figure A1.36. Velocity profiles for sheet four, top of fold R.

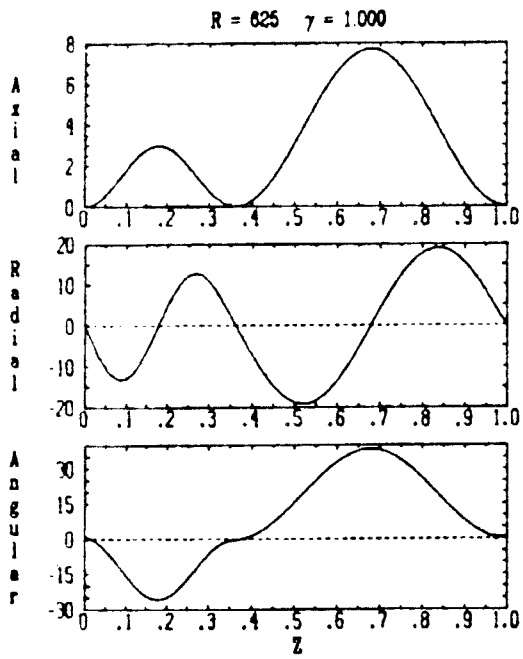

Figure A1.37. Velocity profiles for sheet four, bottom of fold X.

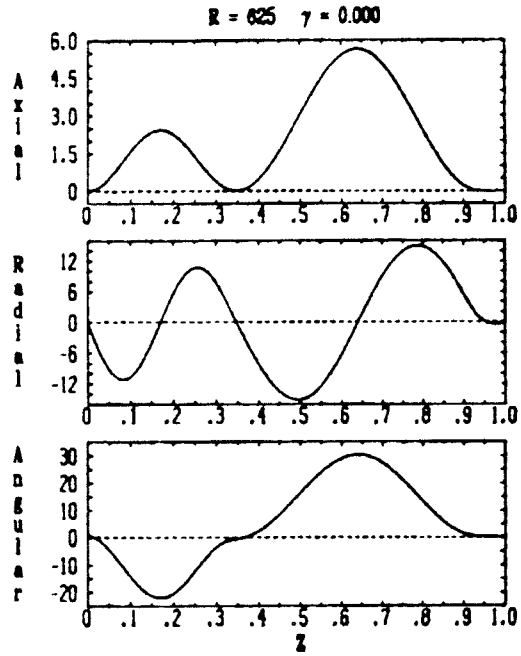

Figure A1.38. Velocity profiles for sheet four, top of fold X.

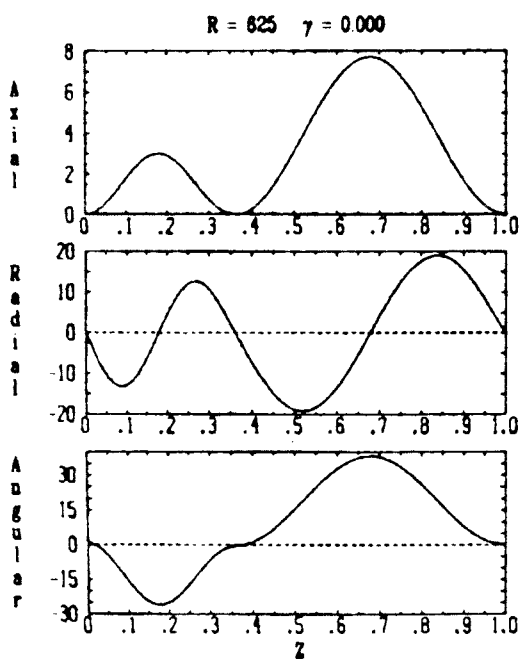

Figure A1.39. Velocity profiles for sheet four, bottom of fold X.

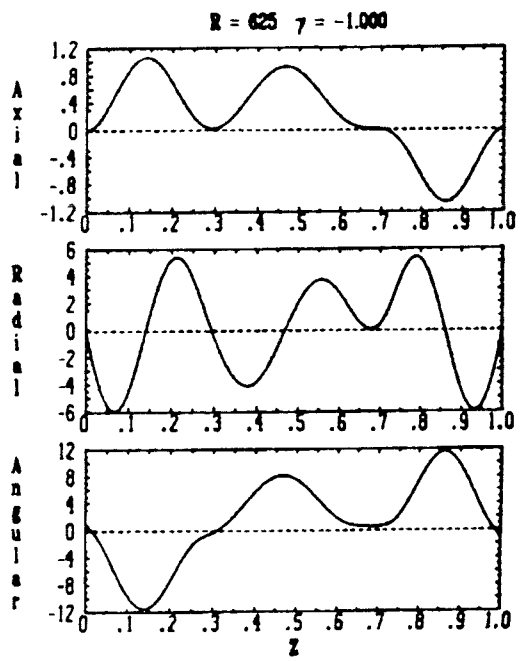

Figure A1.40. Velocity profiles for sheet four, top of fold R.

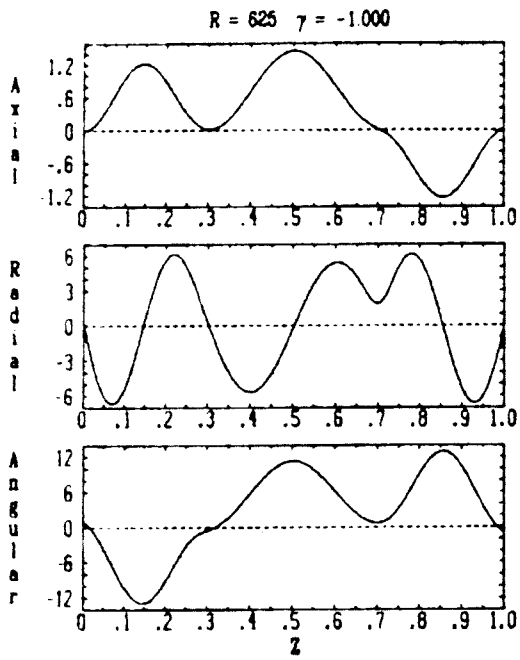

Figure A1.41. Velocity profiles for sheet four, bottom of fold R.

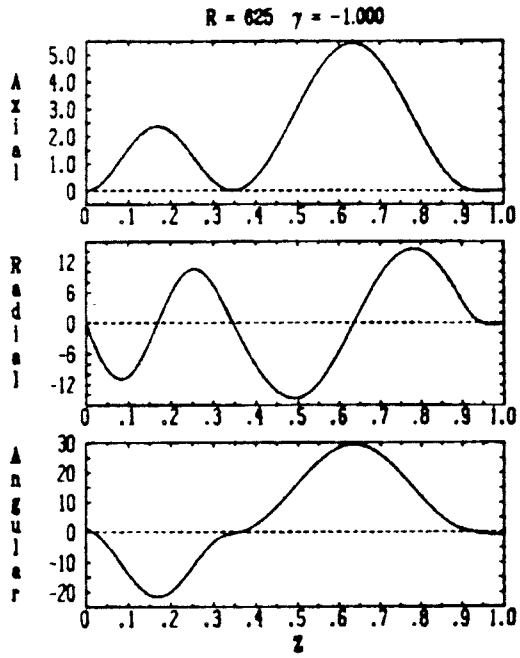

Figure A1.42. Velocity profiles for sheet four, top of fold X.

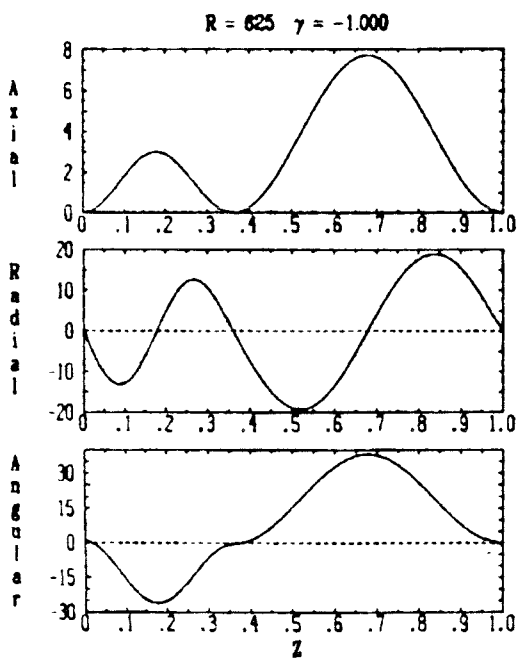

Figure A1.43. Velocity profiles for sheet four, bottom of fold X.

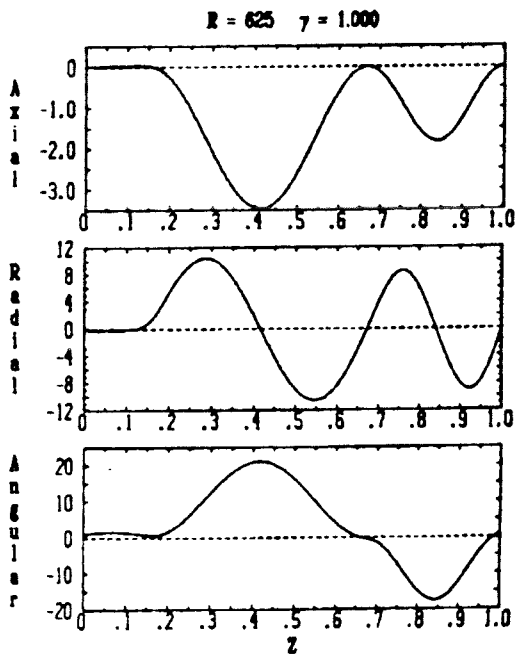

Figure A1.44. Velocity profiles for sheet five, top of fold U.

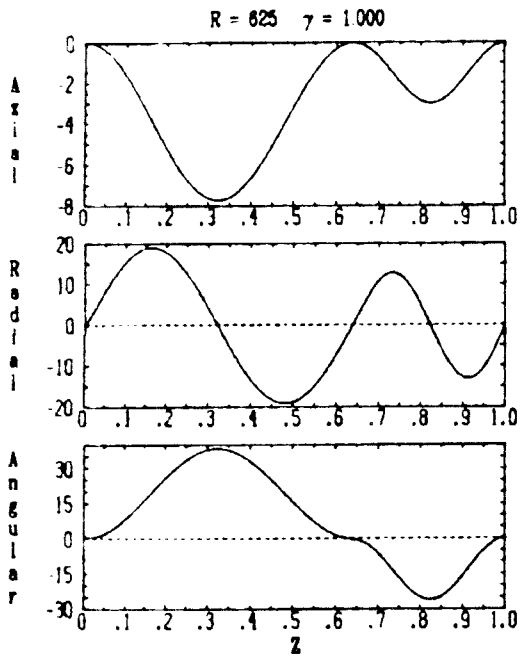

Figure A1.45. Velocity profiles for sheet five, bottom of fold V.

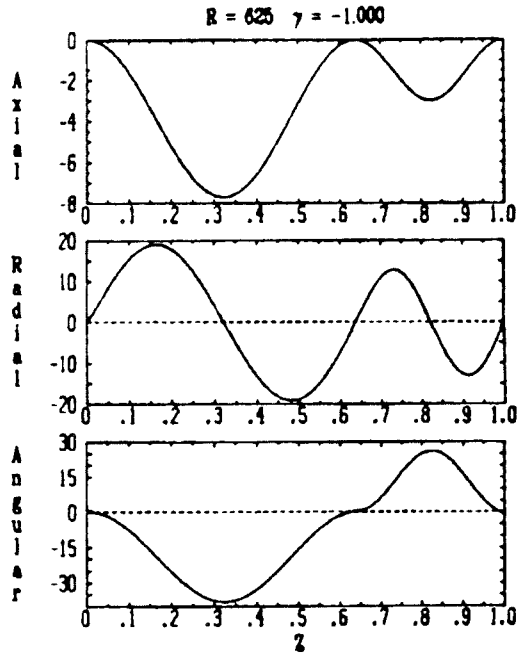

Figure A1.46. Velocity profiles for sheet six, top of fold Y.

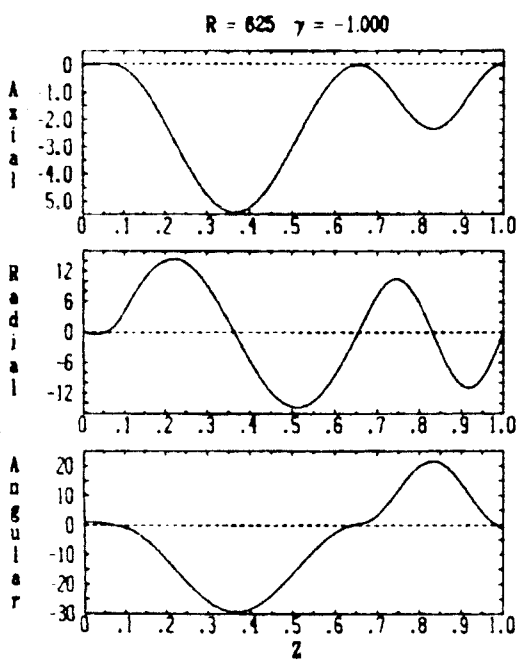

Figure A1.47. Velocity profiles for sheet six, top of fold Y.

References

[1] G. K. Batchelor, *Note on a Class of the Navier-Stokes Equations Representing Steady Rotationally-Symmetric Flow*, Quart. J. Mech. Appl. Math., **4** (1951), pp. 29–41.

[2] G. Bratu, *Sur Les Équations Intégrales Non Linéaires*, Bulletin de la Société Mathématique de France, **42** (1914), pp. 113–142.

[3] F. Brezzi, *Private Communication*, (1984).

[4] T. F. Chan, *Deflation Techniques and Block-Elimination Algorithms for Solving Bordered Singular Systems*, SIAM J. Stat. Comput., **5** (1984), pp. 121–134.

[5] P. Collet, J.-P. Eckmann and H. Koch, *Period Doubling Bifurcations for Families of Maps on* $\mathbb{R}^n$, J. Statist. Phys., **25** (1981) pp. 1–14.

[6] C. de Boor, *Good Approximation by Splines with Variable Knots. II*, in *Lecture Notes in Mathematics, No. 363*, Springer-Verlag, Berlin, 1973, pp. 12–20.

[7] J. J. Dongarra, J. R. Bunch, C. B. Moler and G. W. Stewart, *LINPACK User's Guide*, SIAM, Philadelphia, 1979.

[8] I. M. Gel´fand, *Some Problems in the Theory of Quasilinear Equations*, Usephi Mat. Nauk (N.S.) **14** (1959) No. 2, pp. 89-158. English translation in Translations of the AMS, Series 2, **29** (1963), pp. 295–381.

[9] W. B. Gragg, *On Extrapolation Algorithms for Ordinary Initial Value Problems*, SIAM J. Numer. Anal., Series B, **2** (1965), pp. 384–403.

[10] M. Holodniok, M. Kubíček and V. Hlaváček, *Computation of the Flow Between Two Rotating Coaxial Disks*, J. Fluid Mech., **81** (1977), pp. 689–699.

[11] M. Holodniok, M. Kubíček and V. Hlaváček, *Computation of the Flow Between Two Rotating Coaxial Disks: Multiplicity of Steady-State Solutions*, J. Fluid Mech., **108** (1981), pp. 227–240.

[12] A. Jepson and A. Spence, *Folds in Solutions of Two Parameter Systems and their Calculation: Part I*, to appear in SIAM J. Numer. Anal.

[13] D. Joseph and T. Lundgren, *Quasilinear Dirichlet Problems Driven by Positive Sources*, Arch. Rat. Mech. Anal., **49** (1973), pp. 241–269.

[14] J. P. Keener and H. B. Keller, *Perturbed Bifurcation Theory*, Arch. Rat. Mech. Anal., **50** (1973), pp. 159–175.

[15] H. B. Keller, *Accurate Difference Methods for Linear Ordinary Differential Systems Subject to Linear Constraints*, SIAM J. Numer. Anal., **6** (1969), pp. 8–30.

[16] H. B. Keller, *Accurate Difference Methods for Nonlinear Two-Point Boundary Value Problems*, SIAM J. Numer. Anal., **11** (1974), pp. 305–320.

[17] H. B. Keller, *Numerical Solution Of Bifurcation and Nonlinear Eigenvalue Problems*, in *Applications of Bifurcation Theory*, P. Rabinowitz, ed., Academic Press, New York, 1977, pp. 359–384.

[18] H. B. Keller, *Global Homotopies and Newton Methods*, in *Recent Advances in Numerical Analysis*, C. deBoor and G. H. Golub, eds., Academic Press, New York, 1979, pp. 73–94.

[19] H. B. Keller, *Practical Procedures in Path Following Near Limit Points*, in *Computing Methods in Applied Sciences and Engineering*, R. Glowinski and J. L. Lions, eds., North-Holland Publishing Company, Amsterdam, 1982.

[20] H. B. Keller, *The Bordering Algorithm and Path Following Near Singular Points of Higher Nullity*, SIAM J. Sci. Stat. Comput., **4** (1983) pp. 573–582.

[21] H. B. Keller, *Private Communication*, (1983).

[22] H. B. Keller and V. Pereyra, *Difference Methods and Deferred Corrections For Ordinary Boundary Value Problems*, SIAM J. Numer. Anal., **16** (1979), pp. 241–259.

[23] M. A. Kosecoff, *Some Problems in Nonlinear Elasticity*, Thesis, California Institute of Technology, Pasadena, California, 1975.

[24] H.-O. Kreiss, *Introduction to Numerical Analysis*, Caltech Course Lecture Notes, 1979.

[25] H. O. Kreiss and S. V. Parter, *On the Swirling Flow Between Rotating Coaxial Disks, Asymptotic Behaviour, I*, Proc. Roy. Soc. Edinburgh, **90A** (1981), pp. 293–316.

[26] H. O. Kreiss and S. V. Parter, *On the Swirling Flow Between Rotating Coaxial Disks, Asymptotic Behaviour, II*, Proc. Roy. Soc. Edinburgh, **90A** (1981), pp. 317–346.

[27] H. O. Kreiss and S. V. Parter, *On the Swirling Flow Between Rotating Coaxial Disks: Existence and Nonuniqueness*, Comm. Pure Appl. Math., **36** (1983), pp. 55–84.

[28] G. N. Lance and M. H. Rogers, *The Axially Symmetric Flow of a Viscous Fluid Between Two Infinite Rotating Disks*, Proc. Roy. Soc., A **266** (1962), pp. 109–121.

[29] M. Lentini and H. B. Keller, *The von Kármán Swirling Flows*, SIAM J. Appl. Math., **38** (1980), pp. 52–64.

[30] M. Lentini and V. Pereyra, *An Adaptive Finite Difference Solver for Nonlinear Two-Point Boundary Value Problems with Mild Boundary Layers*, SIAM J. Numer. Anal., **14** (1977), pp. 91–111.

[31] E. N. Lorenz, *Deterministic Nonperiodic Flow*, J. Atmos. Sci., **20** (1962) p. 130.

[32] B. J. Matkowsky and W. L. Siegmann, *The Flow Between Counter-Rotating Disks at High Reynolds Number*, SIAM J. Appl. Math., **30** (1976), pp. 720–727.

[33] J. B. McLeod and S. V. Parter, *On the Flow Between Two Counter-Rotating Infinite Plane Disks*, Arch. Rat. Mech. Anal., **54** (1974), pp. 301–327.

[34] G. L. Mellor, P. J. Chapple and V. K. Stokes, *On the Flow Between a Rotating and a Stationary Disk*, J. Fluid Mech., **31** (1968), pp. 95–112.

[35] N. Minorsky, *Nonlinear Oscillations*, Robert E. Krieger Publishing Co., Huntington, New York, 1974.

[36] G. Moore and A. Spence, *The Calculation of Turning Points of Nonlinear Equations*, SIAM J. Numer. Anal., **17** (1980) pp. 567–576.

[37] Nguyen, Ribault and Florent, *Multiple Solutions For Flow Between Coaxial Disks*, J. Fluid Mech., **68** (1968), pp. 369–388.

[38] C. E. Pearson, *Numerical Solution for the Time-Dependent Viscous Flow Between Two Rotating Coaxial Disks*, J. Fluid Mech., **21** (1965), pp. 623–633.

[39] W. C. Rheinboldt, *Computation of Critical Boundaries on Equilibrium Manifolds*, SIAM J. Numer. Anal., **19** (1982) pp. 653–669.

[40] S. M. Roberts and J. S. Shipman, *Computation of the Flow Between a Rotating and a Stationary Disk*, J. Fluid Mech., **73** (1976), pp. 53–63.

[41] K. Stewartson, *On the Flow Between Two Rotating Coaxial Disks*, Proc. Camb. Phil. Soc., **49** (1953), pp. 333–341.

[42] J. Stöer and R. Bulirsch, *Einführung in die Numerische Mathematik. II*, Heidelberg Taschenbücher No. 114, Springer-Verlag, Berlin, 1973.

[43] R. K.-H. Szeto, *The Flow Between Rotating Coaxial Disks*, Thesis, California Institute of Technology, Pasadena, California, 1978.

[44] K. K. Tam, *A Note on the Asymptotic Solution of the Flow Between Two Oppositely Rotating Infinite Plane Disks*, SIAM J. Appl. Math., **17** (1969), pp. 1305–1310.

[45] L. O. Wilson and N. L. Schryer, *Flow Between a Stationary and a Rotating Disk With Suction*, J. Fluid Mech., **85** (1978), pp. 479–496.

[46] T. von Kármán, *Über Laminare und Turbulente Reibung*, Z. Angew. Math. Mech., **1** (1921), pp. 232–252.

[47] E. C. Zeeman, *Catastrophe Theory*, Addison-Wesley Publishing Co., Inc., Reading, Massachusetts, 1977.